

©2012

Joseph Thomas Jurisa

ALL RIGHTS RESERVED

**IMPACT OF CROSS-SHELF WINDS AND ESTUARINE/COASTAL OCEAN  
COUPLING ON BUOYANT PLUME SYSTEMS**

by

JOSEPH THOMAS JURISA

A Dissertation submitted to the  
Graduate School-New Brunswick  
Rutgers, The State University of New Jersey  
in partial fulfillment of the requirements

for the degree of

Doctor of Philosophy

Graduate Program in Oceanography

written under the direction of

Robert J. Chant

and approved by

---

---

---

---

New Brunswick, New Jersey

October, 2012

ABSTRACT OF THE DISSERTATION

**IMPACT OF CROSS-SHELF WINDS AND ESTUARINE/COASTAL OCEAN  
COUPLING ON BUOYANT PLUME SYSTEMS**

By JOSEPH T. JURISA

Dissertation Director:  
Robert J. Chant

Observational data and realistic and idealized model simulations are used to examine the impact of variable winds, topography, and shelf circulation on a buoyant river plume/estuarine system. Observational data collected during the spring of 2006 Lagrangian Transport and Transformation Experiment (LaTTE) on the New Jersey coast suggest a strong interaction between the variable wind and buoyant forcing and the shelf circulation. During a 2-week field campaign the coastal current detached from the coast and formed a recirculating eddy 60 km downstream of the outflow. This eddy was persistent for 2 weeks under variable wind forcing, as was observed from mooring, shipboard, and satellite data and also from model hindcasts. The formation of the feature is dependent on the estuarine discharge, with cross-shore winds also playing a vital role.

To provide a more generalized view of the role of cross-shelf winds, idealized simulations are run with a straight coastline, linearly sloping bathymetry, and a straight

channel as an estuary. It is found that during an offshore wind stress that the plume is initially transported offshore, but after a couple inertial periods it reaches a steady state in terms of its cross-shore salinity and velocity structure and offshore position. This steady state structure is highly dependent on the estuarine outflow conditions, with the offshore position described by a ratio of the estuarine outflow Froude number and a plume Froude number. Formulations for the plume properties are also developed. The steady state nature of the plume's response to the cross-shore winds is examined by analyzing the mixing in the plume using a salinity coordinate system.

These results and theories developed using the idealized model simulations are compared to realistic model hindcast simulations of the Hudson River plume during the 2005/2006 winter season, when offshore winds are dominant. The response of the Hudson River plume generally compares with the idealized model results, with a few exceptions due to the complex geometry of the New York Bight. This response is a departure from the assumed downwelling response, and has implications for salinity induced stratification over inner shelf during the winter season.

## Acknowledgements

President Obama's phrase "You didn't build it" certainly applies to the work done in this dissertation and my graduate career in that I have received the help and generosity of countless people, without which none of this would have been possible. I would like to thank Bob Chant for giving me the incredible opportunity to come study at Rutgers University. Bob shared with me his expansive knowledge of estuarine and coastal physics and introduced me to new experiences, professional colleagues, and friends. Simply put, I would not have been where I am today without the help of Bob. I would also like to thank my other committee members John Wilkin, Scott Glenn, and Rocky Geyer for their help, guidance, and thoughtful comments throughout this process.

During my time at Rutgers, I have had the opportunity to meet many intelligent and caring people, including my fellow graduate students and the Institute of Marine and Coastal Sciences faculty and staff. I am happy to be able to call them all colleagues and more importantly, friends. I would like to specifically thank Rachel Sipler, Carrie Ferarro, and Katye Alteri for their tremendous help and friendship, specifically during my first years here at Rutgers. Carrie, you'll always be my 'best friend.' I would like to thank Maria Aristizabal for all the support she has given me throughout the years dealing with data, ROMS, or just listening to me vent. As fellow grad students and lab group mates, Dove Guo and Jack McSweeney much needed support as well. What can be said about Eli Hunter? He's a modern day Renaissance Man, and helped out with data collection, MATLAB, ROMS, and computer issues. The Chant lab group would fall

apart without his expertise. The RU COOL group also helped out, specifically during the LaTTE experiment, which this dissertation is based on.

Outside of work, I would like to thank all my friends back home for their life-long friendship and support, and giving me somebody to hang out with back in Indiana. Also I'd like to thank my Ultimate teammates from USC. Those trips down to the Mardi Gras tournament provided much needed vacations. The ultimate team hear at Rutgers also gave me an outlet to release my energy and meet new friends.

Finally, I would like to thank my family. Their love, support, and guidance throughout my career have allowed me to accomplish my dreams. This wouldn't be complete without thanking Laura who has stood by my side and supported me this entire time. I could not ask for a better friend.

## Table of Contents

Abstract .....	ii
Acknowledgements .....	iv
List of tables .....	x
List of figures .....	xi
Chapter 1: Introduction .....	1
1.1. General Plume Structure and Transport .....	2
1.2. Response to Wind Forcing .....	3
1.2.1. Non-dimesional scaling .....	4
1.2.2. Response to alongshore winds .....	7
1.2.3. Response to corss-shore winds .....	9
1.3. Dependence of Estuarine Outflow and Bulge Circulation .....	10
1.4. Impact of Ambient Shelf Circulation .....	14
1.5. Objectives and Outline .....	15
Chapter 2: The coupled Hudson River estuarine-plume response to variable wind and river forcings .....	18
2.1. Introduction .....	20
2.2. Field Site and Data Description .....	23
2.2.1. Field site .....	23
2.2.2. New Jersey shelf moorings .....	23
2.2.3. Hudson River data .....	25
2.3. River/Estuary Forcing .....	27

2.3.1. Sea level effect on river discharge . . . . .	28
2.3.2. Subtidal volume flux . . . . .	30
2.4. Typical Downwelling Events . . . . .	32
2.4.1. Salinity and surface current response . . . . .	32
2.4.2. Propagation speeds . . . . .	33
2.4.3. Freshwater transport . . . . .	36
2.5. Downstream Detachment and Recirculation . . . . .	39
2.5.1. Hudson Shelf Valley response . . . . .	44
2.6. Discussion . . . . .	45
2.6.1. Downstream bulge formation . . . . .	45
2.6.2. Wind strength and duration . . . . .	48
2.6.3. Implications for freshwater transport on the NJ shelf . . . . .	51
2.7. Summary . . . . .	52
Chapter 3: Impact of Offshore Winds on a Buoyant Plume System . . . . .	54
3.1. Introduction . . . . .	56
3.2. Plume Properties . . . . .	58
3.2.1. Plume depth . . . . .	58
3.2.2. Plume averaged velocity . . . . .	60
3.2.3. Plume density . . . . .	61
3.3. Model Description . . . . .	62
3.4. Results . . . . .	64
3.4.1. General plume response . . . . .	64
3.4.2. Velocity structure . . . . .	69



3.4.3. Wind strength influence . . . . .	71
3.4.4. Plume averaged parameters . . . . .	73
3.4.5. Plume width . . . . .	75
3.4.6. Offshore position . . . . .	76
3.5. Plume Mixing . . . . .	78
3.5.1. Cartesian coordinate analysis . . . . .	78
3.5.2. Salinity coordinate analysis . . . . .	84
3.6 Summary . . . . .	89
Chapter 4: The response of the Hudson River plume to offshore winds . . . . .	92
4.1. Introduction . . . . .	94
4.2. Model Description . . . . .	97
4.2.1. Semi-idealized model set-up . . . . .	98
4.2.2. Realistic model set-up . . . . .	99
4.3. Idealized Wind Simulations . . . . .	100
4.3.1. General plume response . . . . .	100
4.3.2. Cross-shore transects . . . . .	103
4.3.3. Plume averaged parameters . . . . .	105
4.3.4. Plume mixing . . . . .	106
4.3.5. Offshore position and bulge formation . . . . .	108
4.4. Winter 2005-2006 Simulations . . . . .	112
4.4.1. River discharge and wind forcing . . . . .	112
4.4.2. General plume response . . . . .	113
4.4.3. Plume mixing . . . . .	117

4.4.4. Plume depth .....	119
4.5. Summary .....	120
Chapter 5: Summary .....	125
Acknowledgement of Previous Publications .....	130
References .....	131

## Lists of Tables

Table 2.1	Onset time and properties of downwelling events . . . . .	35
Table 3.1	Summary of idealized model runs . . . . .	72
Table 4.1	Summary of offshore wind events . . . . .	113

## List of Figures

Figure 2.1	Map of the Hudson River and New York Bight moorings . . . . .	24
Figure 2.2	Surface salinity, wind velocity, and river discharge . . . . .	26
Figure 2.3	Depth averaged velocity and sea level for Hudson moorings . . . . .	27
Figure 2.4	EOF time series with river discharge and sea level . . . . .	29
Figure 2.5	Subtidal volume flux from the estuary mouth . . . . .	30
Figure 2.6	Surface salinity and velocity during the first downwelling event . . .	33
Figure 2.7	Depth-averaged velocity, HSV pressure gradient, and sea level . . .	34
Figure 2.8	Freshwater flux at C moorings . . . . .	39
Figure 2.9	Satellite chlorophyll maps for days 117 and 143 . . . . .	41
Figure 2.10	Map of shipboard surface salinity and velocity with drifter tracks .	43
Figure 2.11	Schematic showing the formation of the downstream eddy . . . . .	47
Figure 2.12	Plot of Wedderburn number . . . . .	50
Figure 3.1	Model domain for idealized simulations . . . . .	63
Figure 3.2	Wind stress forcing . . . . .	64
Figure 3.3	Evolution of surface salinity and velocity for Run 8 . . . . .	65
Figure 3.4	Evolution of surface salinity and velocity for Run 19 . . . . .	66
Figure 3.5	Transect of salinity and velocity, along with depth averaged velocity and momentum for Run 8 on days 4 and 7 . . . . .	67
Figure 3.6	Transect of salinity and velocity, along with depth averaged velocity and momentum for Run 20 on days 4 and 7 . . . . .	68
Figure 3.7	Transect of salinity and velocity; profiles of velocity and	

	momentum terms . . . . .	70
Figure 3.8	Comparison of model output and theory for plume depth, velocity, density, and width . . . . .	74
Figure 3.9	Ratio of estuary and plume Froude numbers and normalized offshore position . . . . .	77
Figure 3.10	Vertical salt flux for Run 8 at two transects for days 2.5, 4.6, and 6.7 . . . . .	79
Figure 3.11	Salt terms for Run 8 at day 7.76 . . . . .	82
Figure 3.12	Surface salinity and plume averaged salinity, depth, and salt flux terms . . . . .	83
Figure 3.13	Vertical salt flux at the base of the plume for Run 8 classified by salinity . . . . .	85
Figure 3.14	Freshwater volume and $dV_f/dt$ for Run 8 classified by salinity . . . .	88
Figure 4.1	Wind rose of the wind forcing during the 2005/2006 winter . . . . .	96
Figure 4.2	LaTTE model domain . . . . .	98
Figure 4.3	Tidally averaged surface salinity and velocity for the $0^\circ$ model run for days 3.6, 5.7, and 9.8 . . . . .	100
Figure 4.4	Tidally averaged surface salinity and velocity for all model runs at day 10 . . . . .	101
Figure 4.5	Cross-shore transect of velocity and salinity for the $0^\circ$ run for days 3.6, 5.7 and 9.8 . . . . .	102
Figure 4.6	Cross-shore transect of velocity and salinity for the $0^\circ$ , $-10^\circ$ , $-20^\circ$ runs of day 9.8 . . . . .	104

Figure 4.7	Model and theoretical velocity for all model runs . . . . .	105
Figure 4.8	Vertical salt flux and plume depth averaged vertical salt flux for the 0° run on day 3.6, 5.7, and 9.8 . . . . .	107
Figure 4.9	Salt terms for the 0° run on day 9.8 . . . . .	108
Figure 4.10	Comparison of the outflow Froude number and offshore position . .	109
Figure 4.11	Contours of plume position for all runs on day 9.8 along with the location of the transition zone . . . . .	111
Figure 4.12	River discharge, wind, plume depth, and cross-shore barotropic pressure gradient for realistic run . . . . .	114
Figure 4.13	Surface map and cross-shore transect of salinity and velocity for all events . . . . .	116
Figure 4.14	Evolution of the vertical salt flux for Event 1 . . . . .	118
Figure 4.15	Salt terms for Event 1 . . . . .	119

# **Chapter 1:**

## **Introduction**

## 1.1. General Plume Structure and Transport

Classical buoyant plume theory suggests that in the absence of wind forcing or ambient shelf circulation, buoyant water upon being discharged into the coastal ocean turns to the right (in the northern hemisphere) and forms a coastal current that continues to propagate downstream in the direction of Kelvin wave propagation. The buoyant plume/ coastal current can be separated into two general categories: bottom advected and surface advected (Yankovsky and Chapman, 1997). For the surface advected case the plume is confined to a relatively thin layer at the surface and is not in contact with the bottom. The width of the resulting buoyant coastal current has been found to simply scale with the internal radius of deformation (Garvine 1995, Fong and Geyer 2002), and the propagation speed of the nose of the plume is the internal wave speed,  $c_w = \sqrt{g'h_p}$  (Lentz and Helfrich 2002, Fong and Geyer 2002) where  $g'$  is the reduced gravity of the plume and  $h_p$  is the plume depth.

In the case of a bottom advected plume, the buoyant plume is in contact with the bottom. This leads to the development of an offshore transport of buoyant water at the base of the plume due to Ekman veering. This offshore Ekman transport is predicted to continue until the plume reaches the cross-shore extent where the geostrophic velocities within the plume are equal to zero at the bottom of the water column (Chapman and Lentz 1994, Yankovsky and Chapman, 1997, Lentz and Helfrich 2002). The plume then becomes trapped at this isobath because the bottom friction due to the sheared plume geostrophic velocities is zero, ceasing the offshore Ekman transport. The width of a



bottom advected plume has been found to be wider than that of the internal rossby radius,  $W_w = c_w / f$  (Garvine 1999, Lentz and Helfrich 2002), where  $f$  is the coriolis parameter.

The depth at which the plume contacts the bottom is found to be  $h_p = \sqrt{2Qf/g'}$ , where  $Q$  is the freshwater transport in the plume (Yankovsky and Chapman 1997). Assuming a constant bottom slope  $\alpha$ , the width of the bottom advected plume is  $W_\alpha = h_p / \alpha$ . The bottom slope also leads to the propagation speed of the plume's nose to be slower than that of the internal wave speed. Lentz and Helfrich (2002) found the expression  $c_\alpha = \alpha g' / f$  to be the propagation speed for a purely bottom advected plume.

In nature, buoyant plumes are rarely purely surface or bottom advected but in fact a combination of the two cases where the inshore portion of plume  $h_p$  is greater than the water column depth ( $h$ ) while the offshore portion of the plume  $h_p$  is less than  $h$ . Lentz and Helfrich (2002) examined these intermediate cases and came up with expressions for both the width and propagation speed of the intermediate plumes. They determined the width of the intermediate case plume is the sum of the bottom and surface advected portions of the plume and formulated the expression  $W_p = (c_w / f)(c_w / c_\alpha)$ . Using the assumption of volume conservation at the nose of the plume they calculated the propagation speed of the nose of the plume to be  $c_p = c_w (1 + c_w / c_\alpha)^{-1}$ .

## 1.2. Response to Wind Forcing

Due to the natural tendency of surface advected and intermediate buoyant plumes to be in part confined to a relatively thin surface layer, buoyant plumes are strongly susceptible to

wind forcing. The strong stratification confines the wind energy input into the relatively thin buoyant player, leading the plume to be easily influenced by winds.

### 1.2.1. Non-dimensional scaling

Even though buoyant plumes are easily susceptible to wind forcing, buoyancy forcing can still play a role in the dynamics of a plume. It is therefore necessary to derive a scaling for the wind, buoyancy, and other forcings in the momentum equations. Garvine (1995) has done just that, starting with the depth averaged x (cross-shore) and y (along-shore) momentum equations of the form

$$u \frac{\partial u}{\partial x} + v \frac{\partial u}{\partial y} - fv = - \frac{1}{\rho} \frac{\partial P}{\partial x} + \frac{\tau_{wx}}{\rho h} - \frac{\tau_{bx}}{\rho h} \quad (1.1a)$$

$$u \frac{\partial v}{\partial x} + v \frac{\partial v}{\partial y} + fu = - \frac{1}{\rho} \frac{\partial P}{\partial y} + \frac{\tau_{wy}}{\rho h} - \frac{\tau_{by}}{\rho h} \quad (1.1b)$$

Where  $u$  and  $v$  are cross-shore and along-shore velocities respectively,  $\tau_w$  is the wind stress, and  $\tau_b$  is the bottom or interfacial stress. Garvine (1995) then scales Eqns. 1.1a,b

$$u \frac{\partial u}{\partial x} + v \frac{\partial u}{\partial y} - fv = - \frac{1}{\rho} \frac{\partial P}{\partial x} + \frac{\tau_{wx}}{\rho h} - \frac{\tau_{bx}}{\rho h} \quad (1.2a)$$

$$\frac{\gamma U^2}{L} \quad fU \quad \frac{c^2}{\gamma L} \quad \frac{\tau_{wx}}{\rho H} \quad \frac{r\gamma U}{H}$$

$$u \frac{\partial v}{\partial x} + v \frac{\partial v}{\partial y} + fu = - \frac{1}{\rho} \frac{\partial P}{\partial y} + \frac{\tau_{wy}}{\rho h} - \frac{\tau_{by}}{\rho h} \quad (1.2b)$$

$$\frac{U^2}{L} \quad f\gamma U \quad \frac{c^2}{L} \quad \frac{\tau_{wx}}{\rho H} \quad \frac{rU}{H}$$

Where  $\gamma$  is the ratio of the plume width to plume length (the plume slenderness),  $L$  is the alongshore length scale,  $\gamma L$  is the across-shore length scale,  $U$  is the alongshore velocity

scale,  $\gamma U$  is the across-shore velocity scale, and  $H$  is the buoyant layer depth. Garvine (1995) normalizes the velocity by  $c$  to form a Froude number  $F = U/c$ , and normalizes the plume width ( $\gamma L$ ) by the internal Rossby radius, forming a Kelvin number  $K = \gamma L / (c/f)$ . The wind stress is represented by the Ekman transport  $V_E = \tau_w / (\rho f)$  normalized by  $HU$ . The bottom/interfacial stress term is scaled to yield  $r/fH$ . Using the above parameters, the dimensional scalings in (1.2a,b) are now put in a non-dimensional form, with the terms being normalized by the pressure gradient term.

$$u \frac{\partial u}{\partial x} + v \frac{\partial u}{\partial y} - fv = - \frac{1}{\rho} \frac{\partial P}{\partial x} + \frac{\tau_{wx}}{\rho h} - \frac{\tau_{bx}}{\rho h} \quad (1.3a)$$

$$\gamma^2 F^2 \quad KF \quad 1 \quad KF \left( \frac{V_E}{HU} \right) \quad \gamma KF \left( \frac{r}{fH} \right)$$

$$u \frac{\partial v}{\partial x} + v \frac{\partial v}{\partial y} + fu = - \frac{1}{\rho} \frac{\partial P}{\partial y} + \frac{\tau_{wy}}{\rho h} - \frac{\tau_{by}}{\rho h} \quad (1.3b)$$

$$F^2 \quad KF \quad 1 \quad \frac{KF}{\gamma} \left( \frac{V_E}{HU} \right) \quad \frac{KF}{\gamma} \left( \frac{r}{fH} \right)$$

The non-dimensional scalings in (1.3) now allow for an easier comparison of the strength of the terms in relation to the pressure gradient. Garvine (1995) pointed out that since  $\gamma$  is less than unity for most plumes, the along-shore wind stress term in (1.3b) is larger compared to the across-shore wind stress in (1.3a) in relation to the respective pressure gradient terms. This gives the wind forcing limit

$$V_E / (HU) \leq O(\gamma / KF) \quad (1.4)$$

If the right hand side of (1.4) dominates, the flow in the buoyant plume is buoyancy driven, while if the left hand side dominates, the flow in the plume is now wind driven.

Whitney and Garvine (2005) modified this scaling to come up with a wind strength index based on the ratio of along-shore buoyancy and wind driven velocities in the plume. The buoyancy driven term is written as

$$u_{dis} = \frac{c}{K} \quad (1.5)$$

For a surface advected plume the width of the plume can be estimated as the internal Rossby radius yielding a Kelvin number of 1 and setting the buoyancy driven velocity simply as the internal wave speed. The wind driven term is written as

$$u_{wind} = \sqrt{\frac{\rho_{air}}{\rho} \frac{C_{10}}{C_{Da}} U} \quad (1.6)$$

Where  $C_{10}$  is the surface drag coefficient,  $C_{Da}$  is the drag coefficient for the depth-averaged velocity, and  $U$  is the wind velocity. The ratio of these two terms (1.5) and (1.6) is the wind strength index

$$W_s = \frac{u_{wind}}{u_{dis}} \quad (1.7)$$

When  $W_s$  is greater than one, wind forcing dominates the flow, while if  $W_s$  is less than one, the flow is buoyancy driven. The wind strength index in (1.7) from Whitney and Garvine (2005) is similar to the term formulated by Lentz and Largier (2006) (their equation 5) with a difference being the buoyancy driven term is calculated in a manner similar to the plume propagation speed in Lentz and Helfrich (2002) described here previously.

### 1.2.2. Response to alongshore winds

Studies examining the effect of winds on buoyant plumes have mainly focused on alongshore winds as the dominant factor in transporting freshwater across the continental shelf. Downwelling winds (in the direction of Kelvin wave propagation) have been found to compress and deepen the plume against the coast. This leads to a steepening of the isopycnals, strengthening the downstream flows in the plume (Moffat and Lentz 2012). Upwelling winds (opposing Kelvin wave propagation) have the effect of transporting the buoyant plume offshore due to Ekman dynamics. Fong and Geyer (2001), through an idealized numerical model, examined the response of a buoyant plume far from the buoyant source to upwelling winds. Fong and Geyer (2001) found that once an upwelling wind stress is applied, the offshore edge of the plume mixes to a critical thickness ( $h_c$ ) and begins to widen. The plume detaches from the coast and continues to widen until the entire plume has mixed to reach the critical thickness. Once the plume reaches its critical thickness it will continue to be transported offshore by the winds until it eventually mixes with the ambient shelf water.

Fong and Geyer (2001) and others (Lentz, 2004; Hetland, 2005) calculate the thickness the plume mixes to using a critical bulk Richardson number ( $Ri_c$ ), which represents the balance between the wind driven shear that enhances mixing and the plume's buoyancy that works to inhibit mixing,

$$Ri_c = \frac{g\Delta\rho_o h_c}{4\rho_a |\Delta u|^2} \quad (1.8)$$

Where  $\rho_a$  is the ambient density,  $\Delta\rho_o$  is the density anomaly in the plume immediately after the onset of wind forcing,  $h_c$  is the plume thickness on the offshore side of the

plume, and  $\Delta u$  is the velocity difference across the plume. In this case,  $\Delta u$  can be thought of as the cross-shore Ekman transport  $U_e = \tau_w / \rho_a f$  divided by  $h_c$  and substituted into (1.8) (Fong and Geyer, 2001). The factor of 4 comes from the assumption that the mean velocity in the plume is the Ekman velocity and the shear is constant over the thickness of the plume (Fong and Geyer, 2001). Typical values for  $Ri_c$  have been found to be in the range of 0.5-1.0. Solving for  $h_c$  yields

$$h_c = \left( \frac{4 Ri_c \rho_a U_e}{g \Delta \rho_a} \right)^{1/3} \quad (1.9)$$

Once the offshore edge of the plume mixes to this critical thickness, the offshore edge travels offshore at the Ekman velocity (Fong and Geyer, 2001). Hetland (2005) manipulated (1.8) slightly differently, solving instead for a critical salinity. Portions of the plume less than the critical salinity will continue to mix, while portions greater than the critical salinity are protected from further wind mixing.

Momentum balances computed in Fong and Geyer (2001) reveal that the alongshore balance is an Ekman balance between the vertical stress divergence and the coriolis acceleration. The cross-shore momentum balance yields a balance of the coriolis acceleration, pressure gradient, vertical stress divergence, and temporal acceleration.

Moffat and Lentz (2012) have examined the response of a buoyant plume to a downwelling wind stress using an idealized 2-D numerical model. At the onset of the wind stress a surface mixed layer is initially formed that can be estimated using (1.9). Through the onshore advection of the isopycnals by the Ekman transport and the continual mixing and deepening of the mixed layer by the wind stress, the isopycnals become vertical and the plume becomes attached to the bottom. The response of the

plume to the downwelling wind stress is dependent on the initial width ratio of the plume,  $W_\gamma/W_\alpha$ , where  $W_\gamma$  is the width of the plume that is detached from the bottom and  $W_\alpha$  is the width of the plume that is still in contact with the bottom. Plumes that are mostly bottom attached will mix less than plumes that are more surface advected. The increased transport in the plume is characterized by the sum of the geostrophic barotropic and baroclinic transports,  $Q_p = Q_{baroclinic} + Q_{barotropic}$ , where

$$Q_{barotropic} = \frac{\tau}{r\rho_o} A_p \quad (1.10)$$

and

$$Q_{baroclinic} = \frac{g'h_p^2}{6f} \quad (1.11)$$

Here,  $\tau$  is the downwelling wind stress,  $r$  is a linear drag coefficient,  $A_p$  is the cross-sectional area of the plume,  $g'$  is the reduced gravity, and  $f$  is the coriolis acceleration.

### 1.2.3. Response to cross-shore winds

While much work has been done to understand the response of a buoyant plume to alongshore winds, relatively little has been done to examine the effect of cross-shore winds. One of the early plume modeling studies (Chao, 1988) examined the effects of wind on buoyant plume and estuarine circulations. For an offshore wind it was found that the alongshore currents on the offshore side of the plume were stronger than alongshore currents near the coast, leading the buoyant plume to appear separated from the coast. For onshore winds it was noted that downstream transport was reduced while upstream transport was significantly increased. A more recent modeling study by Choi and Wilkin (2007) briefly looked at the effects of cross-shelf winds on the Hudson River

plume in New York Bight. Similar to Chao's (1988) results, Choi and Wilkin's (2007) results show that for the offshore wind there is a downstream offshore jet and weak inshore currents.

### 1.3. Dependence on Estuarine Outflow and Bulge Circulation

Choi and Wilkin (2007) also note that the freshwater storage in New York Harbor and Raritan Bay increases with onshore winds and decreases with offshore winds. This change in flushing rates may impact estuarine outflow parameters (described below). In the Hudson River Ralston et al. (2008) noted that the wind driven sea-level set-up was an important driver for the circulation and salt storage in the river. Geyer (1997) revealed that along channel winds had a profound effect on the flushing of freshwater from a small shallow bay. The formation of the Chesapeake Bay coastal current was found to be correlated to the wind driven subtidal discharge out of the bay, not river discharge (Rennie *et al.* 1999).

The estuarine outflow conditions can have an important impact in driving the circulation in the plume and in determining a classification for buoyant plume systems. Garvine (1995) developed a plume classification system based on a Kelvin number ( $K$ ), where plumes with  $K \ll 1$  are classified as small scale discharges and plumes with  $K \gg 1$  are classified as large scale discharges. Here  $K$  is thought of as a non-dimensional width of outflow, hence when  $K \ll 1$  the width of the outflow is less than the internal Rossby radius and vice versa when  $K \gg 1$ . This gives important insights on the role of the estuarine outflow on buoyant plume structure. Garvine (1995) states that for the  $K \ll 1$  case the flow in the plume is highly nonlinear, while in the  $K \gg 1$  case the flows are dominated by an across-shore geostrophic momentum balance.



In an early plume modeling study, Chao and Boicort (1986) noted that for higher velocity outflows there was an anti-cyclonic eddy, or bulge, that formed at the mouth of the estuary and water from this recirculating bulge fed the buoyant coastal current. For runs with a slower outflow velocity this recirculating bulge region was less pronounced or absent altogether. The transition between the recirculating bulge region and the coastal current was very abrupt for the high velocity outflow runs while for the slower outflow runs the transition was much more gradual (Chao and Boicort, 1986).

Yankovsky and Chapman (1997) later described the recirculating bulge region as a steady feature several internal Rossby radii wide. Fong and Geyer (2002) noted that the bulge is not steady and is continually growing in time. Studies have shown that approximately 30-50% of the buoyant discharge is transported into the coastal current with the rest feeding the continually growing bulge region (Fong and Geyer, 2002; Avicola and Huq, 2003; Horner-Devine et al. 2006). There is also a noted dependence of the outflow conditions on the bulge structure and therefore freshwater transport in the coastal current.

Yankovsky and Chapman (1997) related bulge structure to an outflow Burger number,  $S = (g'h)^{1/2} / fL$  and an external Rossby number,  $Ro = u_i / fL$ . Where h, L, and  $u_i$  are the depth, width, and velocity of the buoyant outflow respectively. The Burger number (S) is simply just the inverse of the Kelvin number (K) used by Garvine (1995) to classify buoyant outflows, and the Rossby number is a measure of the non-linearities within the flow. So using Yankovsky and Chapman's (1997) classification, large S and Ro lead to large bulge regions with non-linear flow, and low S and Ro lead to minimal recirculating bulge regions with mainly geostrophic flow. Fong and Geyer (2002) also

found a strong outflow Rossby number dependence on bulge structure with higher Rossby numbers yielding larger bulge regions. Horner-Devine *et al.* (2006) determined that bulge growth is proportional to  $Ro^{0.25}-Ro^{0.32}$ . They also noted an important dependence of the outflow Froude number,  $Fr = u_i / \sqrt{g'h}$ , on the bulge structure and stability and freshwater transport in the coastal current. When the outflow Froude number is critical or super-critical the bulge region is detached from the coast and transport in the coastal current is greatly reduced. The bulge will then grow and eventually reattach, increasing coastal current freshwater transport, and then repeating the cycle. This reinforces the conceptual model of an eddy colliding with a wall by Nof (1988) and applied to the bulge/coastal current circulation by Fong and Geyer (2002). Fong and Geyer (2002) described the bulge region as a baroclinic eddy with a portion of the eddy cut off by the wall. The portion that is cut off by the wall ‘leaks out’ of the eddy and is transported downstream in the coastal current.

In the same vein, Fong and Geyer (2002) also related freshwater transport in the coastal current to the potential energy in the plume,  $g'h$ , and the total energy through a Bernoulli function,

$$B = g'h + \frac{\bar{u}^2 + \bar{v}^2}{2} \quad (1.11)$$

It was noted that the freshwater transport in the coastal current was higher when the potential energy and Bernoulli function was higher near the coast. Due to the general structure of the bulge the highest values of the potential energy and Bernoulli function are typically found near the center of the bulge. As previously noted, Horner-Devine *et al.* (2006) found that the offshore distance of the center of the bulge was related to the

outflow Rossby and Froude numbers. The higher the outflow Rossby and Froude numbers (hence, higher outflow velocity) the further offshore the center of the bulge, which means lower potential energy and Bernoulli function near the coast, leading to lower freshwater transport in the coastal current. They also reported that the radius of the plume was dependent on the internal deformation radius.

The previously referenced bulge studies were all model or laboratory studies, and up until recently there was doubt about whether bulge regions exist in nature. In the early part of this past decade two research programs were conducted to examine the impact of rivers on shelf biological and geochemical processes: the Lagrangian Transport and Transformation Experiment (LaTTE) (Chant et al., 2008b) on the New Jersey shelf and the River Influences on Shelf Ecosystems (RISE) (Hickey et al. 2010) on the Oregon shelf. One of the many important observations to come out of these projects was the actual observation of a recirculating bulge region. Chant et al. (2008a) and Horner-Devine (2009) described the bulge circulation for the Hudson River and Columbia River plumes respectively. Both studies noted the bulge circulation conformed to the prevailing theory and that freshwater transport in the coastal current comprised of approximately 1/3 of the freshwater outflow.

Using an idealized numerical model simulation, Yankovsky *et al.* (2001) examined the effects of a variable discharge on buoyant plume structure. They found that when freshwater discharge was increased to simulate a storm event, the bulge became partially detached from the coast, which is not surprising when taking into account the results of Horner-Devine *et al.* (2006). Yankovsky *et al.* (2001) also discovered that after a pulsed discharge, and in the presence of a downstream ambient shelf flow, a

‘secondary’ recirculating bulge formed and slowly propagated downstream. Yankovsky *et al.* (2001) used the model results to explain a downstream buoyant eddy along the New Jersey coast in May of 1989. However, Choi and Wilkin (2007) in their simulations of the Hudson River plume found that for a pulsed buoyant discharge a downstream bulge did not form, leading to possibility that another forcing such as wind plays a role as well.

Over the entire range of model runs in Fong and Geyer (2002) the freshwater transport in the coastal current never reached that of the freshwater outflow, even for low Rossby number runs. The only conditions under which the coastal current transport approached the freshwater outflow were when a shelf-wide downstream ambient current was imposed at the model boundaries. Fong and Geyer (2002) determined that the freshwater transport in the coastal current was the sum of the barotropic and baroclinic transports.

#### 1.4. Impact of Ambient Shelf Circulation

While wind forcing has been shown to play an important role in plume structure and transport, the results of Fong and Geyer (2002) illustrate the potential impact shelf circulation can have on buoyant plume structure and freshwater transport pathways on the continental shelf. For example, the Columbia River plume has been found to flow either north or south due to the combination of wind forcing and shelf circulation (Hickey *et al.* 2005). In a modeling study of freshwater transport in New York Bight, Zhang *et al.* (2009) noted three main pathways for the Hudson River plume: the Long Island coast, the New Jersey coast, and a mid-shelf pathway running along the southern edge of the Hudson Shelf Valley (HSV). Downwelling winds transport freshwater along the New Jersey coast, upwelling winds drive the mid-shelf and the Long Island pathways which

dominate during the summer and fall transition periods respectively (Zhang et al. 2009). All the pathways are affected by the barotropic shelf circulation. In fact Castelao et al. (2008) noted that the freshwater in mid-shelf pathway is not a direct result of the cross-shore advection of the plume from the New Jersey coast. Upwelling winds initially separate the plume from the coast, however the freshwater is continually be transported across the shelf through the plume, resulting in the transport time from the outflow region to the mid-shelf to be greatly reduced. Zhang et al. (2009) also carried out numerical simulations without the HSV. For that simulation, the mid-shelf pathway was greatly reduced with the Long Island and New Jersey pathways dominating. This change in the shelf circulation of the New York Bight without the HSV illustrates its impact on the freshwater transport pathways. Zhang et al. (2009) found that the barotropic pressure gradients on the shelf were altered by the HSV, leading to the differences in the transport pathways.

Diurnal winds in the north-south direction were found to reduce the amount of freshwater transported in the coastal current due to the winds enhancing bulge formation (Hunter et al. 2010). Zhang et al. (2009) also noted that the ambient shelf circulation in the Mid-Atlantic Bight, as described by Lentz (2008), works to decrease the size of the bulge region for the Hudson River plume and transport freshwater in a southerly direction. Zhang et al. (2009) focused on long-term mean freshwater transports and along shore winds, making the effect of higher frequency and cross-shore wind forcing less clear.

## 1.5. Objectives and Outline

The literature raises some questions that I seek to address in this dissertation:

- 1.) What role does a variable wind forcing, shelf circulation, and estuarine outflow conditions play in the development of a downstream buoyant recirculating feature observed during the 2006 LaTTE field study and a similar feature described by Yankovsky et al. (2001)?
- 2.) What role do offshore winds play in both along- and cross-shelf freshwater transport and plume structure in general?
- 3.) How does the response of the Hudson River plume to offshore winds compare to idealized numerical simulations?
- 4.) How does the unique bathymetry and geometry of the New York Bight alter the plume's response?
- 5.) What is the role of the estuary in determining the plume structure and position on the shelf?

Chapter 2 addresses the observations from the 2006 LaTTE field study. The typical downwelling response of the Hudson River plume is described, as is the formation of a downstream recirculation feature off the New Jersey coast. The role of the shelf circulation, wind forcing, and estuarine discharge is addressed.

Chapter 3 outlines the response of a buoyant river plume system to offshore directed winds using an idealized model domain and forcing. Formulations for plume averaged depth, velocity, density, and width will be developed, along with a parameterization of the estuarine outflow's role in setting up the offshore position of the plume. Momentum and salinity equations are analyzed to address the role of mixing in determining the observed plume structure. In addition the traditional Cartesian analysis

of mixing, a salinity coordinate analysis is utilized to further analyze the mixing over the entire plume area.

Chapter 4 addresses complexities of the Hudson River plume and the New York Bight response to offshore directed winds. Numerical simulations are carried out with idealized wind forcing to retrieve the underlying response of the plume with the results compared to the idealized simulations in Chapter 2. The role of the shelf circulation on the plume structure is addressed. Realistic numerical simulations are run to recreate the 2005/2006 winter season, in which offshore directed winds are dominant. The results are compared to the semi-idealized results.

## **Chapter 2:**

**The coupled Hudson River estuarine-plume  
response to variable wind and river forcings**



### Abstract

Observations of the Hudson River plume were taken in the spring of 2006 in conjunction with the Lagrangian Transport and Transformation Experiment (LaTTE) using mooring arrays, shipboard observations and satellite data. During this time period the plume was subjected to a variety of wind, buoyant and shelf forcings, which yield vastly different responses in plume structure including a downstream recirculating eddy. During weak and downwelling winds the plume formed a narrow buoyant coastal current that propagated downstream near the internal wave speed. Freshwater transport during periods when the downwelling wind was closely aligned with the coast was near the river discharge values. During periods with a cross shore component to the wind, freshwater transport in the coastal current estimated by the mooring array is less than the river discharge due to a widening of the plume that leads to the internal Rossby radius scaling for the plume width to be invalid. The offshore detachment of plume and formation of a downstream eddy that is observed surprisingly persisted for 2 weeks under a variety of wind forcing conditions. Comparison between mooring, shipboard, and satellite data reveal the downstream eddy is steady in time. Shipboard transects yield a freshwater content equal to the previous three days of river discharge. The feature itself was formed due to a large discharge following a strong onshore wind. The plume was then further modified by a brief upwelling wind and currents influenced by the Hudson Shelf Valley. The duration of the detachment and downstream eddy can be explained using a Wedderburn number which is largely consistent with the wind strength index described by Whitney and Garvine (2005).

## 2.1. Introduction

The typical response of a buoyant discharge into the coastal ocean is to form a buoyant coastal current that flows in the direction of Kelvin wave propagation. In addition, previous modeling studies (Yankovsky and Chapman, 1997; Fong and Geyer, 2002) have theorized that a recirculating bulge can form at the mouth of the outflow. The natural formation of a bulge near the outflow was later confirmed by Chant et al. (2008) in a study of the Hudson River Plume, and the circulation of the Columbia River plume has also been described as well (Horner-Devine, 2009). Bulge formation occurs when only a fraction of the estuarine discharge is incorporated in a coastal current with the remaining fluid feeding a non-steady and growing recirculating bulge of buoyant water that recirculates near the outflow region (Avicola and Huq, 2003; Fong and Geyer, 2002; Horner-Devine et al., 2006). Fong and Geyer (2002) found that transport in the coastal current never reaches the outflow value for an unforced plume and that the fraction of the transport is dependent on an outflow Rossby number. In the Fong and Geyer (2002) simulations freshwater transport in the coastal current only approached the river outflow values when a downstream ambient current was imposed over the domain. In a laboratory study, Horner-Devine et al. (2006) found that transport in coastal current had an outflow Froude number dependence, while Huq (2009) relates bulge formation, and therefore freshwater transport, to a Kelvin number which is thought of as the non-dimensional width of the estuary mouth. In all cases bulge formation and the freshwater transport in the coastal current is strongly dependent on the outflow conditions of the buoyant source.

Winds are known to play an important role in determining plume structure and the fate of freshwater. Studies have focused mainly on the effect of along shore winds on the plume. Downwelling winds tend to push the buoyant plume against the coast through an Ekman response strengthening the coastal current, while upwelling winds have been found to thin the plume to a critical thickness and transport the buoyant layer offshore where it will eventually mix with the ambient shelf water (Fong et al. 1997, Fong and Geyer 2001, Lentz 2004, Hetland 2005, Lentz and Largier, 2006).

Wind effects have been found to strongly influence the outflow from estuaries as well. A study by Ralston et al. (2008) show the effects of a wind stress and a wind induced pressure gradient on the estuarine exchange flow and salt storage in the Hudson River. Choi and Wilkin (2007) found that freshwater storage in Raritan Bay in New Jersey, which is connected to the New York Harbor/Hudson River estuary, is dependent on the wind forcing conditions. It has also been noted that subtidal volume flux from Chesapeake Bay is correlated with wind speed and direction (Garvine 1985, Valle-Levinson 1995). Rennie et al. (1999) built on this and determined that the formation and propagation of the Chesapeake buoyant coastal current downstream was correlated to the wind driven subtidal discharge out of the bay, not on river discharge.

This study focuses on observations collected in the New York Bight in the spring of 2006 during the Lagrangian Transport and Transformation Experiment (LaTTE). The observations were collected during the spring transition between the downwelling dominant winter to the upwelling dominant summer. During this transition period the winds are more variable and passing spring storms can lead to large fluctuations in river discharge and periods of sustained onshore winds. These more complex interactions

produce a suite of discharge configurations that fundamentally impacts the fate and transport of buoyant water on the shelf. While these flows are complex and variable, modeling results by Zhang et al. (2009) reveal that there are essentially only a few freshwater transport modes which are determined by a combination of river discharge, topography, and wind forcing.

During the time period of the LaTTE 2006 field study the buoyant plume was subjected to large variations in river outflow and extended periods of upwelling, downwelling, and onshore wind forcings. The variable forcing terms in conjunction with the complex coastline and bathymetric features of the New York Bight yield surprisingly different responses in buoyant plume structure and freshwater transports. This study focuses on the different plume structures during downwelling wind events which include the typical response of coastal current formation and propagation downstream, and the detachment of the coastal current and formation of a downstream recirculation feature which has a similar structure to a feature has described by Yankovsky et al. (2001). This downstream recirculation feature, which persists for approximately two weeks, appears to have been formed by the interaction between the estuarine response to onshore winds, a brief upwelling wind, and the shelf circulation influenced by the Hudson Shelf Valley.

In this paper we will show evidence of an estuarine/coastal ocean coupling, its impact on freshwater transport pathways and the impact of wind driven shelf circulation influenced by coastline geometry and a shelf valley on normal bulge and coastal current formation and their effect on the fate and transport of freshwater on the New Jersey shelf. This paper is organized as follows: section 2 will be a description of the mooring locations and the types of data collected for the analysis; section 3 will present the

forcing of the Hudson River; section 4 will describe the response of the plume to downwelling winds; section 5 will examine the detachment of the coastal current and formation of the downstream bulge; and in section 6 we will discuss the interpretations and implications of the results.

## 2.2. Field Site and Data Description

### 2.2.1. *Field site*

The 2006 LaTTE field effort occurred during the typical spring freshet, when the Hudson River discharge as measured at Green Island, NY has averaged between 900-1100 m<sup>3</sup>/s during November-February over the past 46 years of measurements. The geometry of the Hudson River outflow is unusual in that it is located at the apex of the New York Bight (NYB) where the New Jersey and Long Island coastlines nearly form a right angle (Fig 2.1). Further complicating matters is the presence of the Hudson Shelf Valley (HSV) that bisects the continental shelf from the slope to approximately 20 km from the Hudson River outflow in the NYB apex, and has been shown to impact the generally along isobath ambient circulation in the Mid Atlantic Bight (Harris et al., 2003; Lentz, 2008).

For this study, atmospheric and hydrographic data sets collected from the New Jersey shelf and the Hudson River are utilized to examine the effect of wind, river, and shelf forcings on the Hudson River plume.

### 2.2.2. *New Jersey shelf moorings*

Data from the New Jersey Shelf was obtained in conjunction with the Lagrangian Transport and Transformation Experiment (LaTTE) covering the time period of yearday

101-167 (April 11, 2006 to June 16, 2006). The moorings consisted of 5 inner shelf moorings (N1, C1-3, S1) and 2 Hudson Shelf Valley moorings (SV1, SV2) each containing a bottom mounted Doppler current profiler and a near surface and bottom conductivity and temperature (CT) sensor (Fig 2.1). The C-line moorings also contained a mid-depth CT sensor. Surface salinity is unavailable at SV1 due to damage from ship traffic and current data at C2 is unavailable due to equipment failure. The depths of the mooring locations range from 13 m at C1 to 70 m at SV2. Coastal sea level is recorded at Sandy Hook, NJ (NOAA Station ID: 8531680) and wind data is recorded at Ambrose Light Tower (NOAA Station ID: ALSN6).

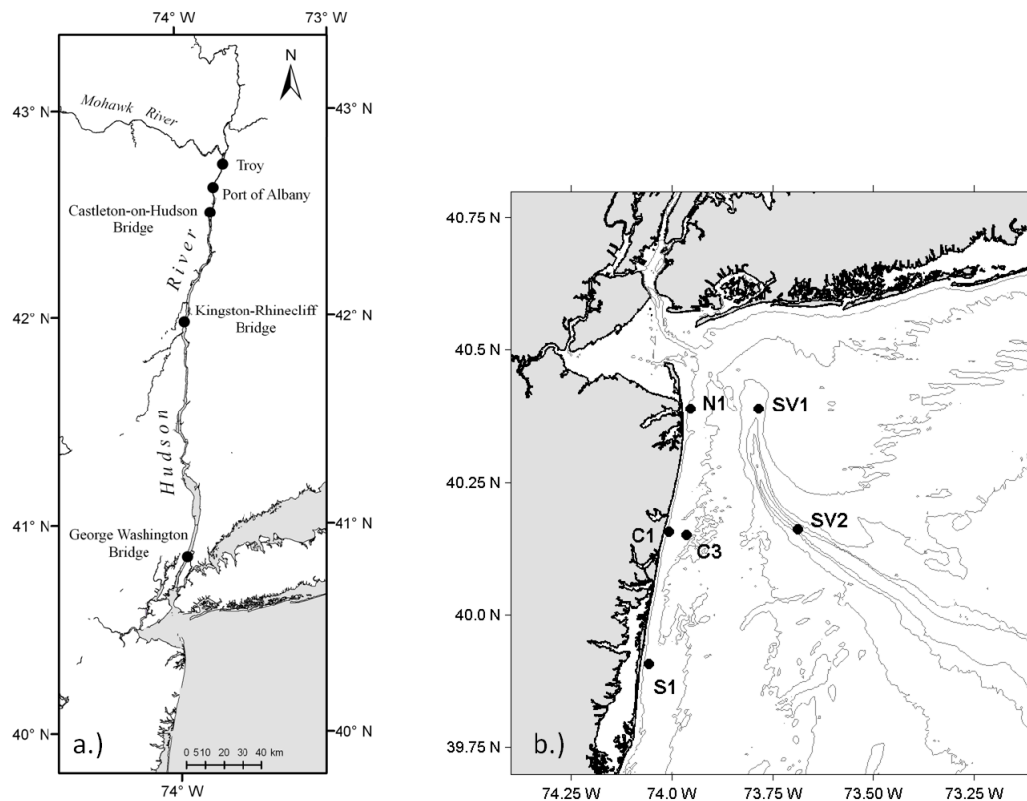


FIG. 2.1. (a) Map of the Hudson River moorings and (b) the moorings in the New York Bight

The data is low-passed with a filter with a 36 hour cut-off frequency and a 72 hour window to remove the influence of tidal effects. The velocity data from the shelf moorings undergo a principal component analysis and are rotated to the direction of the major axis. The flows are nearly rectilinear due to the constraints of the coast (N1, C1, C3, and S1) and the bathymetry of the shelf valley (SV1 and SV2). The positive alongshore flow is in the general northward direction toward the Hudson River outflow for the inner shelf moorings and up-canyon toward the New York Bight apex for the HSV moorings.

### 2.2.3. *Hudson River data*

Hudson River water level and velocity data was obtained from the National Oceanic and Atmospheric Administration's Center for Operational Oceanographic Products and Services (NOAA CO-OPS). The mooring systems were deployed by NOAA CO-OPS in the Hudson River near the George Washington Bridge, Kingston-Rhinecliff Bridge, Castleton-on-Hudson Bridge, the Port of Albany, and Troy, NY. The time period analyzed spans between yearday 96-136, coincidentally coinciding with the LaTTE 2006 field survey. The current data is rotated along its major and minor axis and averaged over the depth of the water column. The depth averaged velocities and water level data are then filtered in the same manner described above.

The river discharge for the Hudson River drainage basin is computed to be 2 times the sum of the discharges measured for the Mohawk River at Cohoes and the Hudson River at Ft. Edwards plus the discharges of the Passaic and Raritan Rivers. The Cohoes and Ft. Edwards measurements must be multiplied by 2 to account for those

stations not capturing the entire watershed. This is the same formulation for the ‘gauged’ river discharge used in Chant et al. (2008).

Water level data recorded by NOAA at Sandy Hook, NJ (station ID: 8531680) and Battery Park, NY (station ID: 8518750), and by USGS at Hastings-on-Hudson (station ID: 01376304) along the river are also used to complement the NOAA data in the subsequent analysis.

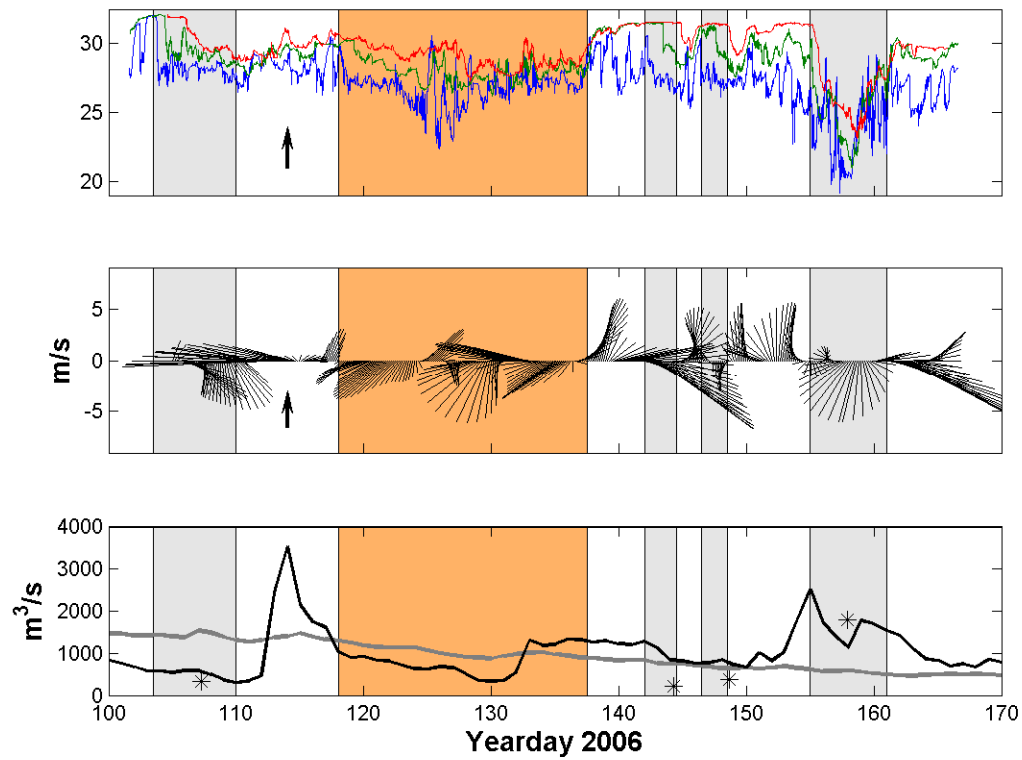


FIG. 2.2. (a) Surface salinity at N1 (blue), C1 (green), and S1 (red). (b) Wind direction and magnitude measured at Ambrose Light Tower. (c) Hudson River discharge. Stars (\*) represent estimates of the freshwater flux at the C mooring line. Gray shaded areas signify periods of downwelling wind with a typical coastal current propagating along the coast, orange shaded area signifies period of coastal current detachment, arrow at day 114 denotes time of high discharge



## 2.3. River/Estuary Forcing

Estuaries and river plumes are coupled by the exchange of fluid at the river's mouth and consequently we describe the response of both systems in the analysis. In this section we will describe the Hudson River forcing conditions during the field study that we will later use to explain the downstream bulge feature observed on the New Jersey coast.

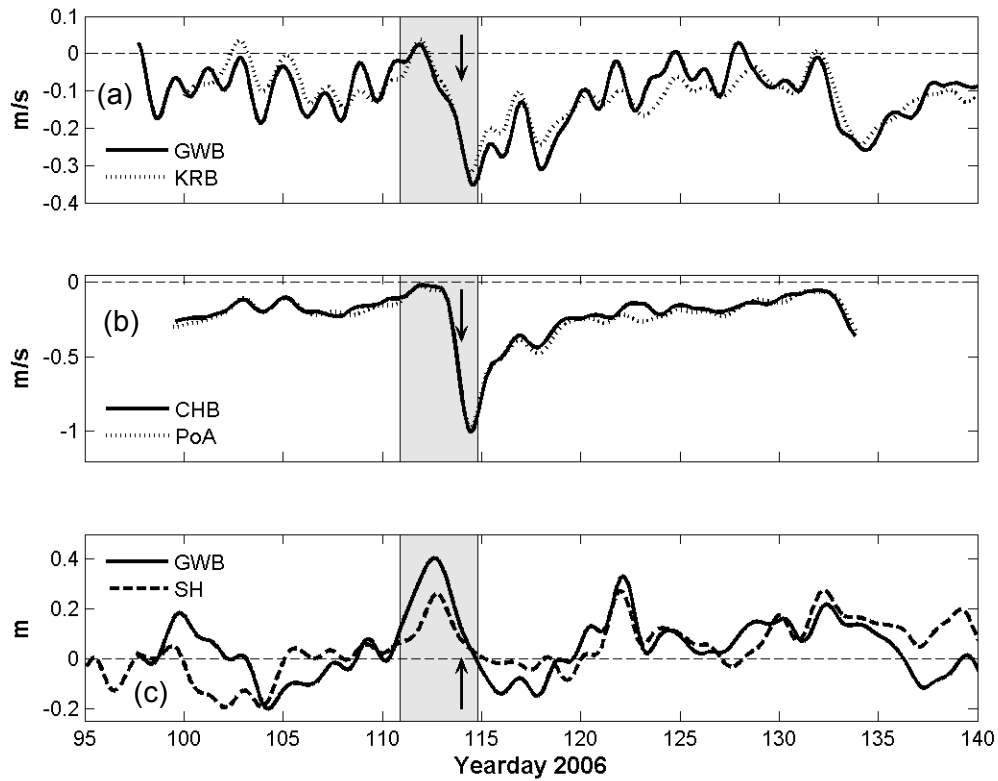


FIG. 2.3. Filtered depth averaged velocities measured at George Washington Bridge (GWB, solid), Kingston-Rhinecliff Bridge (KRB, dotted) (a) and Castleton-on-Hudson Bridge (CHB, solid), Port of Albany (PoA, dotted) (b). Filtered sea level height at GWB and Sandy Hook. Shaded area marks period of onshore winds, while the arrow marks the time of peak river discharge

### 2.3.1. *Sea level effect on river discharge*

The average river discharge for the Hudson River watershed during the field experiment is 1025 m<sup>3</sup>/s with the maximum discharge of 3500 m<sup>3</sup>/s occurring on day 114. Another high discharge event of 2500 m<sup>3</sup>/s occurred on day 155 and a ten day period of above average discharge occurred between days 133-142 (Figure 2.2c). However, as noted by Rennie et al. (1999), river discharge is not always indicative of buoyant plume formation along the coast; wind driven subtidal discharge can be an important factor as well. As such, the effect of coastal sea level on the Hudson River discharge is examined.

Sea level measured at Sandy Hook, NJ near the Hudson River outflow is best correlated with east-west winds (Harris et al. 2003). These wind and sea level forcings along the New Jersey coast have been found to affect the circulation, estuary length, and salt transport in the Hudson River (Lerczak et al. 2008, Ralston et al. 2008).

During the 2006 LaTTE field study there is a strong onshore wind event from day 111-115 that drives a high sea level set up at Sandy Hook (SH, Figure 2.3c). There is also a corresponding increase in water level in the Hudson River measured at the George Washington Bridge which is approximately 40 km from Sandy Hook (GWB, Figure 2.3a). Not only did the onshore wind increase water level in the river, it actually slowed down, and in some cases reversed the subtidal depth-averaged flow in the river. Subtidal flows in the Hudson River reverse up to the Kingston-Rhinecliff Bridge (KRB) 170 km upstream from Sandy Hook, and noticeably decrease all the way up to the Port of Albany (PoA) 210 km from Sandy Hook (Figure 2.3a,b). Maximum velocities are achieved after the relaxation of the onshore wind.

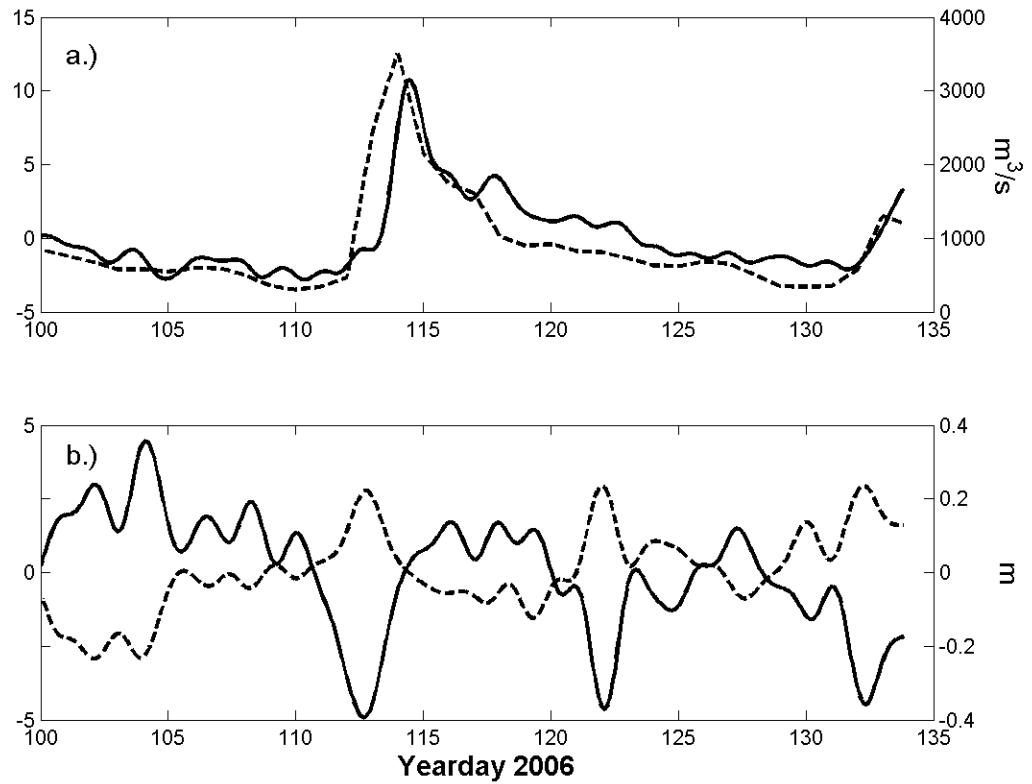


FIG. 2.4. (a) EOF mode 1 time series (left axis, solid line) and gauged Hudson River discharge (right axis, dashed line). (b) EOF mode 2 time series (left axis, solid line) and relative sea level at Sandy Hook, NJ (right axis, dashed line)

Near the end of the onshore wind event on day 114 there is a high discharge event associated with a passing storm. In an attempt to separate the effect of the coastal sea level set up and high discharge on the river water level and subtidal velocities, an empirical orthogonal function (EOF) analysis is carried out using the Hudson River data, which separates the data set into temporal and spatial modes. In this analysis the first two modes are found to be statistically significant. The first mode is found to be strongly correlated with river discharge and the second mode with sea level at Sandy Hook and the E-W wind (Figure 2.4). For water level, the variance explained by the first mode

associated with river discharge increases from less than 2 % near the mouth of the Hudson to greater than 85% at Albany. The opposite is true for the variance explained by the 2<sup>nd</sup> mode; wind driven sea level at the coast accounts for greater than 85% of the variance near the mouth of the Hudson and less than 10% at Albany. Velocity is mainly driven by discharge with the variance explained by the first mode increasing from 65% at the GWB to 90% at Albany.

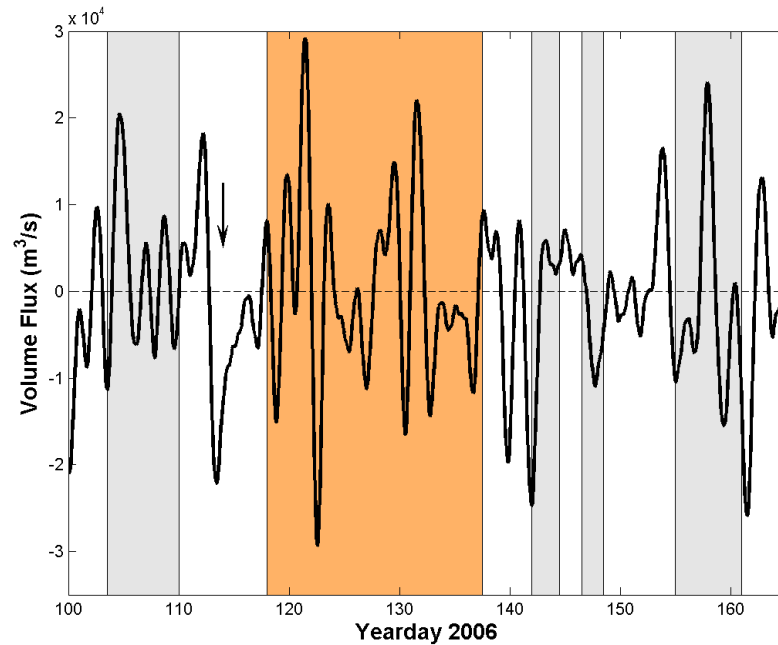


FIG. 2.5. Subtidal volume flux from estuary mouth calculated from Eqn. (1) using sea level data from Sandy Hook, NJ. Positive(negative) values are into (out of) the estuary. Gray shaded areas signify periods of downwelling wind with a typical coastal current propagating along the coast, orange shaded area signifies period of coastal current detachment, arrow at day 114 denotes time of high discharge

### 2.3.2. Subtidal volume flux

The EOF analysis implies that the onshore wind is leading to storage of water within the Hudson River estuary which is released during the relaxation that occurs during the high

discharge event. Here we quantify the subtidal discharge from the estuary to come up with a better understanding of the actual freshwater discharge than the gauged data.

Using sea level data from Sandy Hook, NJ, the subtidal volume flux is calculated as

$$Q_{out} = A_{est} \frac{d\eta_{SH}}{dt} + Q_r \quad (2.1)$$

where  $Q_{out}$  is the volume of discharge,  $A_{est}$  is the area of the estuary,  $\eta_{SH}$  is the sea level measured at Sandy Hook, NJ and  $Q_r$  is the river discharge. Sea level at Sandy Hook is used for simplicity since sea level measured at stations further up the estuary are highly correlated with Sandy Hook with minimal time lag during this time period. The results are plotted in Figure 2.5. From the results we can see that there are large subtidal net volume fluxes out of the estuary (negative values) on starting on days 113, 123, 142, and 163, with the largest integrated discharge volume occurring during the day 113-117 event. Using the combination of the high subtidal volume flux and integrated discharge volume during the day 113-117 event, coupled with the high discharge event on day 114, we can determine that a large amount of freshwater is being discharged onto the New Jersey shelf during this time period. This freshwater discharge which is due to the coupled coastal ocean/estuarine response to cross-shore wind stresses has implications on buoyant plume structure and freshwater transport described later in section 2.5.

## 2.4. Typical Downwelling Events

### *2.4.1. Salinity and surface current response*

During the 2006 field study there were 4 distinct downwelling events starting on days 103, 142, 146, and 155 (gray shaded areas in Figure 2.2). The day 155 downwelling event occurred when the river discharge was  $2500 \text{ m}^3/\text{s}$ , while the events on days 103, 142, and 146 occurred under higher discharge conditions between  $500\text{-}1200 \text{ m}^3/\text{s}$  (Fig 2c). The beginning of these events is marked by downwelling winds and a sharp decrease in surface salinity at the N1 mooring (Fig 2.2a,b). During the downwelling events, low salinity water travels southward in a buoyant coastal current, and this downstream propagation of the buoyant coastal current can be seen in the surface salinities at the inner shelf moorings where the low salinity water arrives at N1 then C1 and finally at S1. This propagation can be more clearly seen in Figure 2.6 for the downwelling event originating on day 103. The system then resets after a upwelling wind event where the buoyant water is moved offshore and nearshore salinities return to typical shelf values (last three gray shaded regions in Fig 2.2a). While most downwelling events reset within a few days, the downwelling event that begins on day 103 does not reset until the upwelling event on day 137 (Fig 2.2).

The response to the downwelling winds can be seen in the currents as well. At the onset of downwelling winds alongshelf currents at C1 and S1 switch from weak or up shelf flows to strong down shelf flows (Fig 7a). Flows at N1 (not shown) are much more variable due to its position near the estuary mouth and also possibly influenced by the presence of a recirculating bulge, as described by Chant et al. (2008). Flows at C3 are weak during the day 146-150 downwelling event, while flows at C1 are strongly flowing

downshelf at around 0.4 m/s showing that during this event the coastal current was narrower and missed the C3 mooring as also suggested by the higher salinities at C3 during this event.

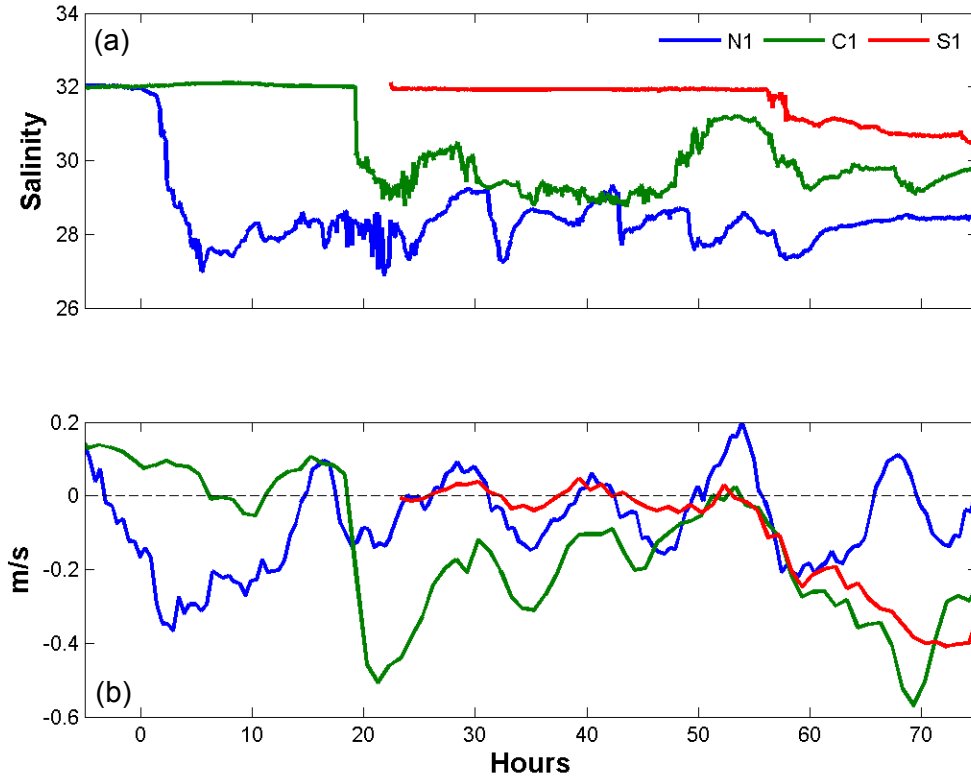


FIG. 2.5. (a) Surface salinity and (b) alongshore near surface velocity at N1 (blue), C1 (green), and N1 (red) during first downwelling event. Hour zero corresponds to the moment the buoyant coastal current arrives at N1 and is equivalent to Day 103.7014

#### 2.4.2. Propagation speeds

For each of the four typical downwelling events we calculate the propagation speed of the nose of the plume based on the arrival time of the buoyant plume at the moorings which is marked by a sudden decrease in the surface salinity at the mooring. For this analysis,

we calculate the speeds between the N1 and C1 moorings and the C1 and S1 moorings, the results of which are presented in Table 2.1. The propagation speeds between N1 and C1 range from 0.26-0.49 m/s and the propagation speeds between C1 and S1 are 0.03-0.20 m/s slower.

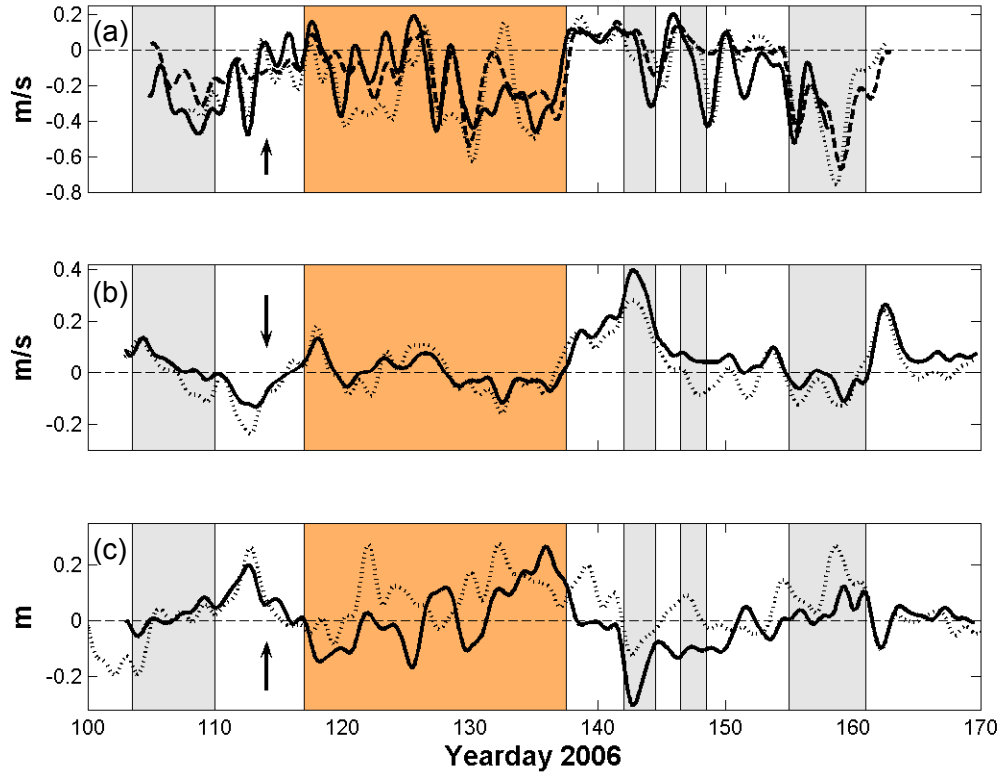


FIG. 2.7. (a) Depth averaged velocities at C1 (solid), C3 (dashed), and S1 (dotted). (b) Depth averaged velocities at SV1 (solid) and SV2 (dotted). (c) Shelf valley pressure gradient (solid) and filtered sea level at Sandy Hook multiplied by a factor of 5 (dotted). Positive shelf valley pressure gradient values represent a higher set up at SV1. Gray shaded areas signify periods of downwelling wind with a typical coastal current propagating along the coast, orange shaded area signifies period of coastal current detachment, arrow at day 114 denotes time of high discharge



The propagation speed for an unforced surface advected plume can be estimated to be the internal wave speed,  $c = (g'h)^{1/2}$  (Lentz and Helfrich, 2002; Fong and Geyer, 2002). The data for the Hudson River plume suggests that the plume is in fact surface advected and does not contact the bottom. Using data from the C1 mooring, the depth of the plume ( $h$ ) is estimated as the depth of the greatest velocity shear and the density profile is considered linear between CT sensors. The internal wave speed at C1 is calculated and is summarized in Table 2.1 as well. The internal wave speed at C1 falls between the observed propagation speeds between N1-C1 and C1-S1 with the exception of the day 143 downwelling event.

TABLE 2.1. Comparison of observed propagation speeds (m/s) between N1 – C1 and C1 – S1 and the internal wave speed measured at C1 with wind speed and direction. Wind direction is in oceanographic notation (i.e. where the wind is flowing toward) with 0/360(180) degrees being north(south) and 90(270) degrees being east(west). Wind speed and direction are from the unfiltered wind record at the onset of the downwelling event.

Onset Time	$\Delta x / \Delta t_{\text{arrival}}$		$(g'h)^{1/2}$	Wind	
	N1=>C1	C1=>S1		Direction (degrees)	Speed (m/s)
C1			C1		
104.5	0.41	0.21	0.24	116	3.1
143.45	0.26	0.23	0.3	129	13.7
147.61	0.49	0.29	0.33	155	2.9
155.13	N/A	0.62	0.64	197	7.0

The difference between the actual propagation speed and the estimate of the internal wave speed highlights the effect of slight variations in direction of the downwelling winds on plume propagation speeds. Just prior to the arrival of the plume at

C1 for the first downwelling event starting on day 103, the wind is very weak and downwelling with an offshore component. This allows the actual propagation speed to be close to the internal wave speed estimate since the wind is not strong enough to significantly alter the plume structure. This is also true for the third event on day 147. The wind for the second event, starting on day 143, is relatively strong and has a significant offshore component. This affects the propagation speed of the plume through the additional effect of a downstream Ekman velocity and possibly causing the plume to widen as well. Due to the strong offshore component of this wind event, the sea level at Sandy Hook drops, leading to an upstream geostrophic flow that opposes the plume's downstream propagation speed, slowing it down. The last event on day 155 both the observed propagation speed and the internal wave speed are significantly quicker than the preceding events. During this time period there is a large discharge event and a moderate downwelling wind that is closely aligned with the New Jersey coast. This increase in buoyant forcing along with the alignment of the downwelling wind stress that does not significantly alter the plume structure, leads to a faster downstream propagation.

#### *2.4.3. Freshwater transport*

In an attempt to approximate the amount of freshwater transported by the coastal current, salinity and ADCP current data are used to determine freshwater fluxes at the C1 and C3 moorings. The salinity data is linearly interpolated over the water column and assumed to be constant between the top CT sensor and the surface. To fill in bad bins in the velocity data near the surface the vertical shear is assumed to linearly go to zero at the surface. The freshwater flux is then calculated using

$$FW_{cc}(z, t) = \int_{z_0}^{\eta} v(z, t) * (s_o - s(z, t)) / s_o dz \quad (2.2)$$

where  $v$  is the interpolated velocity profile,  $s$  is the interpolated salinity profile,  $s_o$  is the salinity at the innershelf moorings before the 1<sup>st</sup> downwelling event,  $z_o$  is the depth of the first good ADCP bin and  $\eta$  is the sea surface elevation. This yields units of a volume flux of freshwater per unit width. The freshwater transport is plotted in Figure 2.8. The results of this formulation reveal that for the downwelling events on days 142 and 146 the freshwater transport at C3 is very weak and while the currents are flowing downstream during that time period, the buoyant coastal current does not extend to the C3 mooring.

Multiplying the freshwater flux calculated using (2) at the C1 mooring by an estimate of the width of the buoyant coastal current yields an estimate of the freshwater transport in the plume. The width of the plume is assumed to be the internal radius of deformation. The freshwater transport is averaged over the period of the four downwelling events starting on days 103, 142, 146, and 155. The estimates are plotted in Figure 2c (denoted with ‘\*’) along with the Hudson River discharge. The freshwater transport estimates are close the measured discharge from the Hudson River for the day 103 and 155 events, and noticeably underestimated for the day 142 and 146 events. As with the plume nose propagation speeds, this discrepancy between river input (gauged value) and estimates made with the mooring data highlights the importance of subtle deviations of the wind direction from a true alongshore direction on plume structure and freshwater transport. During a weak wind forcing and a true alongshore wind forcing the approximation of the plume width with being equal to the internal Rossby radius is valid, while when the wind stress has an offshore component (day 142 and 146) the overall plume structure is fundamentally altered. The offshore component of the wind can widen

the plume, invalidating the Rossby radius width approximation. The wider plume prevents the mooring array from fully capturing the density and velocity structure of the plume, leading us to under estimate the freshwater content and downstream velocity. Bulge formation can also play a role in the reduced freshwater transport estimates, as seen during the day 142 downwelling event where a large bulge region is present (higher chlorophyll areas in Fig 2.9b) and the shelf valley flows bisect the bulge region.

The freshwater flux for the downwelling wind period starting on day 118 is in stark contrast to the four typical downwelling events described above. During this period the freshwater flux at C1 fluctuates between flowing north and south while the flux at the C3 mooring remains weakly southward (Fig 2.8). As we will describe in the next section, it is during this period that the coastal current detaches from the coast and forms a recirculating bulge region downstream of the estuary mouth in the vicinity of the C mooring line. It is suggested that such a feature is not uncommon along the New Jersey coast from the studies of Yankovsky and Garvine (1998), Munchow and Chant (2000), and Yankovsky et al. (2001), all of which allude to a recirculating eddy slowly propagating along the New Jersey coast that has the potential to significantly alter the freshwater transport timescale. Specifically, Yankovsky and Garvine (1998) noted a time lag of more than a month between a discharge event in the Hudson River and the arrival of buoyant water near Atlantic City, NJ, approximately 160 km downstream of the Battery in New York. This estimation is several times longer than the timescale associated with a coastally trapped gravity current. We suggest that this buoyant quasi-steady/slowly propagating recirculating feature can significantly slow the downstream propagation of freshwater, which can explain the discrepancy between these two

freshwater transport timescales. The formation of this feature is found to be more complex than previously described in Yankovsky et al. (2001).

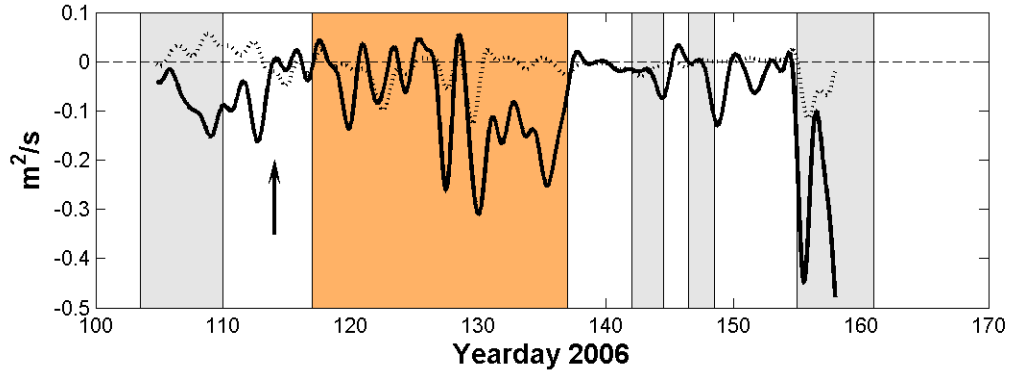


FIG. 2.8. Freshwater flux calculated at C1 (solid) and C3 (dotted). Gray shaded areas signify periods of downwelling wind with a typical coastal current propagating along the coast, orange shaded area signifies period of coastal current detachment, arrow at day 114 denotes time of high discharge

## 2.5. Downstream Detachment and Recirculation

Starting on day 117 to approximately to day 137 the freshwater plume is observed to have been detached from the coast and formed a recirculating feature downstream from the outflow region. This is seen in the higher chlorophyll areas, which qualitatively signify freshwater in Figure 9a and also from the shipboard velocity and salinity data in Figure 10a. The time period this feature was evident along the coast is marked by orange shaded areas in the time series plots. The detachment and recirculating bulge region was first observed in the satellite chlorophyll data on day 117 (Fig 2.9a) and was destroyed on day 137 during the upwelling wind event that caused salinity to return to background values (Fig 2.2). The downwelling event starting on day 118 is similar to the other events

previously discussed in that the downwelling event is preceded by a brief upwelling period. However, in this instance the surface salinity response at the inner shelf moorings differs. There is a rapid initial freshening at N1, but salinity response at C1 and S1 is much slower and more gradual due to the presence of the downstream bulge region. Preceding this downwelling event on day 118 is a period of strong onshore winds peaking during day 112, which is followed by a large discharge event centered on day 114. The strong onshore wind around day 112 leads to a high sea level setup along the coast as measured at Sandy Hook, NJ (Fig 2.7c) which reverses the subtidal flow in the Hudson River as discussed in Section 2.3. and depicted in Figure 2.3. This sea level setup results in the formation of a geostrophic current along the coast as observed in the current velocities at the C1 and S1 moorings (Fig 2.7a). Following the onshore winds there is a brief period of upwelling winds on day 117. During the transition between the onshore and upwelling winds there is a period of weak winds leading to the large discharge from the Hudson River (Fig 2.2, 2.5).

At the onset of the downwelling event on day 118, following the brief upwelling on day 117, satellite chlorophyll data shows a large bulge starting near the C-line moorings that appears to have anti-cyclonic rotation (Fig 2.9a). Currents during the same time show a northward flow at the C-line moorings due to the downstream bulge feature, while flows at S1 remain south. Shelf valley currents during this time are flowing strongly up-canyon implying strong canyon upwelling and a strong lateral velocity shear. This strong lateral shear between the buoyant current and the shelf valley currents possibly plays an important role in the formation of the downstream bulge by restricting cross-valley transport of the plume during the upwelling winds.

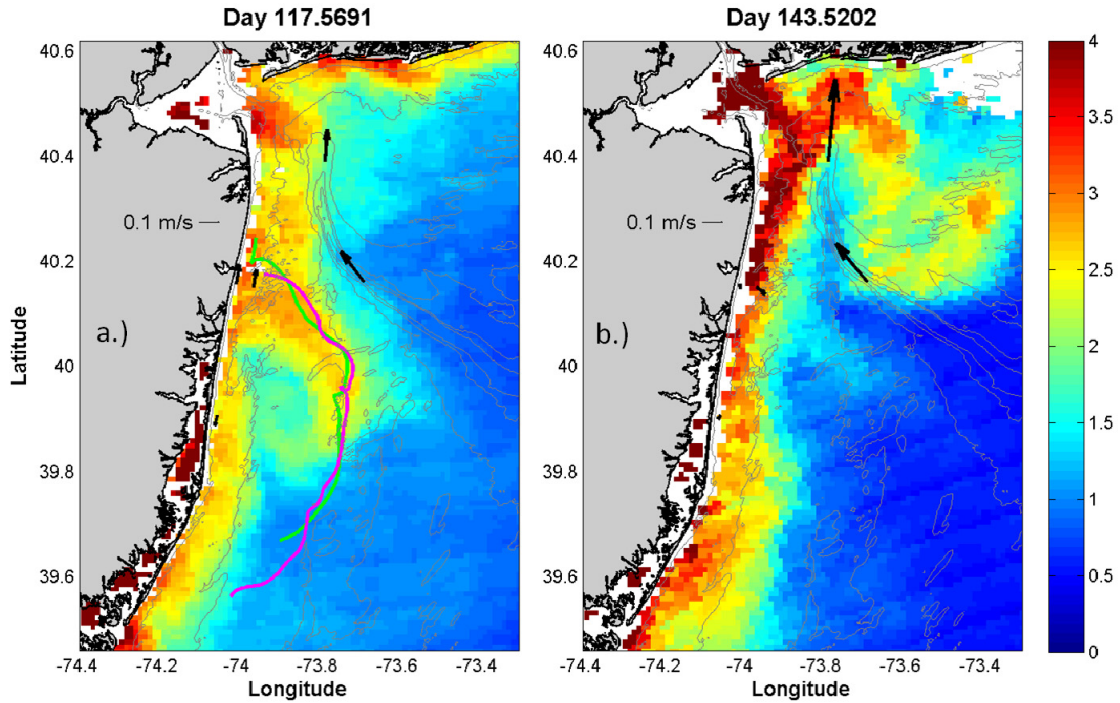


FIG. 2.9. Satellite chlorophyll data with C1, C3, S1, SV1 and SV2 depth averaged currents from yearday 117.5691 (a) and yearday 143.5202 (b). Drifter tracks in (a) are denoted by the green and magenta lines, which were tracked between days 124-129

Ship transects taken approximately 1 week after the beginning of the day 118 downwelling event confirm that the core of the buoyant current becomes detached from the coast and that some buoyant water flow northward in a weak return flow (Fig 2.10a) in the vicinity of the C mooring line. Drifters were placed in the water near the coast north of the C-line moorings on day 124 and were followed until day 129. The tracks of the drifters closely follow the edge of the detached coastal current (Fig 2.10a). The average velocity of the drifters over their deployment length was approximately 0.3 m/s. Remarkably, the bulge remained relatively persistent and constant in structure over the nearly 2 weeks of sampling and variable wind forcing. Note that tidal currents have not

been removed from the shipboard velocity data. However, with the exception of the southernmost transects, this effect is minimal in terms of capturing the downstream bulge structure with the offshore velocity maximum and salinity minimum well correlated with satellite chlorophyll images and drifter tracts, all of which occurred at different time periods during period the downstream bulge was present.

Using the cross-shore ship transects of salinity, a freshwater inventory was calculated using the formulation

$$FW = \iint \frac{s_o - s}{s_o} dz dx \quad (2.3)$$

where  $s_o$  is the background salinity on the shelf,  $dz$  is the bin size,  $dx$  is the cross-shore distance between samples, and  $s$  is the measured salinity. The results are plotted in Figure 10b. A total freshwater inventory of the sampling area is obtained by multiplying the values by the alongshore distance between transects and summing the values. This calculation yields a freshwater inventory of  $1.51 \cdot 10^8 \text{ m}^3$  of freshwater. This value represents approximately the previous three days worth of discharge from the Hudson River, which is also the advective time scale of the downstream bulge region based on the drifter trajectories.

The surface velocities at the C1 and S1 moorings also show the difference in responses to the downwelling wind events and evidence of a recirculation in the downstream bulge region. During the downwelling events on days 142, 146, and 155, the currents turn to the south at both locations and then decrease and turn north in response to the change in wind direction to upwelling winds (Fig 2.7a). At the onset of day 118 downwelling event there is an initial increase in southward flow at both locations; however, after day 120 flows at C1 turn to the north and then oscillate for a week under



steady downwelling winds until day 126 when there is a brief upwelling wind event. During this time period of flow reversals the salinity at C1 continues to gradually decrease, indicating that there is a source a freshwater coming from the south due to the presence of the downstream eddy.

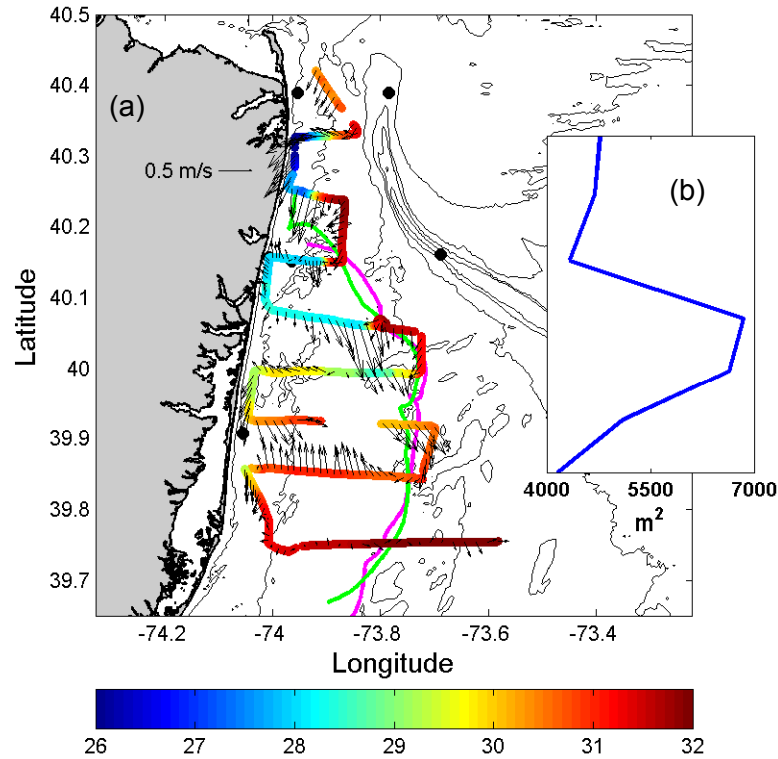


FIG. 2.10. (a) Shipboard near surface currents and salinity. Drifter tracks are denoted by the green and magenta lines. Shipboard surveys occurred on day 123; drifters were tracked between days 124-129. (b) Freshwater content calculated at the cross shore transects

While currents at C1 are variable, currents at S1 during the day 118 downwelling event remain consistently southward during the duration of the event. The salinity at S1 also decreases gradually during the event in a similar way as C1 implying that freshwater is leaving the downstream bulge and reforming the buoyant coastal current. This

downstream bulge recirculation pattern persists until day 137 when the system resets during a strong upwelling wind event. At this time the currents at C1 and S1 become coherent and the salinity at both stations return to background values.

#### *2.5.1. Hudson Shelf Valley response*

Hudson Shelf Valley (HSV) currents are generally directed along the axis of the valley, while cross-valley current variability increases as distance from the bottom increases. The along-canyon flows are best correlated with the along-canyon barotropic pressure gradient, where a high setup offshore would drive up valley flows and high setup near shore would drive down valley flows, which is similar to that described in Harris et al. (2003). These barotropically forced flows interact with the Hudson River outflow due to the proximity of the Hudson's discharge to the apex of the HSV (Zhang et al., 2009).

A dramatic example of this interaction between the barotropic HSV flows and the Hudson River plume occurs during the downwelling event on day 142. As noted previously, the winds during this event had a strong offshore component and an orientation that nearly aligns with the axis of the HSV. This wind orientation favors bulge formation near the mouth of the estuary, transporting water cross-shore over the head of the HSV while also driving a strong up valley flow in the HSV (Fig 2.7b,c). These strong flows actually shear the bulge region, trapping a large portion of the buoyant discharge to the east of the HSV and along the Long Island coast (Fig 2.9b).

This interaction between the HSV and the Hudson River plume is important in the formation of the downstream bulge region on days 117-137. On day 112 is the onset of a strong onshore wind that drives a sea level set up on the coast and strong down valley flows in the HSV (Fig 2.7b,c). After the wind relaxation and high discharge event on

days 114-115, there is a brief upwelling period that drives a set down on the coast, up valley currents in the HSV, all the while transporting the buoyant outflow towards the head of the HSV (Fig 2.7b,c). As is evident in Figure 2.10a, the offshore edge of the plume is trapped along the western edge of the HSV. Here we suggest that in the absence of the barotropically forced HSV flows, a more radially expanding bulge region would develop. However the HSV flows limit the bulge formation, preventing the buoyant water from crossing the HSV and eventually leading to the bulge region to be deformed in the downstream direction as we describe in the following section.

## 2.6. Discussion

In the previous sections we have described a downstream recirculating feature off the New Jersey coast that persists for a period of approximately two weeks under variable wind forcing. This event was preceded by a strong onshore wind followed by a very brief upwelling period, with a high discharge event occurring between these events. Here we will answer some questions that still remain: (i) how this feature forms on the shelf, (ii) what is the wind strength required to destroy the feature, and (iii) what are the implications of this feature on freshwater transport on the shelf.

### 2.6.1. *Downstream bulge formation*

Yankovsky et al. (2001) described a seemingly similar feature that was observed on New Jersey shelf during a study in 1989. The formation of this feature was attributed to a pulse in river discharge that leads to a detached buoyant recirculating bulge region transported downstream. Here, we propose an additional mechanism for the formation of

a downstream buoyant recirculating feature involving the buoyant plume interacting with wind driven shelf circulation that is impacted by the Hudson Shelf Valley.

During periods of upwelling winds a mid-shelf jet has been observed to develop along the southern and onshore edge of the Hudson Shelf Valley and flowing away from the outflow region. Studies have noted that this mid-shelf jet can be an important conduit for transporting freshwater from the Hudson River cross-shelf during the summer upwelling season (Castelao et al., 2008; Zhang et al., 2009). Zhang et al. (2009) discovered that the Hudson Shelf Valley is vital for the formation of the mid-shelf jet based on model simulations with and without the shelf valley. During the summer upwelling period there is a distinct mid-shelf freshwater pathway located on the onshore side of the valley, while the freshwater transport is much more diffuse in that region without the shelf valley. Zhang et al. (2009) noted that the shelf valley had a notable impact on the pressure gradients on the shelf and that this difference explains the different freshwater transport pathways for model runs with and without the shelf valley. However, through what process or processes the shelf valley impacts the pressure gradients on the shelf was not examined in their study.

Preceding the formation of the downstream recirculating feature on day 118, there was a large discharge event on day 114. This event discharged a large amount of freshwater onto the shelf during a period of weak winds (Fig 2.2); conditions which have been found to favor the formation of a radially expanding bulge region (Chant et al., 2008). Quickly following the discharge event on day 114 was an upwelling wind event on day 117 which lasted approximately 1 day. It was after this upwelling event that the recirculating feature was observed.

The data suggest that during the brief upwelling wind on days 117-118 the buoyant plume is transported a short distance offshore. Since the upwelling event was short lived, so was the mid-shelf jet. At the cessation of the upwelling winds the mid-shelf jet dissipated, stopping the transport of the recently discharged buoyant water. After the dissipation of the mid-shelf jet the tongue of buoyant water that is now offshore under goes a geostrophic adjustment, forming the recirculating feature that was observed from day 118-137. A schematic of this process is illustrated in Figure 2.11, where Figure 2.11d represents the plume structure derived from in the satellite chlorophyll, depth averaged currents, and drifter data in Figure 2.9a.

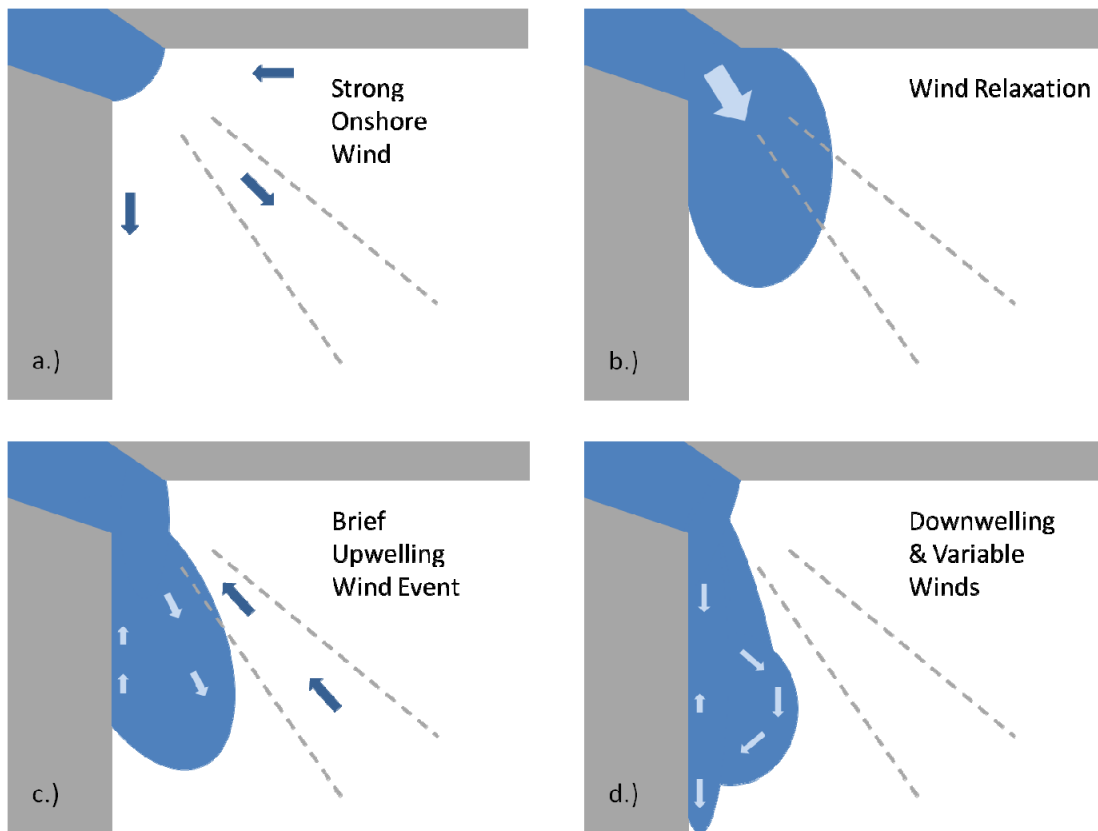


FIG. 2.11. Schematic showing the formation of the downstream buoyant eddy

The timing of the pulsed buoyant discharge and the period of upwelling winds, along with the duration of the upwelling winds are vital to the formation of this feature, which can explain why the feature is not more ubiquitous on the New Jersey shelf. It should be noted that the feature described by Yankovsky et al. (2001) on the New Jersey shelf formed under similar forcing conditions (their Figures 17 and 18), giving credence to the possibility that it was formed by the same mechanism.

### *2.6.2. Wind strength and duration*

One of the more remarkable observations of the downstream bulge feature is how it persists for a period of 19 days under a variety wind forcings. In the absence of wind forcing and shelf currents, a buoyant plume propagates downstream due to the difference in density between the ambient water and the plume. As a wind stress is applied to a buoyant plume and gradually increased, there will come a point when the flow in the plume ceases to be driven by buoyancy and becomes heavily influenced by the wind stress (Garvine, 1995; Whitney and Garvine, 2005). Here we will use a similar theory to that developed by Garvine (1995) and Whitney and Garvine (2005) to show that the longevity of the downstream feature is due to the interplay between the buoyant forcing and wind stress.

Garvine (1995) developed a non-dimensional scaling of the momentum equations for a buoyant river plume, and noted that if the non-dimensional wind stress term is greater than the pressure gradient term, the plume would be primarily a wind-driven current while if the pressure gradient term dominated, the flow would be driven by the buoyant forcing. Whitney and Garvine (2005) built on this scaling and came up with a wind strength index,  $W_s$

$$W_s = \frac{u_{wind}}{u_{geos}} \quad (2.4a)$$

Where,

$$u_{geos} = c/K \quad (2.4b)$$

$$u_{wind} = \sqrt{\frac{\rho_{air}}{\rho} \frac{C_{10}}{C_{Da}}} U \quad (2.4c)$$

Here  $U$  is the along-shelf wind velocity,  $c = \sqrt{g'h}$  is the internal wave speed,  $g'$  is the reduced gravity,  $h$  is the plume depth,  $K$  is the Kelvin number ( $K = W/R_{di}$ ), where  $W$  is the plume width and  $R_{di} = c/f$  is the internal Rossby radius. The  $u_{wind}$  term is simply a wind driven frictional velocity where  $\rho_{air}$  is the density of the air,  $C_{10}$  is a surface drag coefficient for a 10 m wind, and  $C_{da}$  is an interfacial drag coefficient for a surface advected plume. The wind strength index ( $W_s$ ) used here (2.4a) is similar to a Wedderburn number which describes the relative strength of the buoyancy and wind forcing terms. The Wedderburn number has typically been used in examining the influence of wind strength and stratification on upwelling and seiche in lakes (e.g. Thompson and Imberger, 1980; Monismith, 1987). More recently, the Wedderburn number has been used in studies examining the effect of along channel winds on estuarine structure and circulation (Geyer, 1997; Chen and Sanford, 2009). As opposed to the traditional definition of a Wedderburn number which defines the length scale  $L$  as the along channel distance, we (as does Whitney and Garvine (2005)) define  $L$  as the width of the plume. Starting with a Wedderburn number of the form

$$W = \frac{\tau_w L}{\Delta \rho g h^2} \quad (2.5)$$

where  $\tau_w$  is the alongshore wind stress and  $L$  is the plume width, and assuming that  $L$  is a factor of the internal Rossby radius,  $L = \alpha c/f$ , then (6) can be rewritten simply as

$$W = \alpha \frac{u_{Ekman}}{c} \quad (2.6)$$

Here,  $u_{Ekman}$  is the cross plume Ekman velocity driven by the alongshore winds,

$u_{Ekman} = \tau_w / \rho f h$ . When  $|W| > 1$ , the flow is heavily influenced by the wind stress, and when  $|W| < 1$ , the flow is dominated by the buoyant forcing.  $W$  is positive for upwelling winds.

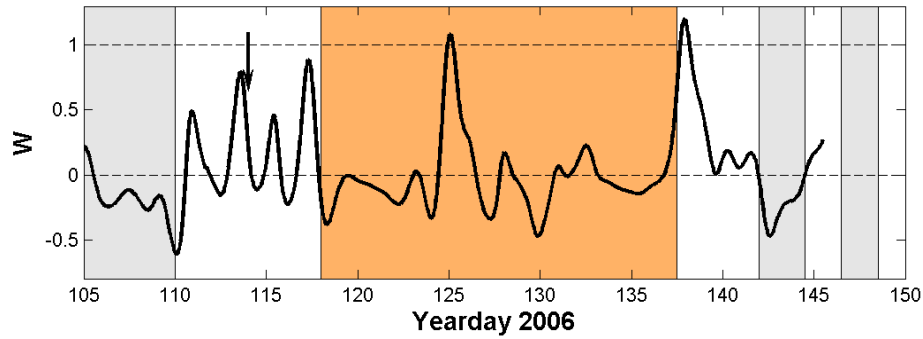


FIG. 2.12. Wedderburn number calculated at N1. Positive (negative) values indicate upwelling (downwelling) winds. Gray shaded areas signify periods of downwelling wind with a typical coastal current propagating along the coast, orange shaded area signifies period of coastal current detachment, arrow at day 114 denotes time of high discharge

$W$  is calculated using data at the N1 mooring since the plume is still attached to the coast during the detachment observed at C1 on days 117-238. The width factor  $\alpha$  is set to 1.0 for this analysis. This agrees with previous studies (Lentz and Helfrich, 2002; Chant et al., 2008) which state that  $\alpha$  is typically  $O(1)$ , as do estimates of  $\alpha$  from the shipboard surveys conducted during this study near the N1 mooring. This leaves  $W$  as the ratio of the cross plume Ekman velocity and the downstream buoyancy driven flow.



It is important to note that two of the maximums in  $W$  on days 117 and 138 bracket the time period the feature is present on the shelf (Fig 2.12). The wind stress on day 117 was just enough to start to move the buoyant water offshore and the upwelling wind stress on day 137 was enough to destroy the feature. During the 20 days in between the wind stress was not strong enough to overcome the buoyant forcing and was unable to destroy or significantly modify the downstream bulge feature with the notable exception of the upwelling wind on day 125. During that event  $W$  is greater than 1 (Figure 2.12) and there is a corresponding increase in salinity at N1 (Fig 2.2a). However, the salinity response is muted and currents remain variable at the C moorings immediately after this event (Fig 2a, 7a) suggesting that the wind did not have a significant impact on the structure of the downstream bulge until day 138.

### *2.6.3. Implications for freshwater transport on the NJ shelf*

Zhang et al. (2009) reported three main freshwater transport pathways on the New Jersey shelf: New Jersey coast, Long Island coast, and mid-shelf pathways. The New Jersey coast pathway dominates when winds are downwelling and a buoyant coastal current forms. Typically this pathway leads to a rapid downshelf propagation of Hudson River water while decreasing the cross-shore transport (Zhang et al., 2009). In the case of a detached bulge region, the cross-shore transport would increase in the area of the bulge, while slowing downshelf transport downstream of the detached bulge due to possible retention in the recirculation region. This shift can have impacts on the biogeochemical processes occurring in the coastal region, including a shift in the location of high productivity, as can be seen in Figure 2.9a.

## 2.7. Summary

In this paper we have described the response of a buoyant river plume to variable wind, buoyant, and shelf forcings in a region with complex bathymetry and geometry. Typical downwelling responses are observed where the buoyant coastal current formed and generally propagated downstream close to the internal wave speed. Deviations of the observed propagation speed from the internal wave speed can be attributed to differences in the wind stress direction from a pure along shore wind stress as is demonstrated during the day 143 event. Upwelling winds follow the downwelling winds and transport the buoyant water offshore where it mixes with the ambient shelf water, essentially resetting the system. Estimates of freshwater transports at the C mooring line are also calculated using the internal Rossby radius as an estimate of plume width. This estimation is found to be valid for periods of weak or true downwelling winds, but is invalid if the winds have a strong offshore component since offshore winds cause the plume to widen.

A downstream recirculation feature is also described. Its formation is attributed to onshore winds coinciding with a large discharge event, followed by a brief period of upwelling winds and an extended period of downwelling winds. The relaxation of the strong onshore winds during the large discharge event leads to a large buoyant discharge onto the shelf. This large buoyant plume is then transported offshore, though limited by the presence of the HSV. Buoyancy is now the dominant forcing term and the plume geostrophically adjusts, forming the downstream recirculating feature. This feature persists for approximately 2 weeks until the winds are strong enough to reset the system, which is consistent with a Wedderburn number scaling. The downstream feature described here can significantly impact the freshwater transport time along the coast of

New Jersey and can begin to explain the differences between the long transport timescale described by Yankovsky and Garvine (1998) and the shorter transport timescale associated with a coastally trapped internal wave.

# **Chapter 3:**

## **Impact of Offshore Winds on a Buoyant River Plume System**

## Abstract

Idealized numerical simulations utilizing the Regional Ocean Modeling System (ROMS) are carried out to examine the response of buoyant river plume systems to offshore directed wind stresses. It is found that after a few inertial periods of wind forcing the plume becomes detached from the coast and reaches a steady-state in terms of the plume's offshore position, width, and plume averaged depth, salinity, and velocity. The steady-state offshore position of the plume is a balance between the cross shore advection driven by the estuarine outflow and the alongshore advection driven by the Ekman velocities, and is described using the ratio of the outflow Froude number and the plume Froude number. The steady-state salinity structure is maintained by a balance between the cross-shore advection of salt creating stratification, the turbulent vertical mixing, and the downstream transport of freshwater continually resetting the system. Plume mixing is also analyzed using a salinity coordinate system to track the changes in freshwater volume in salinity space and time. A dynamical plume region classification is developed with use of a Richardson number based critical mixing salinity criteria in salinity space. This salinity class based classification agrees well with a classification based on an alongshore analysis of the salt flux equation. For this classification the near-field is dominated by large cross-shore fluxes, the mid-field by a diminishing cross-shore salt flux, and in the far-field a balance between the alongshore salt flux and turbulent mixing.

### 3.1. Introduction

When buoyant estuarine water is discharged into the coastal ocean it is deflected to the right (in the northern hemisphere) and forms a coastally attached plume that propagates downstream in the direction of Kelvin wave propagation. How this buoyant coastal plume is transported across the continental shelf and eventually mixes with the saltier ambient shelf water is important for the understanding of shelf wide circulation and biogeochemical processes. Strong vertical velocity shear driven by the estuarine outflow dominates mixing at the mouth of the estuary (MacDonald et al. 2007) and wind is the dominant mixing mechanism in the far field plume due to the plume's tendency to be confined to a thin surface layer (Garvine 1995, Hetland 2005).

Cross-shelf transport on the shelf is thought to be driven mainly by alongshore winds through an Ekman transport in the surface layer. At the coast, this can lead to an upwelling of bottom water from the bottom layer or a downwelling of water from the surface layer. Downwelling winds impact a buoyant coastal current by transporting the buoyant water against the coast and steepening the isopycnals, leading to an enhanced downstream transport (Moffat and Lentz 2012). Upwelling winds cause the offshore edge of the plume to mix to a critical depth and begin to be transported offshore. The plume then becomes detached from the coast and the plume continues to entrain salty ambient water and deepen due to mixing on the offshore edge driving by an Ekman straining mechanism. The plume is continually transported across the shelf and mixes until it becomes undistinguishable from the ambient shelf water (Fong et al. 1998; Fong and Geyer 2001, Lentz 2004). Recently, progress has been made in recognizing the effects of cross-shelf winds on driving cross-shelf transport for an unstratified shelf

(Tillburg 2003, Fewings et al. 2008). It has been found in near shore regions where the surface and bottom Ekman layers interact, cross-shore winds can drive a significant cross-shore transport.

For a surface advected buoyant river plume, it is not expected that the surface and bottom boundary layers will directly interact, due to the strong stratification in the plume. Because of this it has been assumed that the cross-shelf transport due to offshore winds is insignificant when compared to alongshore winds since the Ekman transport is directed in the alongshore direction. However, it has still not entirely been explained how an offshore wind will impact the mixing and freshwater transport of a buoyant river plume. In the pioneering modeling study by Chao (1989) it is noted that an offshore wind lead to a spreading of the plume, but model limitations prevented a more thorough analysis. For a model of the Hudson River plume in the New York Bight with idealized wind and river forcings, it was also found that an offshore wind leads to a spreading of the plume in the cross-shore direction and the downstream velocity maximum in the plume develops near the offshore edge, impacting the freshwater transport (Choi and Wilkin 2007). Cross shore winds are a common feature globally, manifested as a sea-land breeze system or simply seasonal wind patterns, but the impacts of these cross-shore winds on buoyant coastal flows has been a relatively unexplored area.

This leaves several questions on the response of a plume system to offshore winds that we plan to answer in this study. How does the plume response evolve in time? What is the role of the estuarine outflow conditions on the far-field plume structure and position? Are the scalings for turbulent mixing, plume depth, and velocity for alongshore winds relevant for cross-shore winds?

Using idealized numerical model domains and forcings, this study will describe the response and structure of a buoyant plume to steady offshore winds. Section 2 will describe the background theory for calculating several plume parameters, Section 3 will describe the numerical model and forcing set-up, Section 4 will examine the model results and compare them to the background theory, and in Section 5 we will discuss the results and their implications.

## 3.2. Plume Properties

Here we develop scalings for the vertical mixing, plume depth, velocity, and density.

These scalings are based on those from studies of the upwelling response of river plumes (Fong and Geyer 2001, Lentz 2004) since the underlying response of a buoyant surface layer should remain the same regardless of the direction of the wind stress. The parameterizations of plume properties in this section are based on results from this study that show the plume has become detached from the coast in response to the offshore wind stress and has reached a relative steady state in terms of cross-shore plume structure and offshore position after a few inertial periods.

### 3.2.1. *Plume depth*

The depth to which the plume mixes to can be calculated using a critical bulk Richardson number parameterization (Pollard et al. 1973, Trowbridge 1992, Fong and Geyer 2001, Lentz 2004),

$$Ri_c = \frac{g\Delta\rho_o h_p}{4\rho_a |\Delta u|^2} \quad (3.1)$$



where  $\rho_a$  is the ambient density,  $\Delta\rho_o$  is the density anomaly in the plume immediately after the onset of wind forcing,  $h_p$  is the plume thickness on the offshore side of the plume, and  $\Delta u$  is the velocity difference over the thickness of the plume. Here the velocity shear that contributes to the mixing of the plume is considered to be due to wind driven Ekman velocity. Since we are averaging over the width of the plume, the geostrophic velocities due to the cross-shore baroclinic pressure gradients in plume cancel out because the plume becomes detached from the coast and thus isopycnals must outcrop at both the offshore and inshore side of the river plume. Hence,  $\Delta u$  is considered to be  $U_e = \tau_w / \rho_a f$  divided by  $h_c$ . This alongshore Ekman velocity is substituted into (3.1) and solved for  $h_c$ , yielding an expression for plume thickness:

$$h_p = \left( \frac{4Ri_c \rho_a U_e}{g \Delta \rho_a} \right)^{1/3} \quad (3.2).$$

Here,  $Ri_c$  is a constant that typically has a value of 1. This is the same formulation derived by Fong and Geyer (2001) and Lentz (2004), except here it is shown to be effective for cross-shore wind response that reaches a steady-state structure. As in Fong and Geyer (2001) and Lentz (2004) the plume depth is dependent on the balance between the wind induced velocity shear driving the turbulent mixing and the plume's buoyancy suppressing the turbulent mixing. If the actual plume depth is shallower than the critical Richardson number based depth calculated in (3.2), then the plume will mix and deepen until the plume depth matches the critical depth.

### 3.2.2. Plume averaged velocity

The alongshore velocities in the plume are driven by the cross-shore pressure gradient and the downstream Ekman velocities. While the cross-sectionally averaged cross-shore baroclinic pressure gradient vanishes, the response of the sea-surface to the cross-shelf winds results in a non-zero cross shore averaged barotropic pressure gradient. This allows the plume averaged velocities to be written as simply the sum of the downstream Ekman velocity and the upstream barotropic velocity due to wind-driven sea level set-down at the coast,

$$v_p = v_{Ekman} + v_{barotropic} \quad (3.3),$$

where,

$$v_{Ekman} = \frac{\tau^{sx}}{\rho f h_p} \quad (3.4).$$

The barotropic velocity can be calculated by

$$v_{barotropic} = -\frac{g}{f} \frac{\partial \eta}{\partial x} \quad (3.5),$$

where,

$$\eta = \frac{u_*^2}{gH} x \quad (3.6).$$

Here,  $\tau^{sx}$  is the cross-shore wind stress,  $\rho$  is the density,  $f$  is the coriolis parameter,  $g$  is the gravitational acceleration,  $\eta$  is the sea surface elevation,  $H$  is the water depth, and  $x$  is the cross-shore distance. The frictional velocity,  $u_*$ , is written as  $(\tau^{sx}/\rho)^{1/2}$ .

### 3.2.3. Plume density

The estimate for plume average density is based on the formulation from Lentz (2004) for a plume response to upwelling winds. This theory is based on a conservation freshwater in a cross-shore transect of the plume,

$$\Delta\rho_o A_o = \Delta\rho_i A_i \quad (3.7).$$

Where the subscript  $i$  refers to the initial conditions and  $o$  refers to conditions after the onset of wind. This assumption works well for the upwelling wind case since the transect is essentially disconnected from the freshwater source; there is no upstream control in the upwelling case. This is not true for the offshore wind case since the wind is driving a significant downstream freshwater flux that can change dramatically during the first few inertial periods after the onset of the wind stress depending on the initial structure of the plume. This theory of freshwater conservation over time will not work for plumes where the river discharge is significantly larger than the initial freshwater transport downstream in the plume (for instance there is a large bulge region near the outflow). This setup leads to a large increase in freshwater transport at a downstream transect due to the advection of the bulge region downstream, which this theory does not account for. However, if initially there is no bulge region and the river discharge is close to the freshwater transport in the plume, the assumption of freshwater conservation is a valid one.

Using the theory of freshwater conservation, Lentz (2004) derives an expression for the plume averaged density difference,

$$\Delta\rho_o = \begin{cases} \Delta\rho_i \left(1 + \tilde{h}_p^2\right)^{-1} & \tilde{h}_p \leq 1 \\ \Delta\rho_i \left(A_i \tilde{h}_p\right) & \tilde{h}_p > 1 \end{cases} \quad (3.8),$$

where  $\tilde{h}_p$  is a normalized plume thickness,  $h_p/h_i$  at the offshore edge. Since  $\Delta\rho_0$  is required to solve for  $h_p$ , (3.8) is substituted into (3.2), yielding

$$\begin{cases} \tilde{h}_p^3 - \tilde{h}_s^2(\tilde{h}_p^2 + 1)/2 \approx 0 & \tilde{h}_s \leq 1 \\ \tilde{h}_p \approx \tilde{h}_s & \tilde{h}_s > 1 \end{cases} \quad (3.9).$$

Where  $\tilde{h}_s$  is a normalized plume thickness,  $h_s/h_i$ , and

$$h_s = \left( \frac{2Ri_c \rho_a U_E^2}{g h_i \Delta\rho_i} \right)^{1/2} \quad (3.10).$$

This reveals a formulation for the plume averaged density that is only dependent on the initial plume thickness ( $h_i$ ), density anomaly ( $\Delta\rho_i$ ), and the wind stress (contained in  $U_E$ ), all the while assuming that the freshwater transport into the cross-shore transect is equal to the freshwater transport out. Please refer to Lentz (2004) for a more thorough derivation and explanation.

### 3.3. Model Description

In this study we use the Regional Ocean Modeling System (ROMS, [www.myroms.org](http://www.myroms.org)) to examine the effects of offshore winds on a buoyant plume system. Shchepetkin and McWilliams (2005, 2009a) describe in detail the algorithms that comprise the ROMS computational kernel, and Haidvogel et al. (2008) (as corrected by Shchepetkin and McWilliams, 2009) discuss the validation of ROMS in a variety of oceanic settings. ROMS has been successfully deployed in the past for analyzing both realistic and idealized buoyant river plume (e.g. Choi and Wilkin 2007, Zhang et al. 2009, Hetland 2005).

The model set up used for the idealized simulations uses a 250x225 km domain. The domain includes a 120 km long channel with a depth of 10 m that serves as the river/estuary. The width of the estuary at the coast varies between 1-10 km. The coastline is a straight wall 10 m deep. The domain has linearly sloping bottom over the shelf region where the depth increases at a rate of 1m per 1000 m (Fig 3.1). On the offshore boundary a radiation boundary condition is implemented for 3-D momentum and tracers and Flather (1976) and Chapman (1985) boundary conditions for the free surface and 2-D momentum. The boundary is periodic on the up- and downstream boundaries. Over the time frame of the simulations, the buoyant plume does not interact with the boundaries. The model set up utilizes the generic length scale (GLS) k-kl mixing scheme. An M2 tide is forced on the offshore boundary to simulate more realistic mixing processes. No other shelf circulation is imposed initially at the boundaries. The temperature is set to a constant 10°C throughout the entire domain and the ambient shelf salinity is set to 32.

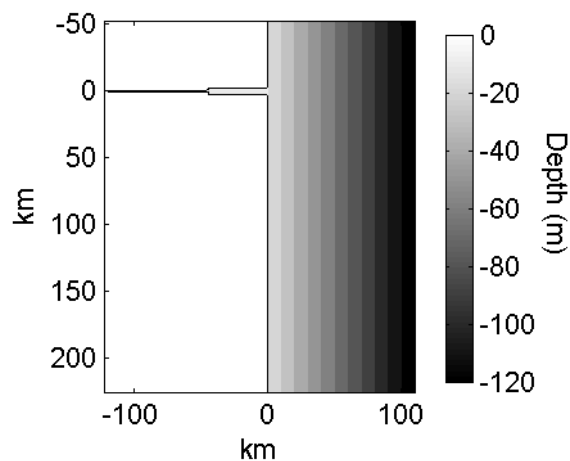


FIG 3.1. Model domain bathymetry for idealized ROMS simulations with a 5 km wide outflow.

The river discharge is forced at the head of the channel with a salinity value of 0 and is held constant over the duration of the run. The model is initialized by running the model with river discharge and no wind forcing until the estuary reaches a steady state salinity structure. Once the steady state salinity structure is reached, the shelf salinity is reset to 32 and the shelf velocity and sea surface is set to zero. The model is then run for 2 days to allow a plume to develop on the shelf. The wind forcing is confined to the cross shore directions. The wind stress is held to zero for the first 4 days of the simulation, allowing for an unforced plume to develop for 6 days. The wind stress is then ramped up over a period of a day to the maximum value where it is held constant for the remainder of the simulation (Fig 3.2). The ranges of discharge and wind stress values for the offshore wind simulations already completed are listed in Table 3.1.

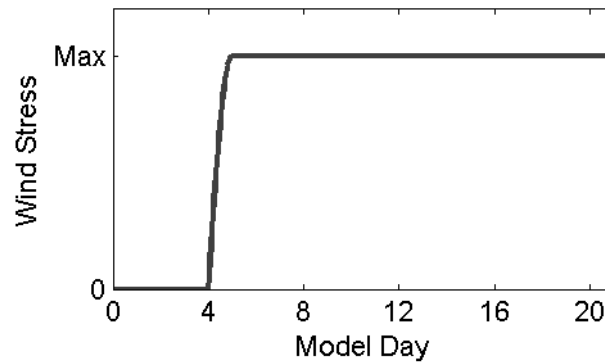


FIG 3.2. Plot of wind stress forcing for idealized simulations.

### 3.4. Results

#### 3.4.1. General plume response

Before the onset of the offshore wind stress there is a large, well defined bulge region near the mouth of the estuary and a narrow coastal current propagating downstream for the narrow outflow simulations. For the wide outflow simulations, the bulge region is more confined and the coastal current is wider, transporting a larger fraction of the freshwater discharge (Fig 3.3a, 3.4a). These initial plume structures generally agree with previous studies on the dependence of plume structure on outflow conditions (Fong and Geyer, 2002; Horner-Devine et al., 2006).

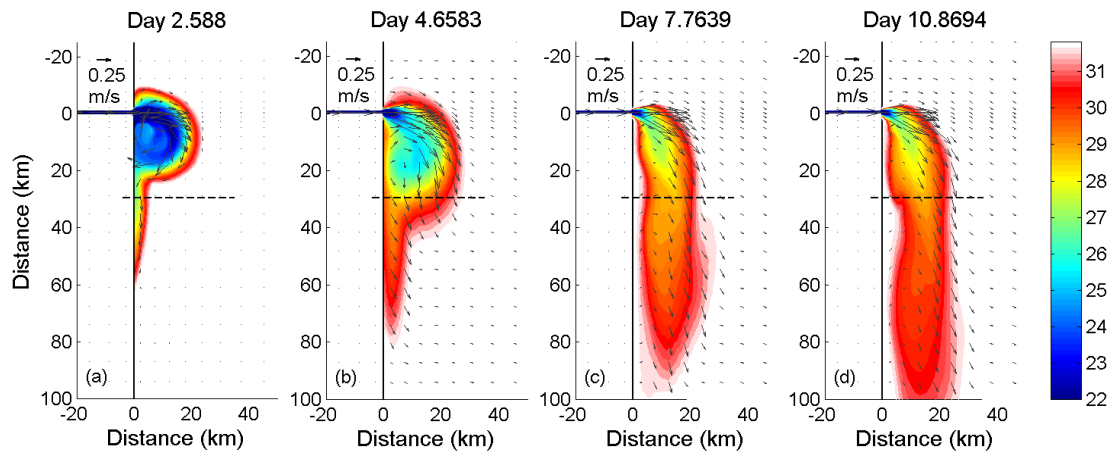


FIG 3.3. Tidally averaged surface salinity and velocity for Run 8 (1000m<sup>3</sup>/s, 0.1 N/m<sup>2</sup>, 1 km estuary) for period of no wind (a), onset of wind (b), 3 days of wind (c), and 6 days of wind forcing.

At the onset of the offshore wind stress (Day 4.65) the bulge region mixes and is advected downstream and the coastal current is initially slowly advected offshore (Fig

3.3b, 3.4b). After a few inertial periods of wind forcing, the plume structure has now reached a quasi-steady state with respect to the offshore distance, depth, velocity, and salinity. At this point there is no longer a discernible bulge region near the mouth of the outflow. There is now a strong downstream jet on the offshore side of the plume with a weak (sometimes upstream) flow on the inshore side. For the wide outflow case (Fig 3.4), the initial bulge region is reduced and the plume's offshore extent is less than the narrow outflow run.

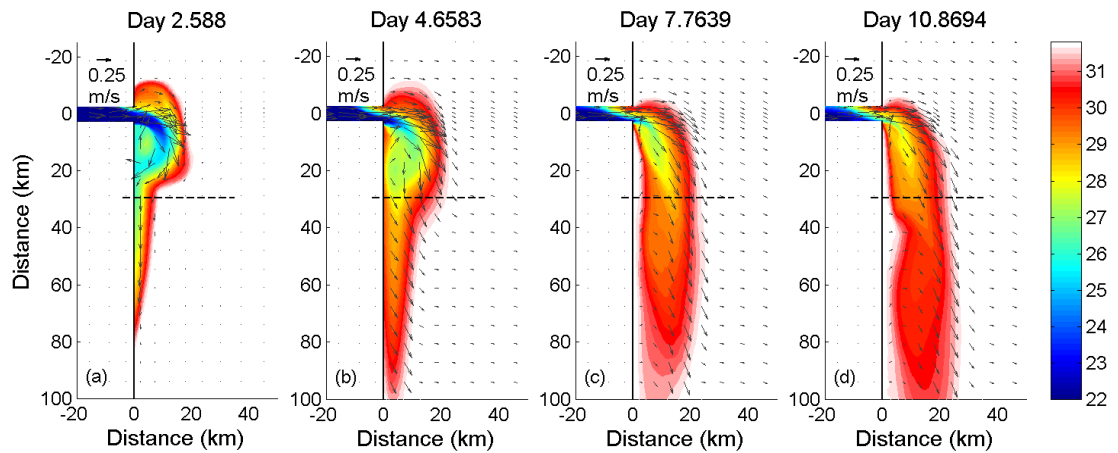


FIG 3.4. Tidally averaged surface salinity and velocity for Run 19 (1000m<sup>3</sup>/s, 0.1 N/m<sup>2</sup>, 5 km estuary) for period of no wind (a), onset of wind (b), 3 days of wind (c), and 6 days of wind forcing

At the onset of wind forcing the plume remains relatively thin, with the wide outflow plumes slightly thicker than the narrow outflow plumes. This difference in thickness is due to the wide outflow cases being more laterally sheared at the outflow than the strongly vertically sheared narrow outflow runs (not shown). Over the course of the initial response period, the wind induced vertical velocity shear leads to mixing at the



base of the plume, leading to an increase in plume density and a thickening of the plume as seen in far the narrow outflow run 8 in Figure 3.5a,d when the plume mixes from 4 m deep during the onset of the wind to over 6 m 3 days later. The same is true for the wide outflow case of run 19 that mixes from 5 m to 7 m deep (Fig 3.6a,d).

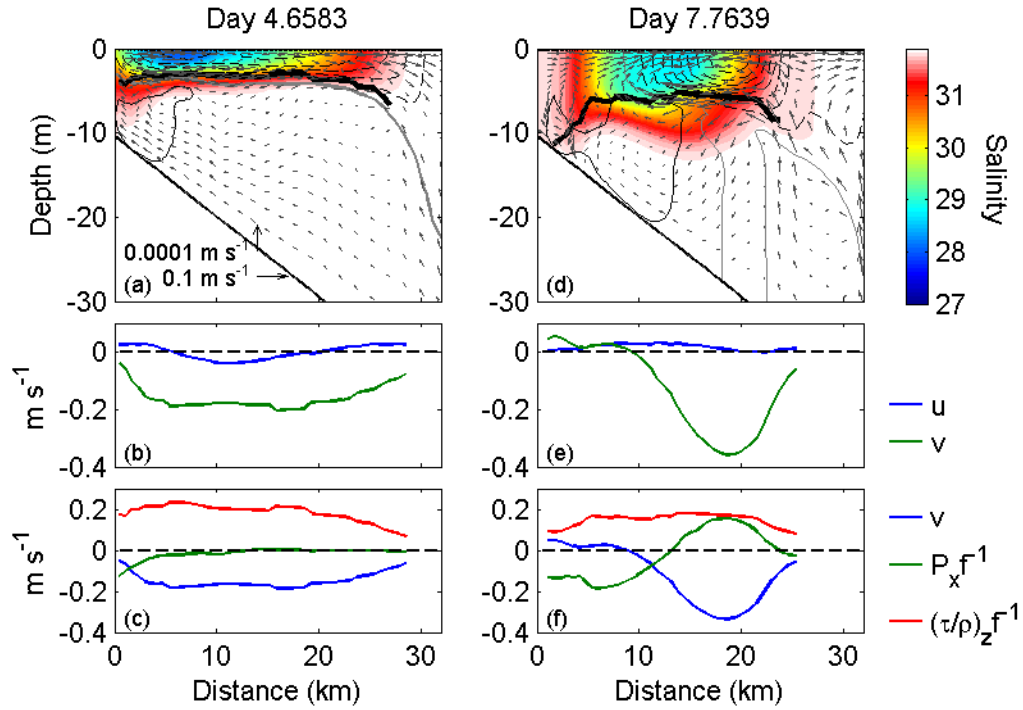


FIG 3.5. Plume velocity, salinity, and momentum for Run 8 at a cross-shore transect 35 km downstream of the outflow. Left panels (a-c) correspond to the onset of the offshore wind stress, while the right panels (d-f) correspond to 3 days after the onset of the wind stress. For panels (a) and (d) color signifies salinity, alongshore velocity is contoured at  $0.05 \text{ m s}^{-1}$  intervals with dashed contours representing downstream velocity and solid, thin black contours representing upstream velocity. The zero isotach is contoured with the thick gray line. Thick black line signifies the plume depth based on where the cross-shore stress goes below 10% of the surface value. Averaged velocity (b & e) and momentum (c & f) are vertically averaged between the surface and the plume depth signified by the black line in (a,d). The vertically averaged momentum terms are normalized by the coriolis parameter ( $\sim 1 \cdot 10^{-4} \text{ s}^{-1}$ ) to yield units of  $\text{m s}^{-1}$ .

During this time period, the plume depth averaged alongshore velocity structure transitions from a state of weak horizontal shear to one with a strong horizontal shear that consists of a strong downstream jet (Fig 3.5, 3.6). This change in velocity structure over the first few inertial periods is in response to the evolution of the pressure gradients during the time period. Panels (c) and (f) in figure 3.5 and 3.6 show the cross-shore momentum terms (normalized by  $f$ ) at the onset of wind forcing and after the spin-up period. At the onset of wind forcing the balance is an Ekman balance between the stress and coriolis terms. Over a few inertial periods the pressure gradient responds to the wind forcing and the offshore movement of the low salinity core of the plume yielding a structure that works in concert with the stress term on the offshore side of the plume while working in opposition on inshore side. This interaction between the cross-shore wind-driven stress and pressure gradient terms drive the asymmetric downstream velocity structure observed in the plume. Advective terms, while important in the near field, are negligible in the far field.

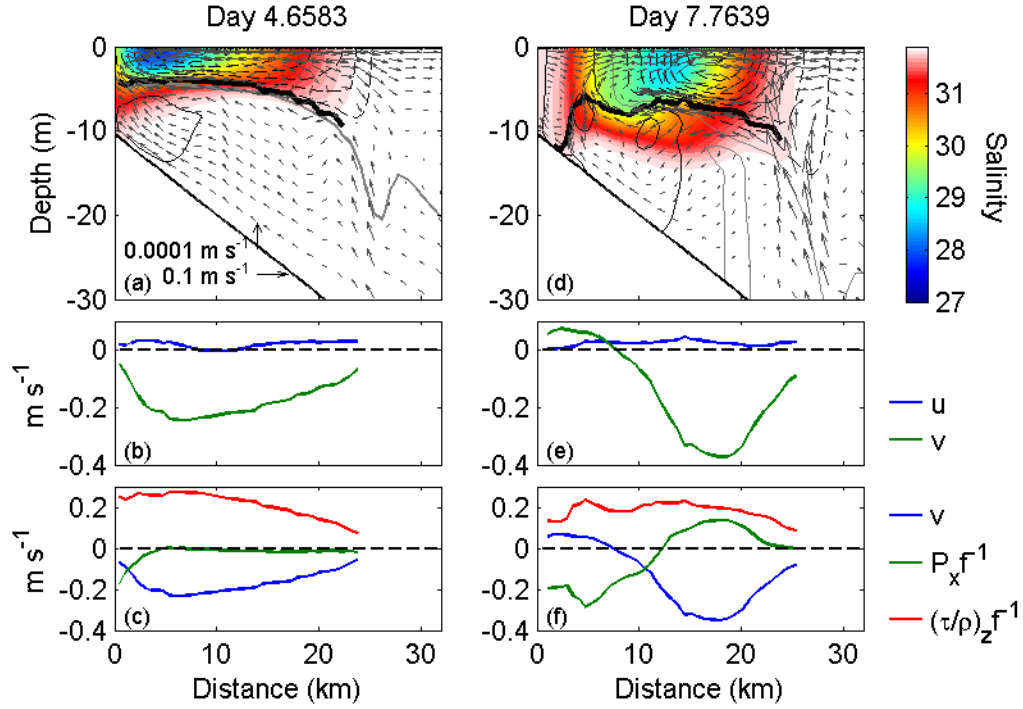


FIG 3.6. Same as Figure 5, except for Run 20.

### 3.4.2. Velocity structure

The cross-shore structure of the alongshore velocity is balanced by the cross-shore pressure gradient, wind stress and coriolis which drives an asymmetric velocity structure. This is shown through the plume depth averaged (Fig 3.5, 3.6), and also from depth dependent quantities (Fig 3.7, middle and bottom panels). The cross plume velocities are offshore near the surface and onshore at depth, with the circulation being weak on the inshore side of plume and rather vigorous on the offshore side.

Vertical profiles of the horizontal velocities are plotted in Figure 3.7 (panels b-d) for three locations in the plume: the midpoint between the inshore edge and the salinity minimum (panel b), the salinity minimum (panel c), and the midpoint between the

salinity minimum and the offshore edge of the plume (panel d). The observed velocity structure can best be described as an Ekman layer for a free surface that is altered by depth dependent pressure gradients (Ekman 1905). The theoretical depth dependent Ekman velocities are plotted alongside the observed velocities at the salinity minimum in panel c. Here we assumed a constant eddy viscosity of  $1.3 \times 10^{-3}$ , which is an average eddy viscosity within the plume from the numerical model, and no pressure gradient for the theoretical velocities. The depth dependent Ekman velocities capture the general structure of the horizontal velocities. Discrepancies can be due to depth dependent stratification, eddy viscosity, and pressure gradients; all of which the Ekman formulation does not account for. On the inshore side the opposing pressure gradient and wind stress lead to weak velocities in both the alongshore and cross-shore direction. In contrast on the offshore side both wind stress and baroclinicity work in concert to generate strong currents and vertical shears. The strong wind driven velocity shear in the alongshore direction on the offshore side of the plume helps drive the strong cross plume circulation. The Ekman response on the offshore side rotates the currents from the offshore direction at the surface to the onshore direction at the base of the plume, and consistent with this; the alongshore momentum balance here is mainly between the coriolis acceleration and the vertical stress divergence.

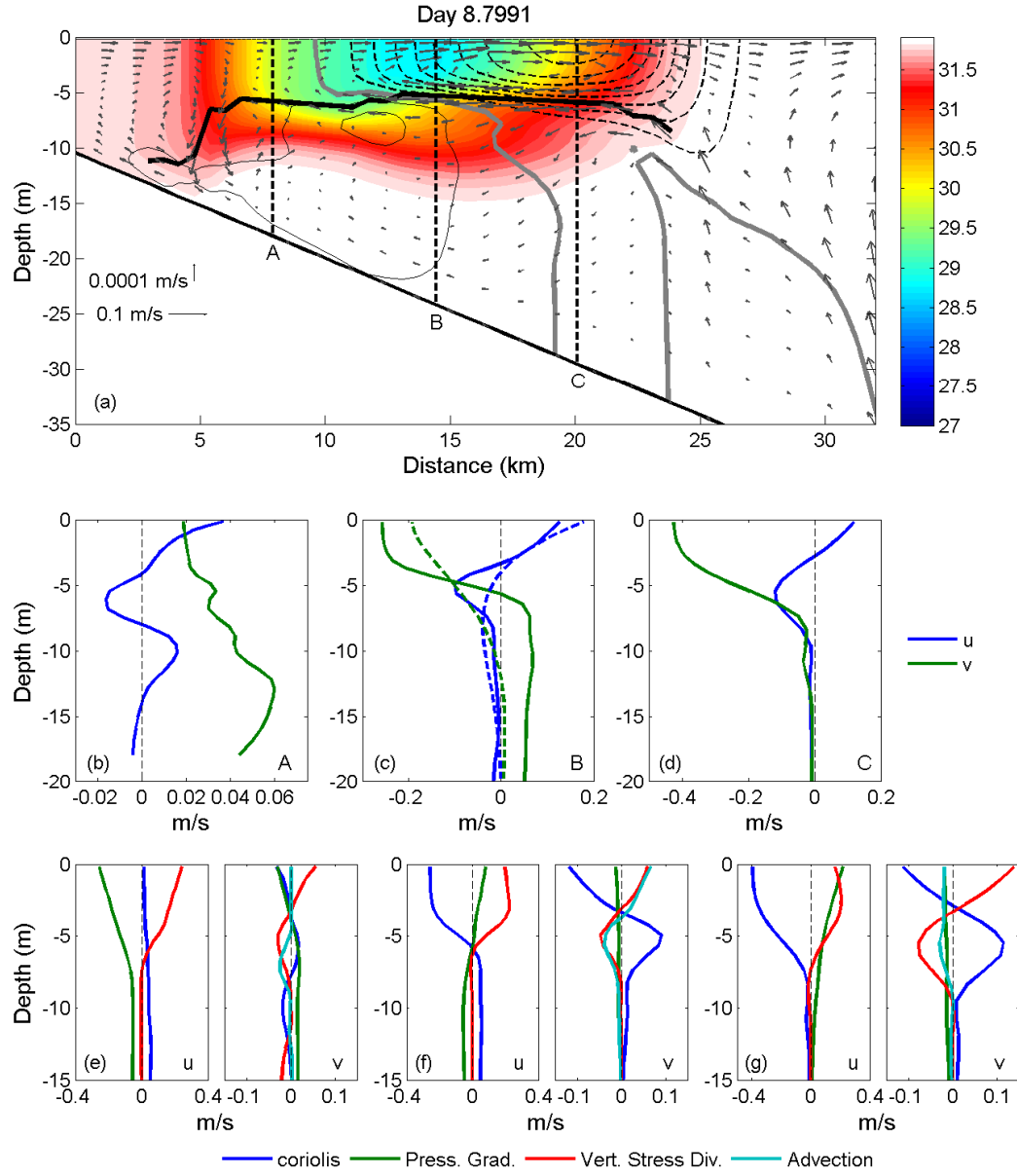


FIG 3.7. (a) Plume velocity and salinity for Run 8. Color signifies salinity, alongshore velocity is contoured at  $0.05 \text{ m s}^{-1}$  intervals with dashed contours representing downstream velocity and solid, thin black contours representing upstream velocity. The zero isotach is contoured with the thick gray line. Thick black line signifies the plume depth based on where the cross-shore stress goes below 10% of the surface value. Vertical dashed lines denote locations of profiles plotted in panels b-g. (b-d) Along and cross-shore velocity profiles. Colored dashed line in (c) is the theoretical Ekman velocity profile. (e-g) Cross-shore (u) and alongshore (v) momentum terms.

### 3.4.3. *Winds strength influence*

The general plume response to the offshore winds described above only applies to simulations where the cross-shore wind stress is the dominant forcing mechanism; for weaker wind stresses buoyancy forcing can be dominant. During these weaker wind simulations the wind is not strong enough to significantly alter the initial bulge recirculation region near the mouth of the outflow and a strong offshore jet seen in wind dominant simulations does not develop. Based on these observations, we define a wind strength index based on the ratio of the downstream Ekman velocity and the observed velocity in the plume after the onset of the wind stress,

$$W_{SI} = \frac{v_e}{v_p} \quad (3.11).$$

Here,  $v_e$  is the plume averaged Ekman velocity and  $v_p$  is the observed plume averaged velocity in the plume. This index is the same as the non-dimensional wind stress term used in Garvine's (1995) dynamical plume scaling.

In the case when  $W_{SI}$  is less than 1, the downstream velocity is larger than the downstream Ekman velocity showing that the buoyancy forcing is a dominant term. When  $W_{SI}$  is greater than 1, the wind stress is the dominant forcing mechanism and the plume averaged buoyancy driven flow is negligible. In many of our simulations  $W_{SI}$  is greater than unity due to upstream barotropic flows driven by the sea level set down near the coast, decreasing the observed plume averaged velocities.

TABLE 3.1. Summary of model runs with varying river discharge, wind stress, estuary width, and the resultant wind strength index ( $W_{SI}$ ). Runs in bold signify a  $W_{SI}$  greater than 1.

<i>Model Run #</i>	<i>Discharge (m<sup>3</sup>/s)</i>	<i>Wind stress (N/m<sup>2</sup>)</i>	<i>Estuary Width (km)</i>	<i><math>W_{SI}</math></i>
1	500	0.025	1	0.86
2	500	0.05	1	0.93
<b>3</b>	<b>500</b>	<b>0.075</b>	<b>1</b>	<b>1.11</b>
<b>4</b>	<b>500</b>	<b>0.1</b>	<b>1</b>	<b>1.14</b>
<b>5</b>	<b>500</b>	<b>0.125</b>	<b>1</b>	<b>1.22</b>
<b>6</b>	<b>500</b>	<b>0.15</b>	<b>1</b>	<b>1.3</b>
7	1000	0.05	1	0.89
<b>8</b>	<b>1000</b>	<b>0.1</b>	<b>1</b>	<b>1.08</b>
<b>9</b>	<b>1000</b>	<b>0.15</b>	<b>1</b>	<b>1.2</b>
10	1500	0.05	1	0.85
<b>11</b>	<b>1500</b>	<b>0.1</b>	<b>1</b>	<b>1.08</b>
<b>12</b>	<b>1500</b>	<b>0.15</b>	<b>1</b>	<b>1.15</b>
<b>13</b>	<b>300</b>	<b>0.075</b>	<b>5</b>	<b>1.03</b>
<b>14</b>	<b>300</b>	<b>0.125</b>	<b>5</b>	<b>1.52</b>
15	500	0.05	5	0.78
<b>16</b>	<b>500</b>	<b>0.1</b>	<b>5</b>	<b>1.11</b>
<b>17</b>	<b>500</b>	<b>0.15</b>	<b>5</b>	<b>1.15</b>
18	1000	0.05	5	0.85
<b>19</b>	<b>1000</b>	<b>0.1</b>	<b>5</b>	<b>1.07</b>
<b>20</b>	<b>1000</b>	<b>0.15</b>	<b>5</b>	<b>1.28</b>

$W_{SI}$  is listed for each of the model runs in Table 3.1. For this set of simulations  $W_{SI}$  is less than one for wind stresses equal to or less than  $0.05 \text{ N/m}^2$ . We choose to not include these runs in the following parameterizations on the plume averaged velocity, density, width and offshore position due to the theories being based on a wind dominated plume.

#### 3.4.4. *Plume averaged parameters*

Plume averaged depth, velocity, and density are estimated using (3.2), (3.3), and (3.8) respectively using only the initial plume averaged depth, density, and wind stress. Here, the critical Richardson number ( $Ri_c$ ) is considered to be 1.0. These theoretical estimates are compared to the plume averaged parameters from the model at a cross-shore transect located approximately 35km downstream of the mouth of the estuary at Day 7.76, approximately 3 days after the onset of wind forcing (Fig 3.8). In general, there is a good agreement between the theoretical depth and the plume depth from the model simulations; however, the theory does tend to slightly over-predict the plume depth, especially for weak wind cases (Fig 3.8a).

The theoretical velocity agrees with the model results for strong wind simulations (Fig 3.8b). The theory under-predicts the plume average velocity for weak wind runs and low discharge due to the cross-shore pressure gradient not being symmetrical. In these runs the center of the plume remains close to the coast, which reduces the inshore area of the plume with a shoreward directed pressure gradients and reduced (or even reversed) alongshore velocity. Consequently this results in a stronger plume averaged downstream velocity.



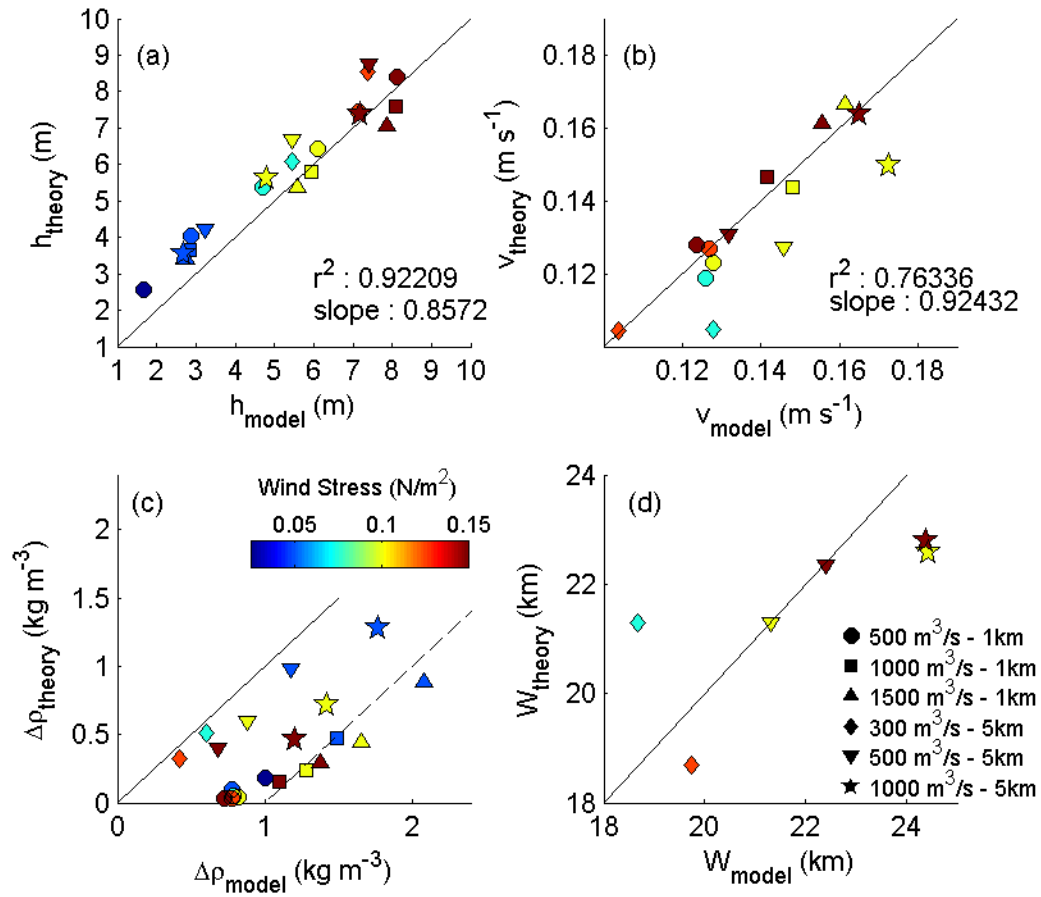


FIG 3.8. Comparison of model output and theory for plume depth (a), velocity (b), density (c), and width(d) 4 days after the onset of wind. Shapes indicate the river discharge and estuary width while the color of the marker represents the magnitude of the wind stress. The solid black line is the 1:1 line. The dashed line in (c) denotes a 1 kg m<sup>-3</sup> offset.

As previously stated, the theory greatly over-predicts the density for the narrow outflow runs, while there is a better agreement with the wide outflow runs (Fig 3.8c). The best results are for runs 13 and 14 which are both low discharge and wide outflow simulations. These discrepancies are due to the varying validity of the key assumption

that freshwater is conserved in the cross-shore transect of the plume. Remember, the simulations are initialized with what amounts to a 6 day old plume at the onset of the wind stress, and the size of the recirculating bulge region that develops during this time is dependent on the river outflow and the estuary width. Hence, the theoretical density estimates from the large discharge, narrow outflow simulations (runs 10-12) have the greatest offset and the theoretical density estimates for runs 13 and 14 fall the closest to actual plume density values. Despite these errors for the narrow outflows, we can still utilize the estimates of the plume depth, velocity, and density to estimate the plume width for the wide outflow simulations as described in the next section.

#### 3.4.5. *Plume width*

After several days of wind forcing, the freshwater transport in the plume approaches equilibrium with the freshwater discharge from the estuary (Fig 3.8d). Knowing this, we can take a formulation for the freshwater transport in the plume, and substitute the freshwater transport with the freshwater discharge from the estuary,

$$Q_r = \frac{\Delta s}{s_o} v_p h_p W_p \quad (3.12).$$

Here,  $v_p$ ,  $h_p$ , and  $\Delta s$  are calculated from equations (3.2), (3.3), and (3.8) respectively.

Solving for  $W_p$  in (3.12) yields

$$W_p = \frac{Q_r s_o}{v_p h_p \Delta s} \quad (3.13).$$

The results of (3.13) are computed only for wide outflow runs with  $W_{SI} > 1$ . The results of which are plotted with the plume width measured in the model in Figure 3.8d. Due to instabilities propagating downstream in the plume, the plume widths (as calculated using

(3.13) and from the model) are averaged over a 4 day period. Equation (3.13) yields a good agreement with the observed plume widths for runs that are wind dominated. The notable exception is run 13 (120 m<sup>3</sup>/s discharge, 5km width, 0.1 N/m<sup>2</sup> wind) where the theory greatly over predicts the plume width.  $W_{SI}$  for run 13 is 1.03, so it is near the wind forced limit, and it can be seen in Figure 3.8b that it also has a large offset when comparing the theoretical and model velocities, which leads to an increase in the theoretical plume width.

#### 3.4.6. Offshore position

We now have reliable formulations for the plume averaged depth and velocity for all wind dominated runs, and salinity and width estimates for low discharge and wide outflow runs. We now will describe the controls of the offshore position of the plume core. The initial offshore transport of the plume can be divided into two processes: the spin-up of the Ekman response and the advection from the estuarine outflow. The steady state offshore position of the plume core is simply balance between the offshore advection due to the estuarine outflow and the downstream advection of the plume due to the wind driven Ekman transport. We parameterize the cross and along shore advection processes with two Froude numbers,

$$F_{estuary} = \left( \frac{u}{c} \right)_{estuary}; \quad F_{plume} = \left( \frac{v}{c} \right)_{plume} \quad (3.14).$$

Here  $u$  is the average outflow velocity at the mouth of the outflow,  $v$  is the plume averaged velocity at a downstream transect, and  $c$  is the internal wave speed ( $c = \sqrt{g'h}$ ) at the location denoted by the subscript. The ratio of the two Froude numbers,

$F_{plume} / F_{estuary}$ , can be thought of as a ratio of two non-dimensional velocities. With that

in mind, the larger the ratio, the closer the plume core is to the shore and the smaller the ratio the further offshore the plume core will be.

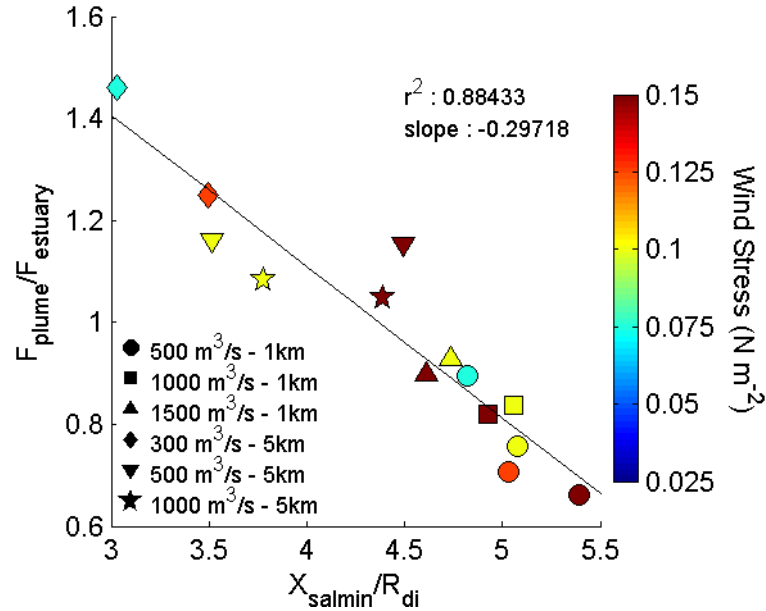


FIG 3.9. Ratio of plume and estuary Froude numbers and the normalized offshore position of the plume core. Shapes indicate the river discharge and estuary width while the color of the marker represents the magnitude of the wind stress. Black line is the best fit line.

The ratio is plotted with the normalized offshore distance of the plume core in figure 3.9, where the plume core is defined as the location of the minimum surface salinity at the transect and this position is normalized by the internal deformation radius ( $R_{di} = c/f$ ). There is a good agreement between the Froude number ratio and the normalized offshore plume core position. If the normalized plume velocity is larger than the normalized estuarine velocity, then the plume will be close to the shore due to the

plume being advected downstream faster than it is being advected offshore by the outflow velocity. The opposite is true if the Froude number ratio is less than 1.

### 3.5. Plume Mixing

Understanding mixing is vital to understanding the response of a buoyant plume to a wind stress. To achieve this understanding we follow Hetland (2005) and perform an analysis of the vertical salt fluxes throughout transects of the plume, then classify the vertical salt flux at the base of the plume according to surface salinity, and finally track freshwater transports between salinity classifications.

#### 3.5.1. *Cartesian coordinate analysis*

The vertical salt flux is calculated by multiplying the hourly salt eddy diffusivity and vertical salinity gradient from the numerical model and then averaging the product over two M2 tidal cycles. Cross-shore transects of vertical salt fluxes are plotted at two transects in Figure 3.10 for three different time periods. Transect 1 is at the mouth of the estuary and transect 2 is approximately 35 km downstream of the outflow.

The highest values of vertical salt flux are found at transect 1 for run 8 (1 km wide estuary, 1000 m<sup>3</sup>/s discharge, 0.1 N/m<sup>2</sup> wind stress) near the outflow region where there is high velocity shear that drives the mixing. The high vertical salt flux values near the outflow region increase after the onset of the wind stress (day 4 and after) due to an increase in the velocity shear. This increase in mixing near the outflow after the onset of the wind stress coincides with an increase in the surface layer salinity. Before the onset of the wind stress at transect 2, the plume is simply in a geostrophic balance which

exhibits less vertical mixing in the absence of a surface stress and the vertical velocity shears associated with the estuarine outflow. After the wind stress turns on, the structure of the vertical salt flux mirrors that of the alongshore velocity field. At day 4.65 (onset of wind) the downstream velocity is broadly distributed over the width of the plume from the initial Ekman response and the vertical salt flux mirrors that vertical velocity shear with the highest values distributed widely over the inner portion of the plume transect. After the cross-shore pressure gradients develop and the downstream offshore jet develops, the high mixing rates form on the offshore side of the plume in the vicinity of the high velocity shear zone described previously.

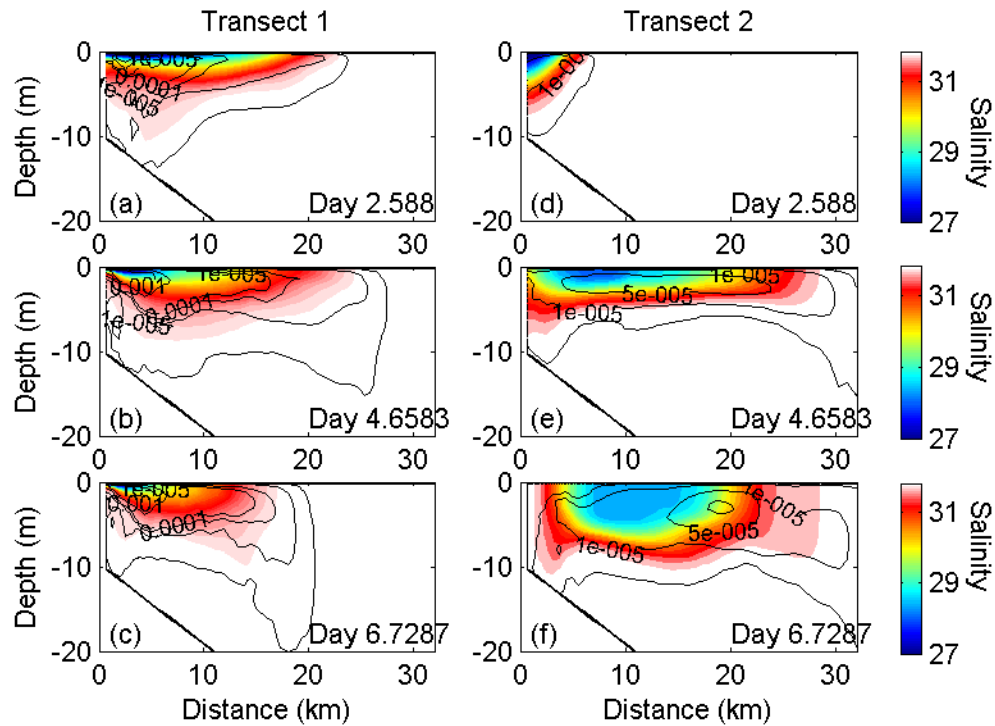


FIG 3.10. Vertical salt flux (black contours) and salinity (color map) for Run 8 at 2 cross-shore transects, near the mouth (left panels) and 35 km downstream (right panels) for three time periods: 2 days before the

onset of wind (top panels), the onset of wind stress (middle panels), and 2 days after the onset of wind (bottom panels).

Even though there are relatively high vertical salt flux values on the offshore side compared to the inshore side of the plume at a given cross-shore transect, the plume remains remarkably stable in its salinity and velocity structure over time. In examining the salt equation, the importance of the advective terms becomes clear in maintaining the steady salinity field. The first order balance is between the turbulent vertical mixing  $(\partial/\partial z (K_s \partial s/\partial z))$  and the cross-shore advection of salt  $(u \partial s/\partial x)$ , Fig 3.11). The turbulent mixing is focused on the offshore side of the plume in the high vertical shear region. Here, the vertical mixing that is acting to de-stratify the plume is roughly balanced by the straining of the salinity field by the cross-shore velocity field that acts to stratify the water column. On the inshore side of the plume there is weak vertical velocity shear and the cross-shore circulation acts to make the plume's isopycnals more vertical, reducing the stratification in the plume and inhibiting vertical mixing of salt in this region of the plume. The residual of  $u \partial s/\partial x$  and  $\partial/\partial z (K_s \partial s/\partial z)$  is dominated by the alongshore advection of salt  $(v \partial s/\partial y)$ . While  $v \partial s/\partial y$  may appear small, it is vital to maintaining the steady nature of the plume by advecting freshwater from upstream into the transect, allowing  $u \partial s/\partial x$  to stratify the offshore portion of the plume, and advecting the saltier mixed water downstream. Once at the steady state, this balance allows the cross-shore salinity structure to constantly maintain itself.

Here we examine the alongshore structure of the salt equation to describe the different dynamical regions of the plume. We start by using the salt equation of the form

$$\frac{\partial s}{\partial t} = -u \frac{\partial s}{\partial x} - v \frac{\partial s}{\partial y} - w \frac{\partial s}{\partial z} + \frac{\partial}{\partial z} \left( K_s \frac{\partial s}{\partial z} \right) \quad (3.15),$$

where  $x$ ,  $y$ , and  $z$  are the cross-shore, alongshore, and vertical coordinates respectively and  $K_s$  is the salinity diffusivity. The terms in (3.15) are then vertically integrated between the surface and the plume depth as a function of  $z$  and then cross-sectionally averaged. This yields the average turbulent vertical salt flux, advective salt fluxes, and the resultant integral of the rate of change of salinity within the plume at a given alongshore location. The result of this calculation is shown in figure 3.12d,e. Over the alongshore extent of the plume the main balance is between the vertical turbulent salt flux and the total advective salt flux. In essence, the turbulent mixing is working to de-stratify the plume while the total advective term is bringing in fresher water from the river discharge to re-stratify the interior of the plume.

When the advective term is separated into its directional components, different plume mixing regions can be seen. At the location of the outflow, the vertical and alongshore terms are acting to bring salt into the plume, while the cross-shore term is working to freshen the plume. The alongshore term acts to increase the salt content due to the downstream Ekman flow advecting saltier water from upstream of the outflow into the fresher plume. In the outflow region there is a net upward vertical velocity in response to the plume thinning and spreading. This can also be described of as the ‘lift-off’ zone (Hetland and MacDonald 2008, MacDonald et al. 2007). It is this region we classify as the near-field region. Here, the cross-shore advection of freshwater from the



river outflow dominates the total advective term. The leading order terms in the near-field region are the total advective term which is balanced by the turbulent vertical salt flux. The time dependent salt term does not contribute to the balance in this region.

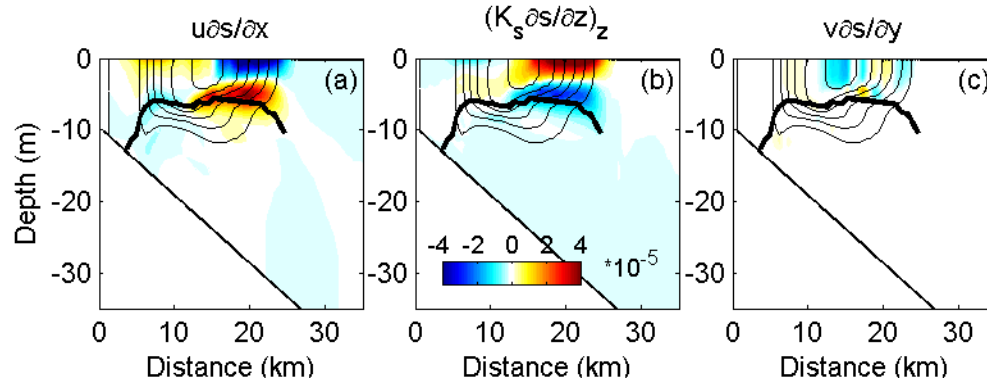


FIG 3.11. Cross-shore advective salt term (a), vertical divergence of the turbulent vertical salt flux (b), and alongshore advective salt term (c). Cross-shore transect is located approximately 35 km downstream of the outflow at day 7.76. Thick black line signifies the plume depth based on where the cross-shore stress goes below 10% of the surface value. Salinity is contoured in black at 0.5 intervals.

From the location where plume spreading and thinning diminishes (vertical advection of salt approaches zero) and the cross-shore advective term approaches zero is the mid-field region. Here, the plume is no longer thinning, but the plume is still turning in response to coriolis and the Ekman driven flows. The magnitude of the cross-shore salt flux decreases as distance from the near-field region increases due to the plume becoming more aligned with the alongshore direction. The alongshore advective term also decreases in the mid-field region in response to the alongshore salinity gradient transitioning from a negative regime (saltier upstream) to a positive one (fresher upstream). In the process, the alongshore advective term becomes a dominant term near

the downstream limits of the mid-field region. The total advective term is once again mainly balanced by the turbulent vertical salt flux; however, the salt rate does play a role and the plume is slightly saltening in this region.

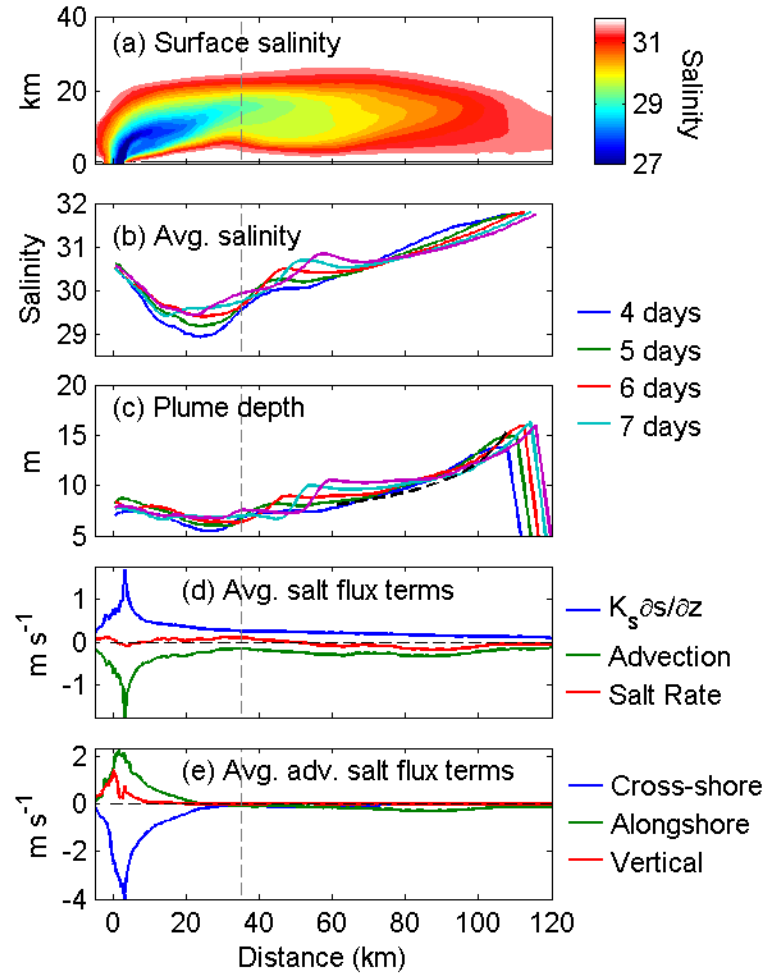


FIG 3.12. Surface salinity for Run 20 at 4 days after the onset of wind forcing (a). Cross-sectionally averaged salinity (b) and plume depth (c) for a four day time period from 4-7 days after the onset of wind. Theoretical plume depth based on a constant salinity gradient is plotted in (c) with a black dashed line. Cross-sectionally averaged salt flux terms with the total advection term (d) and the cross-sectionally averaged advective components (e). Vertical gray dashed line denotes the approximate location of the mid-field/far-field plume boundary.

In the far-field the vertical and cross-shore advective salt fluxes are now negligible, and the turbulent vertical salt flux is balanced mainly by the alongshore advective flux of freshwater downstream. In this region of the plume, the alongshore salinity gradient is constant in the alongshore direction (once the instabilities propagating downstream are averaged over). The salinity value near the mid/far-field boundary is constant in time and the salinity value at the leading edge of the plume is set to 31.8 by the definition we set for defining the plume. These factors plus the continually downstream propagation of the plume (the far-field is constantly growing) lead the plume to become fresher in an Eulerian reference frame. It should be noted that the plume structure is dictated by the wind induced velocity shear mixing processes. If a typical constant salinity gradient in the far-field plume is assumed and used in the critical Richardson number based estimate of the plume depth, it is found that both the observed plume depth and the theoretical depth show the same  $\Delta\rho^{-1/3}$  dependence from (3.2) (Fig 3.12c).

### 3.5.2. *Salinity coordinate analysis*

To look at the both the spatial and temporal variability of mixing in the plume, we examine mean vertical salt fluxes classified by salinity. Using Hetland (2005) as guidance, the vertical salt flux is calculated at the base of the plume over the entire horizontal domain of the plume, excluding the estuary channel. Here, the base of the plume is defined as the depth where  $\Delta\rho \leq \frac{1}{2}(\rho_o - \rho_{surface})$ . The mixing values at the

base of the plume are then separated into salinity classes based on the surface salinity at each location ranging from the minimum salinity to the maximum salinity in the model domain, 32, at 0.25 intervals. The results of this analysis are plotted in Figure 3.13.

Since low salinity values are located near the outflow and higher values are located near the periphery of the plume, we have a general idea of the spatial variability in the mixing at the base of the plume. Generally, the vertical mixing rates in the plume increase when the wind stress is turned on, with the greatest increases seen at the lower salinity classes near the mouth of the outflow. As time progresses, the vertical salt fluxes in the higher salinity classes (far-field plume) decrease to approach the mixing values prior to the wind stress.

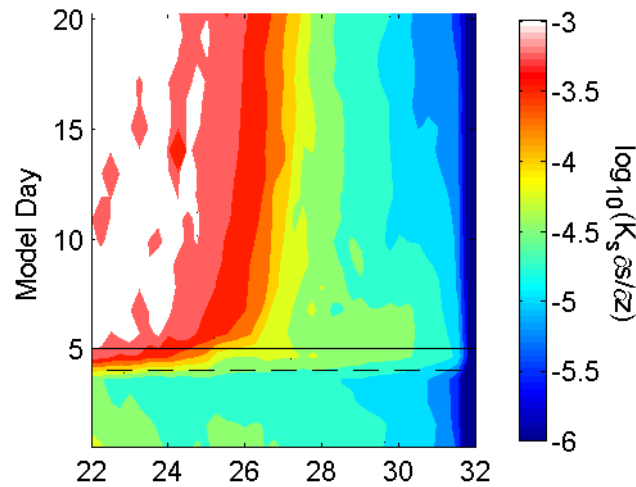


FIG 3.13. Vertical salt flux ( $\text{m s}^{-1}$ ) at the base of the plume classified by salinity for Run 8. Horizontal dashed line at day 4 and solid line at day 5 note were the wind stress turns on and reaches it maximum value respectively.

To better explain the temporal and salinity space structure of the vertical salt flux, it is helpful to examine the transport of freshwater in the plume in salinity space. The volume of freshwater in an individual salinity class is defined as

$$V_f = \int_{s_c(i-1) \leq s < s_c(i)} \frac{s_o - s}{s_o} dV \quad (3.16)$$

where  $s_o$  is the background salinity of 32,  $s$  is the salinity of the grid cell which must fall between salinity class values  $s_c(i)$  and  $s_c(i-1)$ , and  $V$  is the volume of the grid cell. Prior to the onset of the wind stress the freshwater is broadly distributed over a range of salinity classes. After the onset of wind the freshwater in the lower salinity classes (which represent the recirculating bulge region) is transported to higher salinity classes (Fig 3.14a). This is more obvious when taking the time derivative of  $V_f$ . Here it is clearly seen that there a loss of freshwater at lower salinity classes and gain at higher salinity classes once the wind turns on (Fig 3.14b). It is important to note that there is a clear delineation between salinity classes losing and gaining freshwater. When we take that mixing interface where  $dV_f/dt=0$  and superimpose it on top of the plot of  $V_f$ , we can see that it separates regions in salinity space that are steady in time (left of the interface) and still being mixed (right of the interface). In salinity space the contours for freshwater volume are vertical in the steady region and horizontal in the unsteady region. This is also true for plume parameters such as plume depth and isohaline surface area (not shown).

The steadiness of the plume parameters can be described by once again manipulating the bulk critical Richardson number formulation in (3.1). As is done in by Hetland (2005), instead of solving for  $h_p$ , (3.1) can be solved for a critical salinity,

$$s_{crit} = 32 - \left( \frac{4Ri_c \rho_a |\Delta u|^2}{gh_p} \right) \beta^{-1} \quad (3.17)$$

where  $\beta = 0.78 \text{ kg}^{-1}$ . The critical salinity is calculated in salinity space by finding the mean depth of the plume at each location in each salinity class based on the mean plume salinity at that location. The salinity space plume depth is then input into (3.17) along with the Ekman velocity and the critical Richardson number ( $Ri_c = 1$ ). This yields a critical mixing salinity for each salinity class and time. We develop a critical mixing parameter by taking the ratio of the critical salinity and the salinity class value to yield

$$s_{mix} = \frac{s_{crit}}{s_{class}} \quad (3.18).$$

When  $s_{mix} < 1$ , the plume will mix because the critical salinity is less than the plume salinity, allowing the wind induced velocity shear to mix the plume. When  $s_{mix} > 1$ , the plume is considered stable because the plume salinity is less than the critical salinity; the velocity shear cannot overcome the buoyancy forcing, preventing the freshwater from being transported to a higher salinity class.

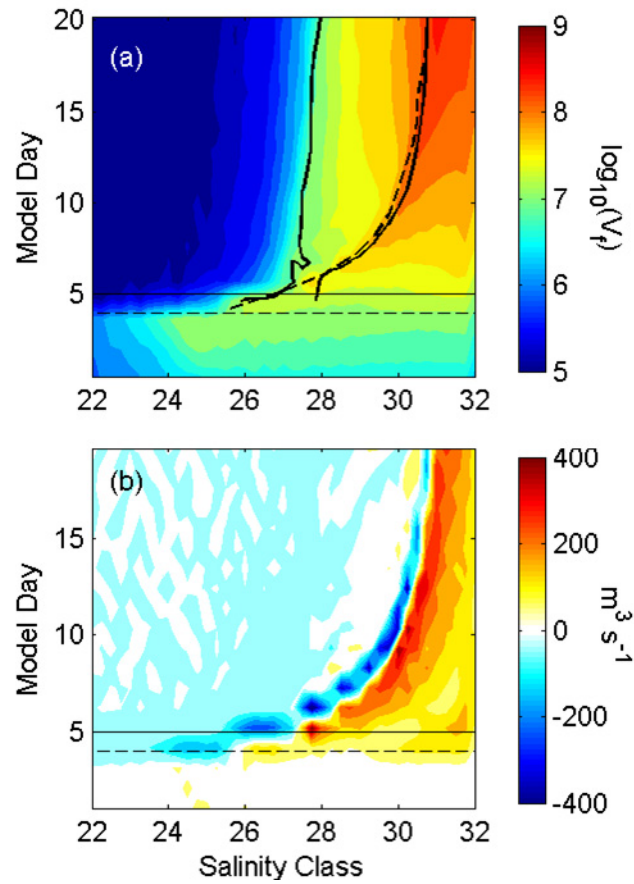


FIG 3.14. Freshwater volume (a), and  $dV_f/dt$  (b) for Run 8. Solid and dashed black contours in (a) are the  $s_{\text{mix}} = 1.02$  contour and the  $dV_f/dt = 0$  contour respectively. Horizontal dashed line at day 4 and solid line at day 5 note were the wind stress turns on and reaches it maximum value respectively.

The  $s_{\text{mix}} = 1.02$  contour is plotted with the freshwater volume and the  $dV_f/dt = 0$  contour in Figure 3.14a. The  $s_{\text{mix}}$  contour closing follows the  $dV_f/dt$  contour, which separates vertical contours of  $V_f$  (steady in time) and horizontal contours (mixing). This exercise can also be done by calculating a Richardson number in salinity space and contouring a critical value. This approach yields similar results as the critical salinity calculation shown here. In the stable region the wind has mixed the

plume enough so that the plume salinity is less than the critical salinity, which now inhibits the mixing. The stable regions in salinity space can be loosely defined as the near and mid-field plume regions defined and the mixing region in salinity space can be described as the far-field region. Mainly, the mixing region in salinity lies near the downstream edge on the plume and the periphery. The two classifications cannot be directly compared since salinity classes can reside in different dynamical regions; however, the salinity class classification does provide a general overview of the processes occurring in Cartesian space.

### 3.6. Summary

This study has utilized idealized model simulations to describe the response of an offshore wind on a buoyant plume system. The tools developed here to describe and predict the structure of a plume should be applicable to a plume subjected to an offshore wind stress in nature. The theories should hold for any plume and offshore wind stress that has a wind strength index greater than 1. However, we do acknowledge the difficulties with estimating the plume width since the assumption the freshwater is conserved in a cross-shore transect is not always the case, due to a continual supply of fresh water from the estuarine discharge.

The idea of the position of the plume core (under a cross-shore wind stress) being related to the outflow velocity of the estuary is in line with the findings of Horner-Devine et al. (2006). They found that for an unforced plume (no wind stress) that the offshore position of the core of the recirculating bulge region had a dependence on the outflow Froude and Rossby numbers. Their reasoning was similar in that the offshore position



was related to the offshore advection from the outflow and the tendency of the flow to turn right due to rotation. In this study we have added another level of complexity with the addition of the cross-shore wind stress, but the dependence on the outflow velocity remains fundamentally the same.

The dependence of a plume's downstream structure and position on outflow conditions when subjected to an offshore wind stress is in stark contrast to how a plume responds to an alongshore upwelling wind stress. In the alongshore wind response the plume can be thought of as strictly two dimensional (Lentz 2004, Moffat and Lentz 2012). We have shown here that a two dimensional approach would not capture the entire response of the plume to the offshore wind stress since the alongshore advection of momentum and salt within the plume are first order parameters in the momentum and salt balances.

It has been found that the steady salinity structure within a cross-shore transect of the plume is maintained by a balance between the turbulent vertical mixing and the cross-shore advection of salt. The residual is dominated by the alongshore advective term which replenishes the plume transect with freshwater, maintaining the salinity structure in time. By examining the alongshore structure of the cross-sectionally averaged salt flux terms, the plume can be segregated into three distinct regions: near-field, mid-field, and far-field plume. The near-field region is located at the outflow of the estuary into the ocean and is characterized by large cross-shore salt fluxes along with high turbulent vertical salt fluxes. The mid-field is a transition zone where the plume is turning toward the alongshore direction and thus the cross-shore salt flux diminishes in importance over

the region. Once the cross-shore salt fluxes approach zero, the plume reaches the far-field. Here, the turbulent vertical salt fluxes are balanced by the alongshore advection of freshwater.

Mixing in the plume was also examined by tracking the volume of freshwater using a salinity coordinate system. A mixing interface in salinity space develops where  $dV_f/dt = 0$  and separates regions of the plume that are steady and unsteady in time. The  $dV_f/dt = 0$  contour also agrees with a critical mixing salinity which shows whether a salinity class's buoyancy will inhibit mixing (steady) or lead to an increase in plume depth in time (unsteady).

The fact that the plume reaches a relatively steady state can in part be attributed to the dependence on the outflow conditions or an upstream control of the downstream conditions. The steadiness of the plume is also vastly different than the response to a plume to upwelling winds which continuously mix and deepen a plume while transporting it across the shelf. For example, it is shown here that for an offshore wind stress of  $0.1 \text{ N/m}^2$ , the plume is rapidly advected offshore 15-20 km, but then stays stationary at that location for the duration of the wind event. In contrast, an upwelling wind of the same magnitude and initial plume structure and be transported offshore approximately 40 km in a 3 day period. This difference can have implications for stratification in the inner shelf/near shore region, as well as nutrient transport, productivity, and the fate of pollutants.

## **Chapter 4:**

### **The response of the Hudson River plume to offshore winds**

## Abstract

The effect of offshore winds in the Hudson River plume and the New York Bight are examined using the semi-idealized and realistic numerical simulations using the Regional Ocean Modeling System (ROMS). Semi-idealized simulations are forced with a steady wind varies between eastward (offshore) and southeastward. The offshore position of the far-field plume is directly and indirectly related to the magnitude of the downwelling component of the wind stress, with the plume being furthest offshore during the pure eastward wind and trapped against the coast for the southeastward wind. In the region near the mouth of the outflow, the plume displays a bulge-like circulation for all model runs. The offshore position of the bulge region is correlated to an outflow Froude number. The structure of the velocity field off the Long Island coast is also correlated to plume position, suggesting it plays role in the plume structure. The plume averaged velocity is found to be simply the sum of the Ekman velocity, geostrophic barotropic velocity due to sea level set down, and the ambient shelf circulation. The semi-idealized results are compared to realistic simulations of the Hudson River plume during the 2005/2006 winter season when offshore winds are dominant. Four offshore wind events are described, the results of which compared favorably to the results of the semi-idealized runs. However, it is noted that it takes the plume approximately 6 days to reach a quasi-steady state position, and as the wind forcing for the realistic run falls in the 3-5 day synoptic weather band, the plume never fully reaches its maximum offshore position.

## 4.1. Introduction

Upon entering the coastal ocean, buoyant river discharge typically turns to the right (left) in the northern (southern) hemisphere and forms a buoyant coastal current that flows in the direction of Kelvin wave propagation (Chao and Boicourt, Fong and Geyer 2002, Garvine 1995, Yankovsky and Chapman 1997). If the buoyant water is confined to a relatively thin surface layer, the plume can be highly susceptible to wind induced mixing and transport. Upwelling winds (opposing Kelvin wave propagation) can rapidly transport the plume across the shelf. The plume thickens in response to the wind stress and reaches a critical depth based on a Richardson number criterion (Fong and Geyer 2002, Lentz 2004, Hetland 2005). The plume continues to deepen as it is transported offshore through an Ekman straining process that continually entrains ambient water into plume on the offshore edge (Lentz 2004). Downwelling winds has been found to press the plume against the coast, causing the isopycnals to steepen and increase downstream velocities (Moffat and Lentz 2012). These two responses suggest two basic freshwater transport pathways on a shelf: a downstream propagating coastal current associated with weak or downwelling winds and an offshore pathway associated with upwelling winds.

In the New York Bight (NYB), complicated bathymetric features, like the Hudson Shelf Valley (HSV), and the geometry of the coastline can cause the plume response to wind forcings to diverge from the simple Ekman based theories (Chant et al. 2008, Castelao et al. 2008, Zhang et al. 2009, Jurisa and Chant 2012, Yankovsky et al. 2001). Numerical simulations of the freshwater transport pathways in the NYB during 2005-2006 show three distinct pathways: the New Jersey coast pathway, Long Island

pathways, and a mid-shelf pathway along the southern edge of the Hudson Shelf Valley (HSV) (Zhang et al. 2009). When broken up by season, it was found that the NJ coast pathway dominates during the winter and spring when downwelling winds are more common while the Long Island and mid-shelf pathway dominate during the summer and fall when upwelling winds are typical. As noted by Castelao et al. (2008), the mid-shelf pathway, while driven by upwelling winds, is not a direct result of the cross-shore advection of the plume through an Ekman response. In the case of the mid-shelf pathway, it seems that it remains connected to the outflow region, continually supplying freshwater to the downstream region as is evident from CODAR velocity fields (Castelao et al. 2008). From the results of Zhang et al. (2009), it appears that the position of the mid-shelf pathway is in part controlled by the presence of the Hudson Shelf Valley. Simulations run without the HSV showed a large decrease in the freshwater transport in the mid-shelf region, which is attributed to the HSV altering the barotropic flows in the NYB.

The previously mentioned studies focused on the effect of alongshore winds on the freshwater pathways in the NYB, ignoring the impact of cross-shore winds. However, in the NYB offshore directed winds are a dominant forcing mechanism during the winter (Fig 1). Modeling (Tillburg 2003) and observational studies (Fewings et al. 2008) have described how offshore winds can drive an offshore transport of water in the unstratified inner shelf. An early plume modeling study by Chao (1988) looked at the impact of steady offshore winds and noted that the plume was transported offshore and freshwater transport on the offshore side of the plume was increased with a corresponding reduction in transport on the inshore portion of the plume. Choi and

Wilkin (2007) show a similar structure for the Hudson River plume. Recent idealized modeling efforts by Jurisa and Chant (submitted) have shown that the offshore transport of the plume is driven by offshore momentum of the estuarine outflow and that the plume reaches a relative steady state in terms of position and structure within a few inertial periods of the onset of the steady wind forcing.

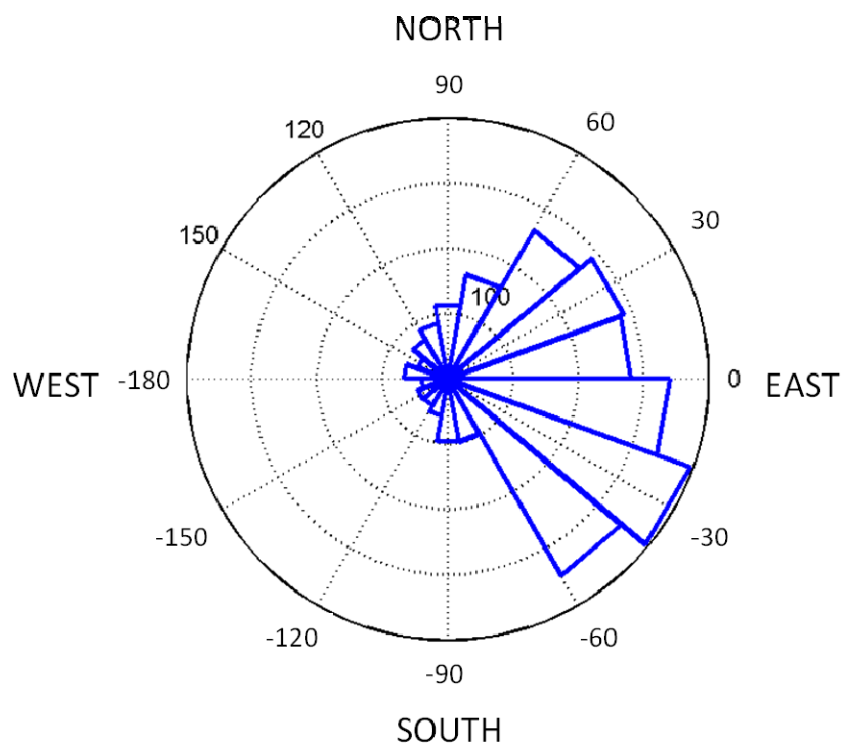


FIG 4.1. Wind rose of the wind forcing during the 2005/2006 winter season. Note the wind direction is reported in the direction the wind blow toward.

Until this time, there has been little done to examine the response of the Hudson River plume to offshore winds under realistic forcing. In a dye mixing study of the Hudson River plume, Houghton et al. (2008) observed an unexpected freshening of the plume during a period of offshore wind forcing. How will the complexities of the NYB affect the response of the Hudson River plume? To tackle this question we will use a two

step approach using the Regional Ocean Modeling System (ROMS). First we will examine the response of the Hudson River plume to steady offshore directed winds. We will then use the results of the semi-idealized simulations to describe the results of a realistic simulation of the 2005-2006 winter season when offshore winds are common (Fig 4.1). The model and NYB will be described in section 4.2 with the semi-realistic and the 2005-2006 winter simulations results described in sections 4.3 and 4.4 respectively. The results will be summarized and discussed in the section 4.5.

## 4.2. Model Description

For this study, we utilize the Region Ocean Modeling System (ROMS, <http://www.myroms.org>). Shchepetkin and McWilliams (2005, 2009a) describe the ROMS computational kernel in detail. Haidvogel et al. (2008), as corrected by Shchepetkin and McWilliams (2009b), give an overview of ROMS features and applications. The model domain covers from eastern Long Island to just south of the mouth of Delaware Bay and out to approximately the 70 m isobaths (Fig 4.2). The horizontal resolution is approximately 1.2 km. The vertical grid consists of 30 layers with a finer resolution near the surface to better capture the surface-trapped buoyant plume structure. At the open boundaries the model utilizes Flather (1976) and Chapman (1985) conditions for the depth-averaged velocity and sea-level respectively. A radiation boundary condition is used for 3-D momentum and tracers. The model uses the k-kl mixing set up from the generic length scale (GLS) mixing scheme. The remotely forced depth-averaged mean alongshelf velocities are included on the open boundaries based on work done by Lentz (2008) on the mean circulation in the Mid-Atlantic Bight.



#### 4.2.1. Semi-idealized model set-up

For the semi-idealized model runs, the Hudson River freshwater discharge is set to a constant to  $800 \text{ m}^3 \text{ s}^{-1}$ , which is the mean discharge during the 2005-2006 winter season that will be examined later. For the semi-idealized set of runs, the discharge for the Delaware River is held to 0. For tidal forcing, simply an M2 tide is forced at the open boundaries. The temperature throughout the domain is set to  $8^\circ\text{C}$ . Atmospheric heat fluxes and evaporation/precipitation are set to 0 as well. The model runs are initialized with a mean salinity structure on the shelf with four days of river discharge. Once the model starts, the wind forcing is held to zero for 3 days when it is then ramped up to its maximum value over a period of a day. After that, the wind stress is constant throughout the remainder of the run.

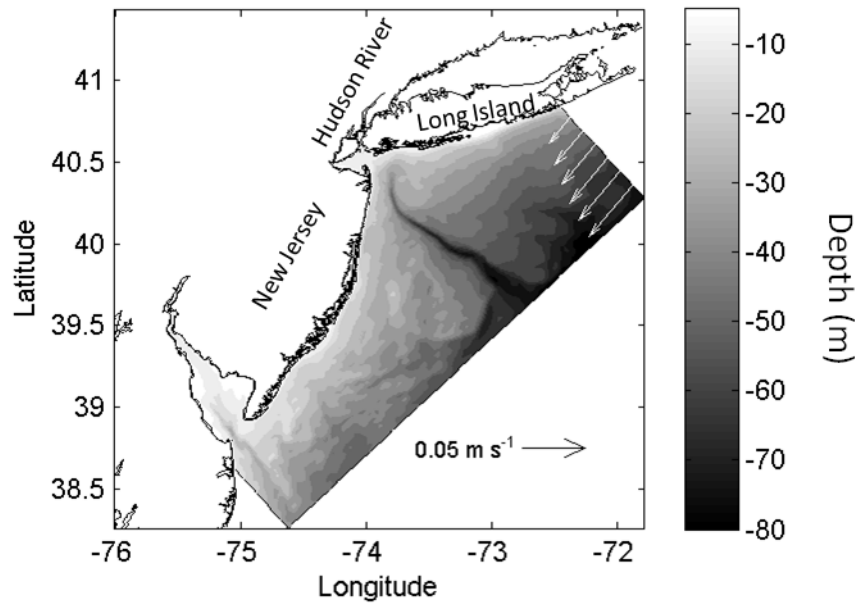


FIG 4.2. LaTTE model domain. Depth contour in grayscale at 5 m intervals. Alongshore ambient circulation imposed at the boundary is plotted as white arrows.

For this model set-up there is a suite of 6 runs with slightly different wind forcing. For all runs the magnitude of the wind stress is equal to  $0.1 \text{ N m}^{-3}$ . What varies is the direction of the wind stress, with model runs consisting of winds directed eastward ( $0^\circ$ ),  $-10^\circ$ ,  $-15^\circ$ ,  $-20^\circ$ ,  $-22.5^\circ$ , and  $-45^\circ$ . All winds directions for here on will be reported using east as  $0^\circ$ , with more southward having a negative angle and more northward directed winds having a positive angle.

#### 4.2.2. *Realistic model set-up*

At the offshore boundaries the realistic model is forced with 7 tidal constituents:  $M_2$ ,  $S_2$ ,  $O_1$ ,  $K_1$ ,  $Q_1$ ,  $N_2$ , and  $K_2$ . Two rivers are included in this set-up, the Hudson and Delaware Rivers. Discharge data was retrieved from U.S. Geological Survey (USGS) stations (<http://waterdata.usgs.gov.nwis/nwis>). As per Chant et al. (2008), the Hudson River discharge is 2 times the sum of the discharge of the Mohawk River at Cohoes and the Hudson at Ft. Edwards to account for additional freshwater input downstream of the gauges. The discharges of the Passaic and Raritan Rivers are added to the Hudson discharge. The Delaware River discharge is calculated to be 2 times the gauged discharge at the USGS station in Trenton, NJ to also account for downstream freshwater inputs. The ROMS model is forced by atmospheric variables (air temperature, humidity, pressure, evaporation/precipitation, short/longwave radiation, and winds) with output from the National Centers for Environmental Prediction (NCEP) North American Mesoscale Model (NAM) reanalysis to calculate the fluxes of momentum and heat across the air-sea interface.

The model is initialized with a mean condition calculated from a larger Mid-Atlantic Bight model over a 3 year period between the years 2006-2009. The model is

started on March 6, 2004 and allowed to spin-up for a year and a half. The time period analyzed in this study spans November 1, 2005 – February 28, 2006, or yearday 650-789 with respect to January 1, 2004. Note that for the analysis in this paper the output was averaged over 2  $M_2$  tidal cycles to remove the tidal influence.

### 4.3. Idealized Wind Simulations

Here we examine the results from the idealized wind simulations to better elucidate the response of the plume to the realistic forcings of the winter 2005-2006 simulations.

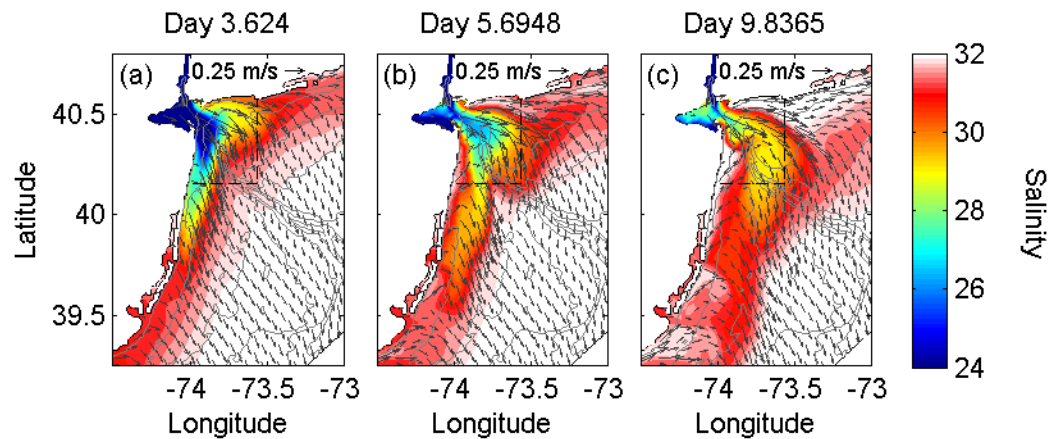


FIG 4.3. Tidally averaged surface salinity and velocity for the  $0^\circ$  model run for days 3.6 (a), 5.7 (b), and 9.8 (c)

#### 4.3.1. General plume response

The complex response to an offshore directed wind become rather apparent almost immediately after the wind forcing is applied. At the onset of wind forcing for the  $0^\circ$  degree model run (eastward wind), the plume temporarily splits into two different

pathways. The outer region of the bulge region near the outflow flows eastward along the Long Island coast while the New Jersey coastal current begins to be transported offshore (Fig 4.3a). After two days of wind forcing the New Jersey coastal current is now separated from the coast. The Long Island plume has now made a southward turn, but it still remains further offshore than the New Jersey plume (Fig 4.3b). Approximately 6 days after the onset of the wind forcing, the New Jersey plume has been transported eastward and has merged with what was the Long Island plume (Fig 4.3c). This forms a continuous pathway that initially flows east along Long Island, then turns southward and flows over the HSV, and continues southward in the middle of the shelf. There is a general southward flow on the offshore side of the plume, and a northward return flow on the inshore side.

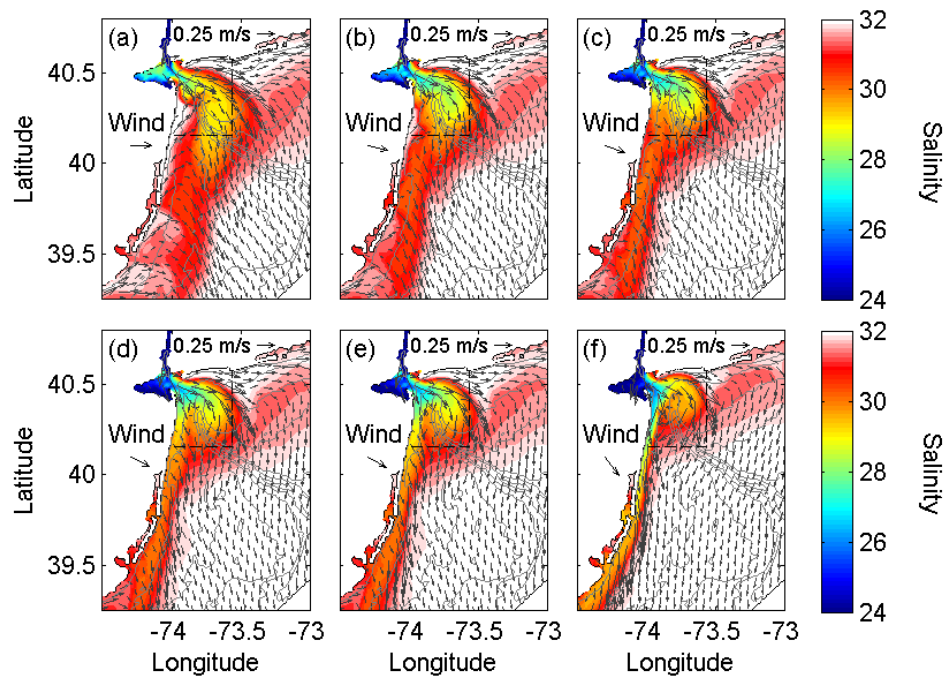


FIG 4.4. Tidally averaged surface salinity and velocity for the  $0^\circ$  (a),  $-10^\circ$  (b),  $-15^\circ$  (c),  $-20^\circ$  (d),  $-22.5^\circ$  (e), and  $-45^\circ$  (f) model runs on day 9, 6 days after the wind turned on.

The temporal response of the plume to winds with a downwelling component is similar to that of a true eastward wind, with the plume reaching a relative steady state in regards to plume position after approximately 7 days of wind forcing. The steady state plume position for all model runs is displayed in Figure 4.4. The factors controlling the offshore position of the plume will be discussed later in sub-section 4.3.5.

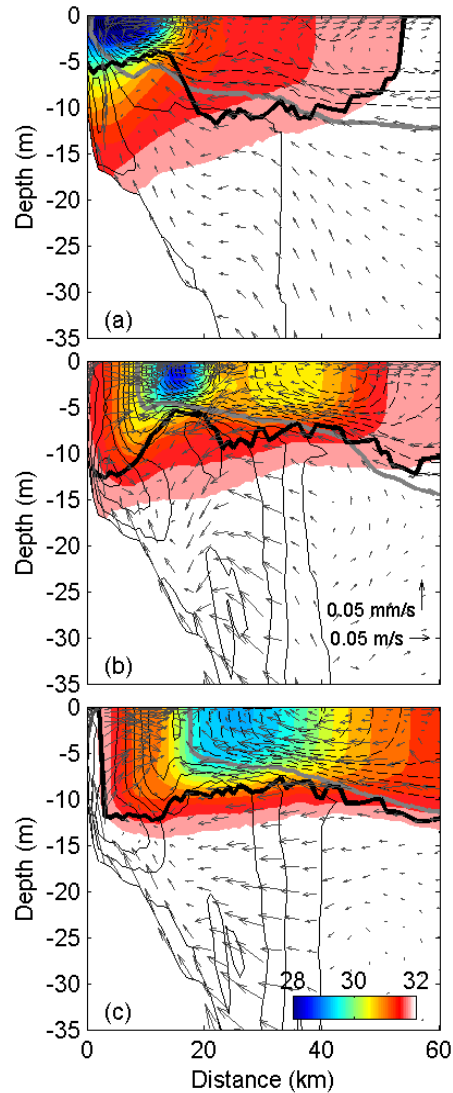


FIG 4.5. Cross-shore transect of velocity and salinity for the  $0^\circ$  run for days 3.6 (a), 5.7 (b) and 9.8 (a).

Salinity is contoured in color and n-s velocity is contoured in the thin black lines at  $0.025 \text{ m s}^{-1}$  intervals.

The thick black line signifies the plume depth, and the thick gray line is the zero isotach.

#### 4.3.2. *Cross-shore transects*

Cross-shore transects of the plume salinity and velocity are taken approximately 35 km downstream of the outflow, signified by the black dashed line in Figures 4.3 and 4.4. The evolution of the plume is evident in Figure 4.5 with the Long Island and New Jersey branches of the plume joining into one coherent structure. The plume starts out as a buoyant coastally trapped current at the onset of the offshore wind with a strong downstream velocity near the coast. The upstream velocity is just starting to develop near the coast as the low salinity core of the plume begins to be transported offshore. The velocity structure offshore of the plume core is primarily Ekman driven with the alongshore flow downstream in the surface layer and upstream at depth and the cross-shore flows offshore at the surface and onshore at depth (Fig 4.5a). After 2 days of the wind forcing there are now two distinct areas of low salinity passing through the transect (Fig 4.5b). There are also two corresponding downstream velocity maxima located just offshore of each of the salinity minima where the cross-shore wind stress and the baroclinic pressure gradient are the same sign. The plume is now a single, coherent structure after 6 days of wind forcing, with both plume branches merging (Fig 4.5c). The structure appears similar to what was reported in Jurisa and Chant (submitted) for an idealized model domain and wind forcing. There is a strong downstream jet on the offshore side and in this case a rather strong upstream flow on the inshore side of the plume. The cross-shore flows vary, however, with a net onshore flow over much of the plume on the offshore side except near the surface where it is offshore in response to the

wind. This is due to the plume angling toward the New Jersey coast at this location, leading to the net onshore flow.

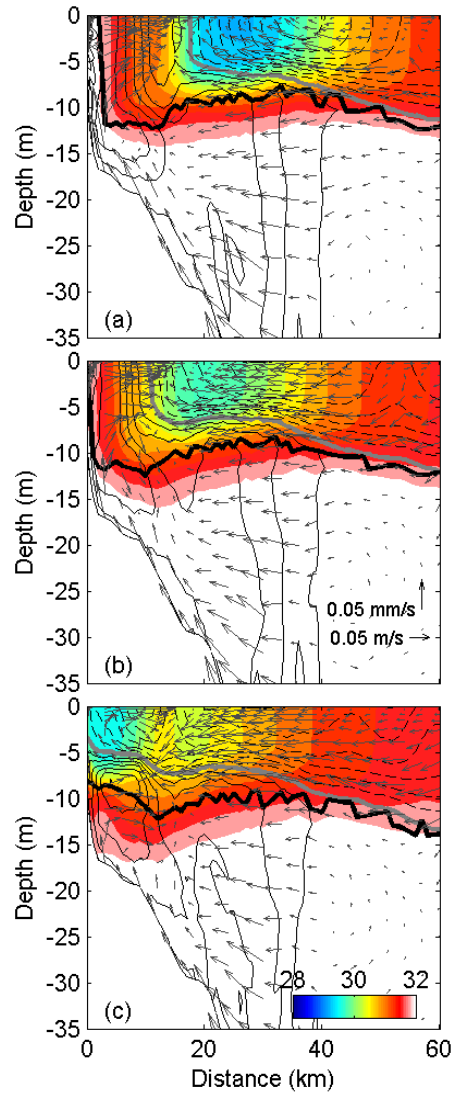


FIG 4.6. Cross-shore transect of velocity and salinity for the  $0^\circ$  (a),  $-10^\circ$  (b),  $-20^\circ$  (c) runs of day 9.8.

Salinity is contoured in color and n-s velocity is contoured in the thin black lines at  $0.025 \text{ m s}^{-1}$  intervals.

The thick black line signifies the plume depth, and the thick gray line is the zero isotach.

The cross-shore plume salinity and velocity transects for three of the model runs are plotted in Figure 4.6 when they have reached a steady state position. As the wind

rotates from  $0^\circ$  (Fig 4.6a) to  $-20^\circ$  (Fig 4.6c), the offshore position of the salinity minima move closer to the coast. Subsequently, the upstream flow on the inshore side of the plume reduces until the low salinity core reaches the coast.

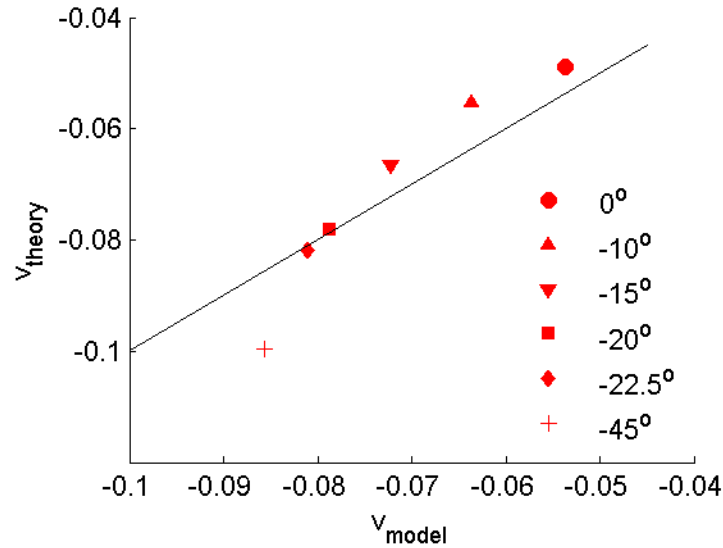


FIG 4.7. The model velocity and the theoretical velocity from (1) for all model runs on day 9.8.

#### 4.3.3. Plume-averaged parameters

To estimate the plume-averaged velocity, we use an approach similar to that of Jurisa and Chant (submitted) where the estimate of the velocity is simply the sum of the velocity components:

$$v_{\text{theory}} = v_{bt} + v_{Ek} + v_{amb} \quad (4.1).$$

Here,  $v_{bt} = g \partial \eta / \partial x f^{-1}$  is the upshelf flow due to the sea level set down near the coast and  $v_{Ek} = \tau_{wx} (\rho h_p f)^{-1}$  is the downshelf Ekman velocity due to the eastward component of the wind stress. In this case we add an additional term,  $v_{amb}$ , which is the mean ambient along shelf circulation imposed at the boundaries of the model domain. For this



part of the shelf,  $v_{amb} = 0.02 \text{ ms}^{-1}$ . Sea level is retrieved from the model output to calculate  $v_{bt}$ . The plume velocity from the model ( $v_{model}$ ) is cross-sectionally averaged over the width and depth of the plume. The results of the comparison are plotted in Figure 4.7. The velocity estimate,  $v_{theory}$ , compares well to the model plume velocity for runs with a wind direction ranging from  $0^\circ$  to  $-22.5^\circ$ . For the  $-45^\circ$  run, the theory overestimates the downstream plume velocity. This discrepancy can be due to the plume becoming attached to the bottom once it is pressed up against the coast, increasing the bottom friction, or the wind direction has begun to modify the ambient flow.

#### 4.3.4. *Plume mixing*

To get an understanding of the plume structure and its evolution, we must first get an understanding of the mixing within the plume. The vertical turbulent salt flux for the  $0^\circ$  model run is calculated from the model output for 3 time periods: the onset of wind, 2 days of wind forcing, and 6 days of wind forcing (Fig 4.8). The areas of high vertical salt flux correspond to the regions of maximum alongshore velocity in Figure 4.5. After 2 days of wind forcing there are two maxima in the vertical turbulent salt flux. There is one for each branch of the plume, the higher of which corresponds to the remnants of the New Jersey branch of the plume which has a higher vertical salinity and velocity gradient (Fig 4.8b). After the two branches merge after 6 days of wind forcing the area of higher vertical salt fluxes has broadened over the offshore side of the plume (Fig 4.8c). The mean vertical salt flux within the plume is plotted in Figure 4.8d, which also correlates the vertical salt flux at the base of the plume. The maximum in mixing can be seen during the initial adjustment period for days 3.6 and 5.7. In the offshore side of the plume, plume averaged vertical salt flux values remain nearly constant in time.

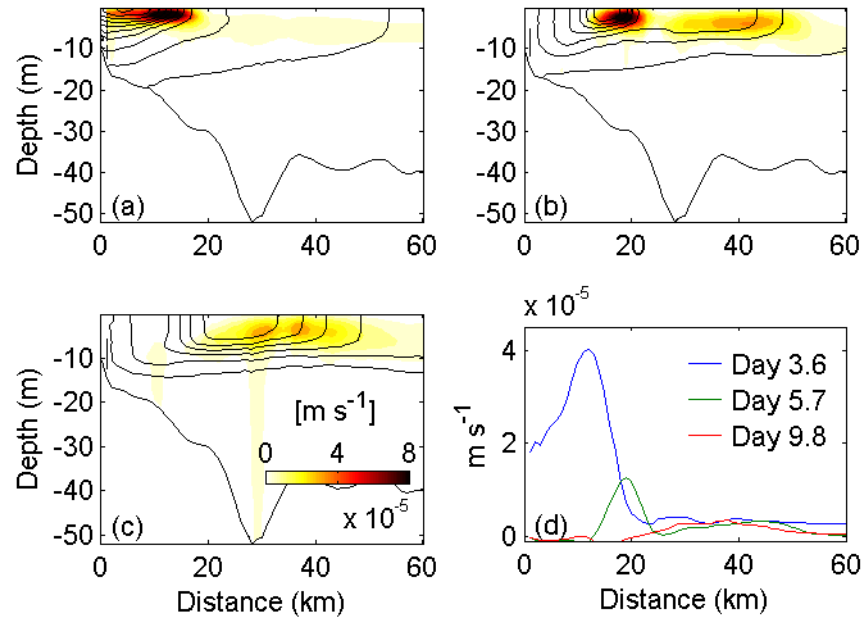


FIG 4.8. Vertical salt flux for the  $0^\circ$  run on day 3.6 (a), 5.7 (b), 9.8 (c), and the plume depth averaged vertical salt flux for the same days (d).

Unlike in the results of Chapter 3, the plume in these simulations does not reach a steady state in terms of plume salinity or depth over the duration of the run. The salt equation is analyzed to determine how the salinity structure of the plume is changing. For this analysis the time rate of change of salt equals the sum of the advective terms and the vertical divergence of the vertical turbulent salt flux (Fig 4.9). As in Chapter 3, the turbulent mixing is roughly balanced by the advective terms. Near the surface, the advective terms are working to transport saltier water offshore towards the center of the plume, and fresher water from the center of the plume towards the offshore edge (Fig 4.9c). At the base of the plume there is an onshore advection of saltier water. These advective processes are working to stratify the water column while the turbulent mixing term works to reduce the stratification. The structure of the salt rate indicate that the

plume is deepening and moving slightly offshore at this time period. Freshwater is moving away from the center of the plume, leading to an increase in the salinity at that location and freshwater is being transported offshore and mixed vertically, leading to a decrease in salinity at those locations, but increasing the total salt content of the plume at this location.

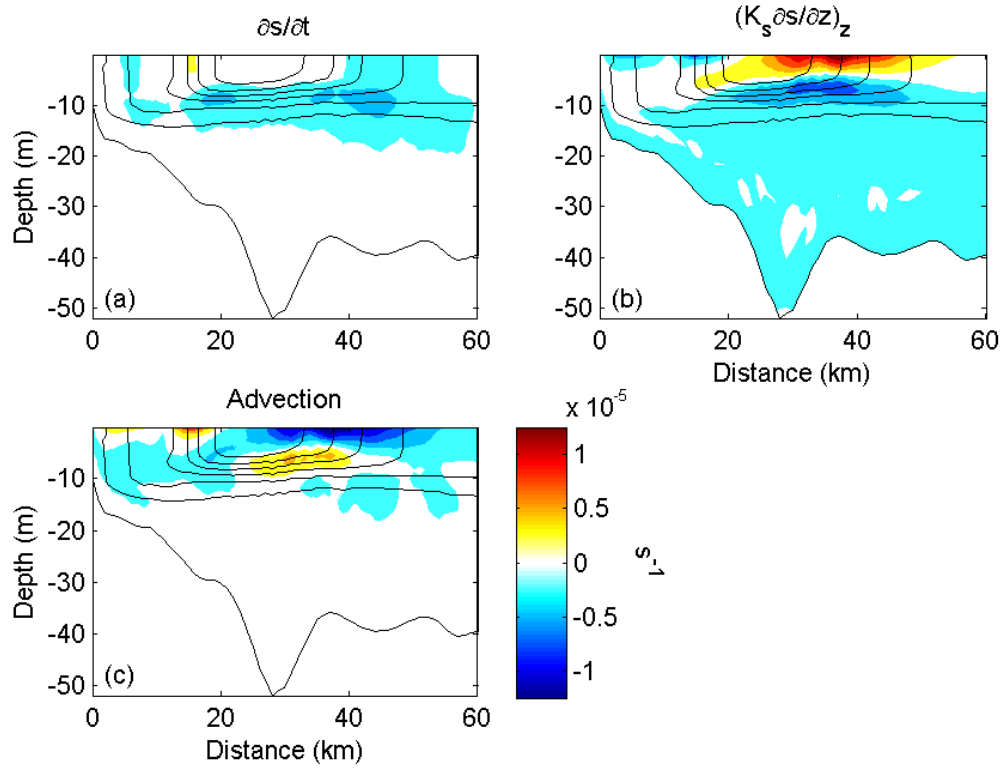


FIG 4.9. The salt rate (a), vertical divergence of the turbulent vertical salt flux (b) and the total advective term (c) for the  $0^\circ$  run on day 9.8.

#### 4.3.5. Offshore position and bulge formation

While the plume does not reach a steady state in terms of its salinity or depth, it does approach a steady state when it comes to its offshore position after approximately 6 days of wind forcing. The offshore extent of the plume is reduced with the increasing

downwelling component (Fig 4.4, 4.10, 4.11). With all cases, the furthest offshore extent of the plume occurs eastward of the mouth. While the onshore Ekman transport on the shelf from the downwelling component of the wind can explain some of the onshore movement, it is not the entire story; the cross-shore outflow momentum and the shelf circulation are important factors as well.

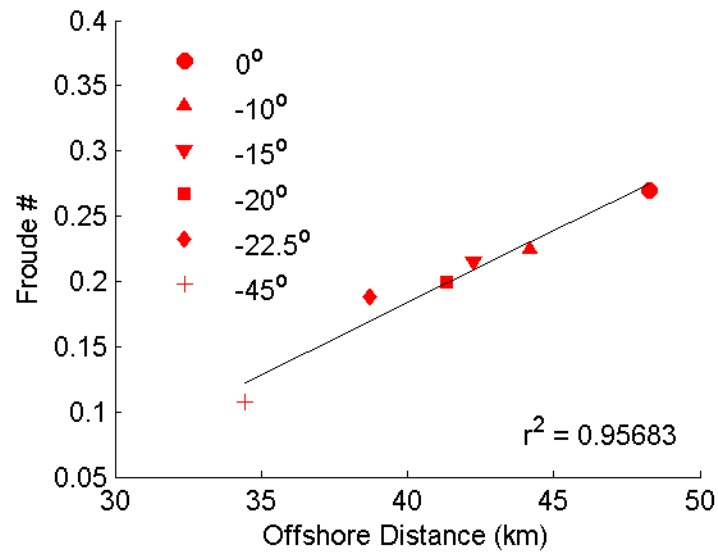


FIG 4.10. Offshore location of the plume in relation to the outflow Froude number on day 9.8 for all runs.

In all the simulations run here, a turning or bulge region develops near or offshore of the estuary mouth (Fig 4.4). For an unforced plume, the center of the recirculating bulge is related to the outflow Froude number,  $Fr = u / \sqrt{g'h}$ , where  $u$  is the cross-shore outflow velocity from the estuary,  $g'$  is the reduced gravity, and  $h$  is the depth of the outflow (Horner-Devine et al. 2006). The higher the Froude number, the further offshore the bulge center is advected. This theory holds true for Hudson River plume subjected to offshore winds as well. There is a strong correlation between higher outflow Froude

numbers and a large offshore extent (Fig 4.10). The  $0^\circ$  run has the largest Froude number due to the pure offshore wind due to the wind stress being aligned with the direction of the outflow. The  $-45^\circ$  run has the smallest Froude number with the strongest onshore Ekman velocity of all the runs.

The other factor impacting the offshore position of the Hudson River plume is the ambient circulation on the shelf. The mean circulation in the Mid-Atlantic Bight is generally southward following the isobaths, with the notable exception of the flow in the HSV which is directed up valley (Lentz, 2008). The outflow of the Hudson River is located in a rather interesting position at the apex of the NYB, separating the north-south oriented New Jersey and east-west Long Island coast. One of the consequences of this orientation is that the mean shelf circulation can interact with the plume *before* it makes a southward turn after crossing the HSV. This interaction can lead to the plume's offshore movement being inhibited. Another consequence of the position of the Hudson outflow in the NYB is that an eastward wind that is offshore relative to the New Jersey coast is an alongshore upwelling wind relative to Long Island. This leads to an eastward directed geostrophic current along the Long Island coast in response to the sea level set down. Since this eastward current occurs close to the Hudson outflow, the plume can be transported further eastward, until it interacts with the southwestward ambient shelf flow.

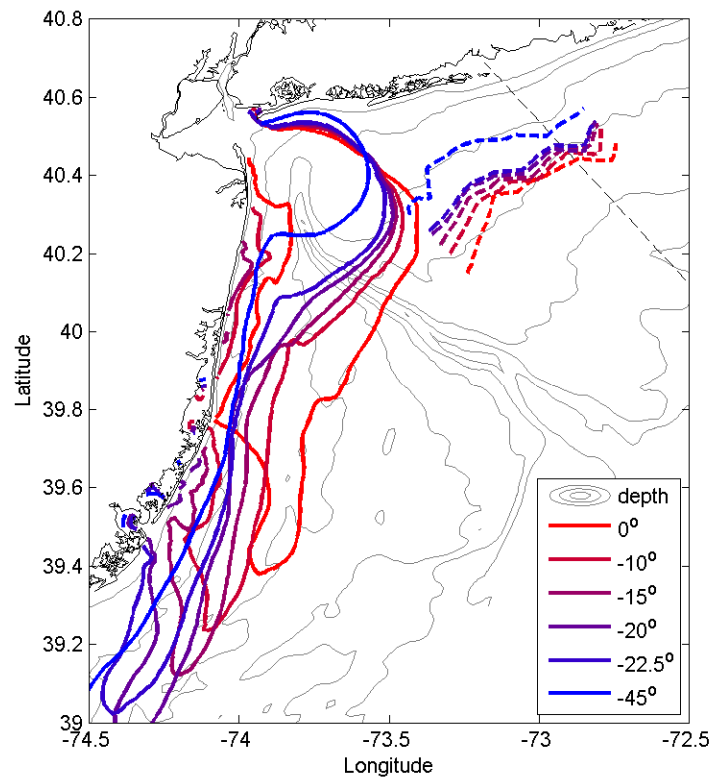


FIG 4.11. Location of the 31.5 isohaline on day 9.8 for all runs (solid colored contours) and the location of the transition zone between eastward and westward velocities (dashed colored lines).

The outer edge of the plume (salinity = 31.5) is contoured in Figure 4.11 for all the runs after 6 days of wind forcing (solid lines). Plotted along with that is the location offshore of Long Island that the depth averaged velocities change from the upwelling eastward flows near the coast and the westward ambient flows offshore. This location of this transition zone roughly correlates with the offshore position of the plume. In fact, the offshore position of the plume and the current transition zone relative to the respective  $-45^\circ$  run location is actually remarkably close. Southward of the velocity

transition zone, the plume edge angles back toward the New Jersey coast, with the steeper angle associated with the stronger southward wind.

Also of note is the continued presence of a recirculating bulge region near the mouth of the outflow, even for  $-45^\circ$  run, which theoretically should have the largest onshore flow. Surprisingly, the angle of the outflow is directed  $5^\circ$  to the north, *towards* Long Island. In fact, the outflow angle rotates from  $-5^\circ$  for the  $0^\circ$  run to  $5^\circ$  for the  $-45^\circ$  run. As a result, the plume is closest to the Long Island coast during the  $-45^\circ$  run, with the stronger downstream Ekman velocities of the other runs keeping the plume slightly further south.

## 4.4. Winter 2005-2006 Simulations

### 4.4.1. River discharge and wind forcing

The mean Hudson River discharge during the study period is  $1200 \text{ m}^3 \text{ s}^{-1}$ . The discharge exceeds  $2500 \text{ m}^3 \text{ s}^{-1}$  3 times (days 686, 700, and 749), with the maximum discharge of  $3850 \text{ m}^3 \text{ s}^{-1}$  occurring on day 749 (Fig 4.12a). Minimum values are around  $700 \text{ m}^3 \text{ s}^{-1}$ .

The winds used in this section are from the model forcing from the NCEP reanalysis. The data is taken from a location near Ambrose Light Tower (NOAA Station ID: ALSN6) and is filtered using a 36 hour cut-off frequency and a 72 hour window. As shown in Figure 1, the mean wind direction is towards the east-southeast. The winds shift to a more eastward phase between days 690-735, and between days 735-765 the winds are in a more variable phase (Fig 4.12b). The winds return to an eastward phase on day 765. For the purposes of this study we focus on 4 periods of offshore directed wind forcing, days 692-695 (event 1), 701-704 (event 2), 716-722 (event 3), and 767-772

(event 4). Event 1 has the wind direction with the smallest deviation from true east with a direction of  $-1.2^\circ$ , and also has the strongest velocity magnitude of  $9.2 \text{ m s}^{-1}$ . Event 3 has the largest downwelling wind component with a wind direction of  $-22.2^\circ$ . These four events are marked in Figure R10 by the vertical black arrows and are summarized in Table 4.1.

TABLE 4.1. Summary of the offshore wind events.

Event	Time	Wind Angle (degrees)	Wind Magnitude ( $\text{m s}^{-1}$ )
# 1	692-695	-1.2	9.2
# 2	701-704	-17.1	7.4
# 3	716-722	-23.3	6.8
# 4	767-772	-14.6	7.5

#### 4.4.2. General plume response

Despite the added complexities of variable wind and river forcing, the surface structure of the plumes for events 1-3 look similar to the simulations with an idealized steady offshore wind forcing (Fig 4.13, left panels). For both events 1 and 2, the plume has become detached from the coast and the buoyant discharge is flowing along the Long Island coast before turning south and eventually back toward the New Jersey coast. The cross-shore salinity and velocity structure shows a low salinity plume core with downstream velocities on the offshore side, and upstream velocities on the inshore portion of the plume. Event 3 has a considerable downwelling component, and as such, the low salinity water of the plume is still in touch with the coast (Fig 4.13e,f). There are also two low salinity branches observed in the cross-shore transect, which are the New



Jersey (inshore branch) and the Long Island (offshore branch) branches of the plume described in the previous section. There is a downstream velocity jet on the offshore side of the plume, but on the inshore side there a downstream flow as well, where the salinity minimum is located, which is surrounded by upstream velocities.

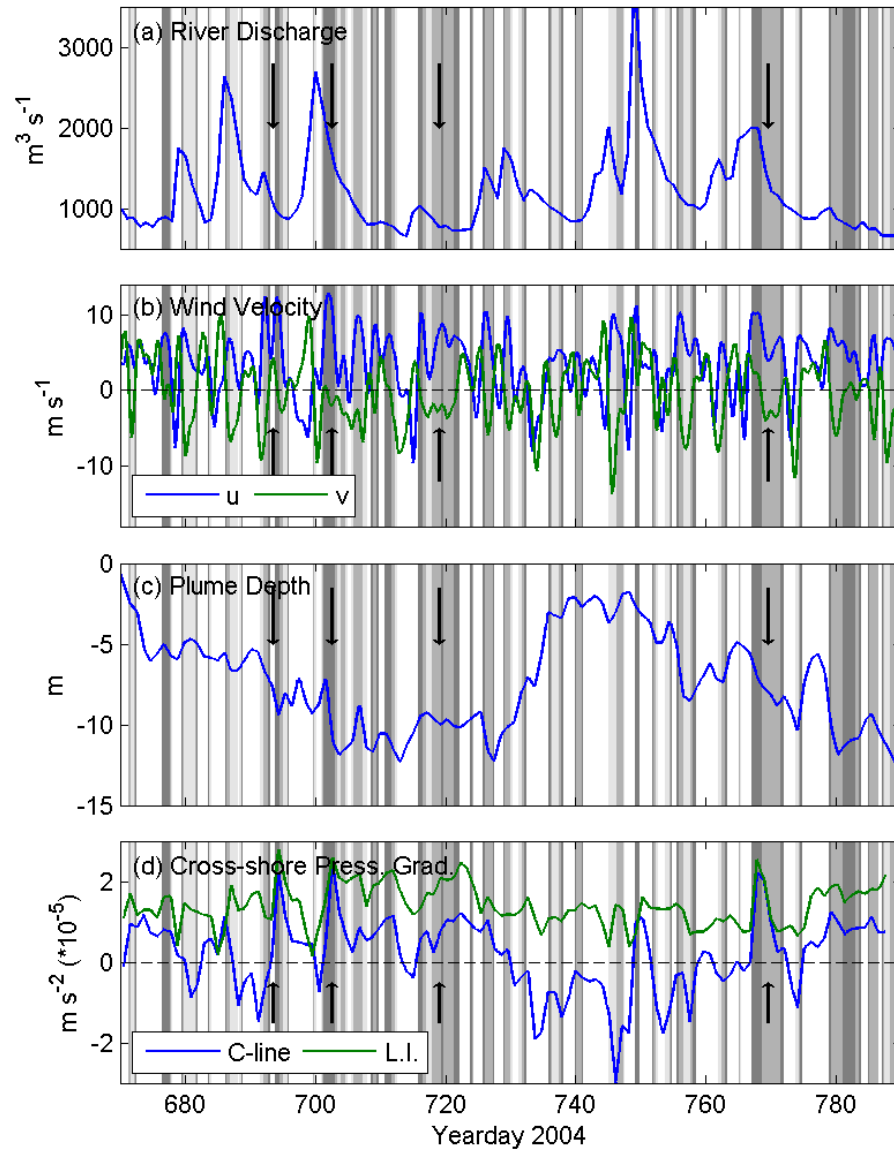


FIG 4.12. Hudson River discharge (a), e-w and n-s wind velocities (b), plume depth averaged across the cross-shore transect along with the average freshwater depth ( $\times 15$ ) (c), and the cross-shore pressure

gradient on the New Jersey coast (C-line) and the Long Island coast (L.I.) (d). Gray shade areas signify winds with a direction between  $5^\circ$  and  $-75^\circ$  with respect to east. Dark grays represent eastward winds.

The response of the plume during event 4 diverges from the response of the previous 3 events and the results of the idealized wind simulations. Event 4 exhibits a strong coastally trapped buoyant current and a bulge of fresher water near the mouth of the outflow (Fig 4.13g,h). While the mean wind direction and speed during this period is  $-14.6^\circ$  and  $7.5 \text{ m s}^{-1}$  respectively, these parameters change over the course of the event. In this case, during the end of the event, the wind direction is approximately  $-30^\circ$  and the magnitude is around  $5.5 \text{ m s}^{-1}$ . This weaker wind with a more downwelling orientation allows the plume to remain attached to the coast, while the bulge region offshore of the mouth is the remnant of plume that was previously subjected to an offshore wind with a slight upwelling component.

The alongshore velocity in the plumes during the offshore wind events is downstream on the offshore side of the plume and upstream towards the mouth of the estuary on the inshore side of the plume. In Chapter 3 it is noted that the alongshore velocity structure is consistent with a balance between the cross-shore pressure gradient, wind stress, and the coriolis acceleration. On the offshore side of the plume, the stress and pressure gradient work in concert to drive the downstream flow, while on the inshore side, those terms oppose each other. This balance led to very weak upstream flows on the inshore side in the idealized simulations in Chapter 3. However, here we observe strong upstream flows during offshore wind events easily exceeding  $20 \text{ cm s}^{-1}$ . The cross-shore barotropic pressure gradients for these realistic simulations are rather large during events 1, 2, and 4 (Fig 4.12d). The cross-shore pressure gradient for these events is in fact

actually larger than for an upwelling favorable response (e.g. day 698 in Fig 4.12d). This amplified response of the sea level to the offshore winds is a factor in driving the rather strong upstream flows on the inshore side of the plume.

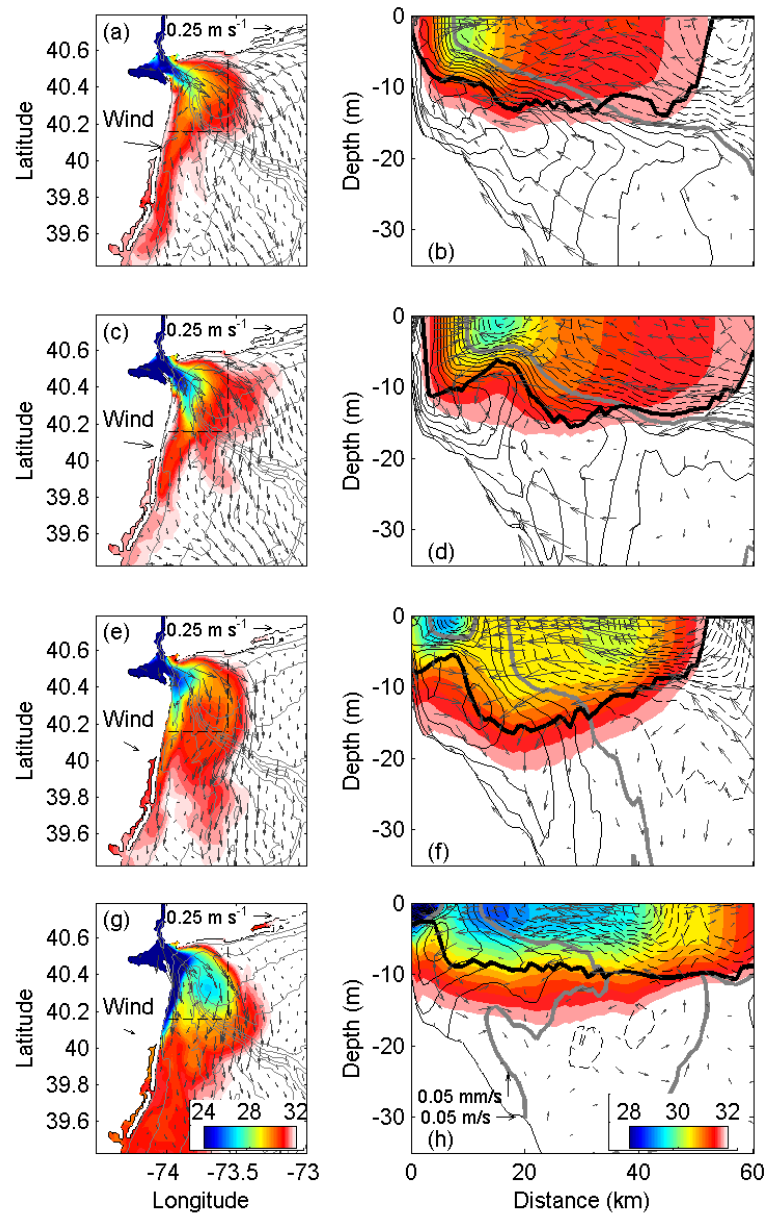


FIG 4.13. Tidally averaged surface salinity and velocity (left panels) and cross-shore transects of tidally average velocity and salinity (right panels) for event 1 (a,b), event 2 (c,d), event 3 (e,f), and event 4 (g,h).

Salinity is contoured in color and n-s velocity is contoured in the tin black lines at  $0.025 \text{ m s}^{-1}$  intervals.

The thick black line signifies the plume depth, and the thick gray line is the zero isotach.

#### 4.4.3. *Plume mixing*

The strong upstream flows on the inshore side of the plume lead to the development of strong lateral velocity shears as well. That lateral shear, as well as having relatively strong offshore velocities on the inner portion of the plume combating the onshore flows at depth on the outer portion can lead to a rather complicated mixing structure. Here, using event 1 as an example, the mixing of the plume will be addressed by first describing the turbulent vertical salt flux and then the terms in the salt equation.

The vertical salt flux is calculated by vertically integrating  $(K_s \partial s / \partial z)_z$  from the model output from the surface to the bottom. Plume depth averaged vertical salt flux quantities are averaged from the surface to the plume depth, defined as the depth where  $\Delta\rho = 0.5 * (\rho_o - \rho_{surface})$ . The evolution of the turbulent vertical salt flux for event 1 (days 692-694) is plotted in Figure 4.14. When the wind shifts to an offshore direction, the plume is initially trapped up against the coast and highly stratified. The increased wind stress drives strong vertical mixing on the edge of the low salinity core of the plume. On day 693, the plume has now begun to spread offshore and the maximum vertical salt flux still reside near shore, but is considerably lower. On day 694, as shown in Fig 4.14c, the low salinity core of the plume is now detached from the coast, and the high values to turbulent mixing are found just offshore of the low salinity core where the vertical velocity shears are the largest. The maximum values of the plume depth averaged turbulent salt fluxes are consistent over days 692 and 694. However, higher

values of turbulent mixing are maintained over the offshore side of the plume on day 694 compared to day 692 (Fig 4.14d). The reduced turbulent mixing values on day 693 can be attributed to the 3-fold decrease in the wind speed in relation to days 692 and 694.

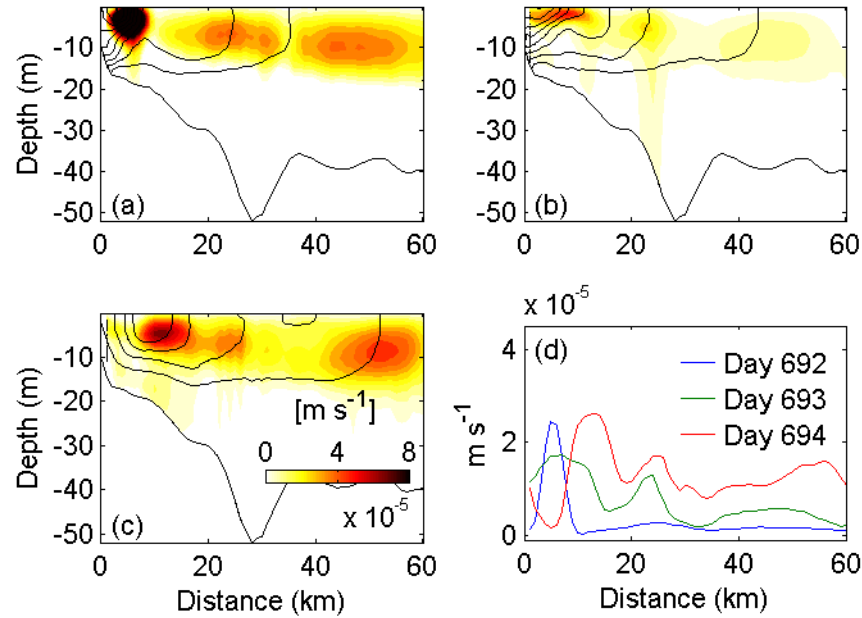


FIG 4.14. Vertical salt flux for the event 1 on day 692 (a), 693 (b), 694 (c), and the plume depth averaged vertical salt flux for the same days (d).

The plume during event 1 is continually mixed and transported offshore for the length of the event. This transport is evident in the salt rate of the plume on day 694 (Fig 4.15a). As the plume is slowly moving offshore, the plume gets saltier near shore as the fresh water in the plume is replaced by saltier shelf waters, while the offshore portion of the plume freshens as the lower salinity waters are advected offshore. The advection of the salinity field works to salten the plume on the inshore side by the cross-shore advection of saltier water offshore along with the alongshore advection of more saline water upstream (Fig 4.15c). Offshore of the low salinity core, the fresher water is being

advected downstream and in the cross-shore direction fresher water is being advected offshore at the surface and saltier water is advected onshore at depth, strengthening the plumes stratification. That stratification is being mixed away by the turbulent mixing processes (Fig R13b)

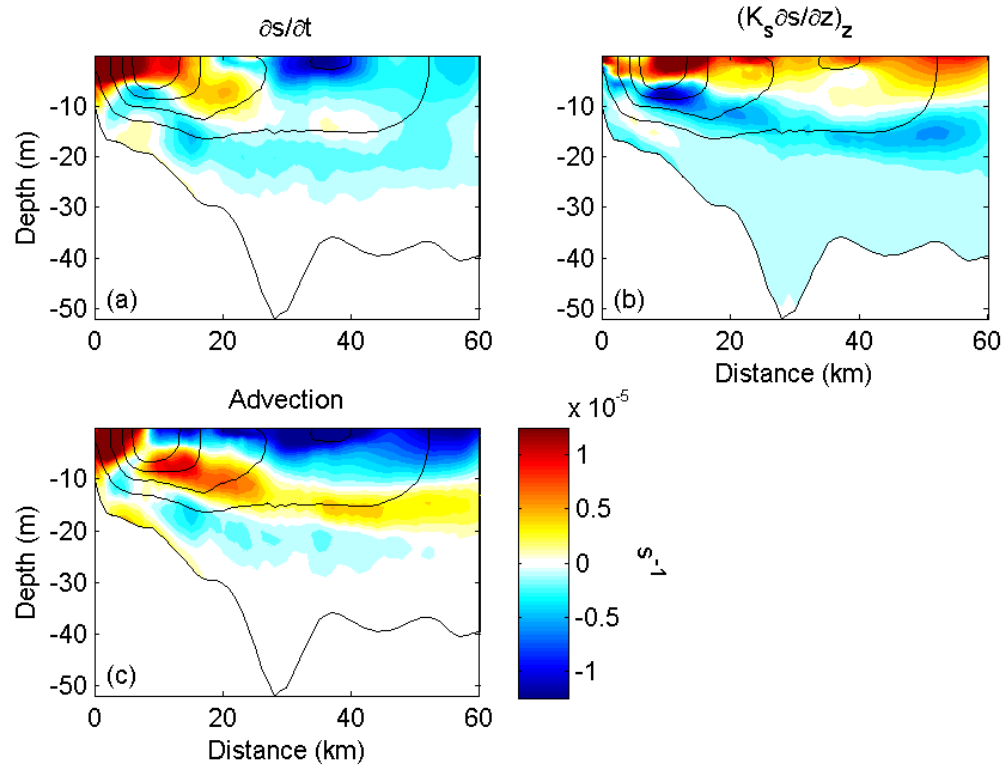


FIG 4.15. The salt rate (a), vertical divergence of the turbulent vertical salt flux (b) and the total advective term (c) for event 1 on day 694.

#### 4.4.4. Plume depth

Over the course of the simulation, the plume depth varies between 2 and 12 m (Fig 4.12c). The plume gradually deepens from day 670 to day 730, where it then continually thins over a ten day period before hold steady at a thickness around 3 m for the next 20 days. The plume then begins to gradually thicken again around day 760 for the

remainder of the run. The large changes in plume depth over the simulation are correlated with offshore winds. During the two periods of increasing plume thickness, the dominant wind direction is offshore. The relatively rapid thinning of the plume from day 730-740 coincided with a period of weaker and more alongshore-oriented winds. The plume did not start to thicken until an offshore wind starting on day 755, with another on following on day 767 (event 4). This change in winds can be seen in the record of the cross-shore pressure gradient (Fig 4.12d). During the periods of offshore wind when the plume was deepening, there is a sea level set down along the New Jersey coast (positive values on Fig 4.12d). While during the period when the plume was either thinning or steady, there is a sea level set up along the coast, indicative of downwelling winds. This relationship between the plume depth and wind direction suggests that plume deepening is inhibited for the Hudson River plume during downwelling winds compared to offshore winds.

## 4.5. Summary

This study has examined the effects of offshore directed winds on the Hudson River plume using semi-idealized and realistic numerical simulations. For the  $0^\circ$  run in the semi-idealized simulations, the plume is found to initially form one branch of freshwater that travels along the Long Island coast before turning south and flowing over the HSV and another branch of the plume that consists of the New Jersey coastal current that becomes detached from the coast. The two branches eventually merge after 6 days of wind forcing to form a unified southward freshwater transport pathway in the Mid-Atlantic Bight.

As the direction of the wind becomes more downwelling, the far field plume is pushed closer to the New Jersey coast. The bulge region also becomes more constrained to the New Jersey coast. However, the bulge region is still a remarkably prominent and robust feature in all the semi-idealized simulations. As in Horner-Devine et al. (2006), the position of the plume can be described using a outflow Froude number where the higher the Froude number, the further offshore the bulge center will be located. The offshore position of the plume is also related to the ambient shelf circulation, specifically the flow along the Long Island coast. The offshore location where the alongshore currents transition from eastward to westward correlates to the offshore position of the plume.

Over the course of all the semi-idealized runs while the plume did reach a quasi-steady state in regards to its position, it never reached a steady state in terms of its depth or velocity and salinity structure. This is in contrast to the idealized results of Chapter 3 where the plume reaches a steady state after a few inertial periods. It should be noted that the plume depth does not follow the simple scaling of a critical Richardson number from previous studies (Fong and Geyer 2001, Lentz 2004, Hetland 2005, Jurisa and Chant 2012). The cross-shore variation in the velocity structure of the lower layer is not accounted for using the simple Richardson number scaling using plume width-averaged quantities and assuming a quiescent lower layer.

The plume structure during offshore wind events in the realistic simulations of the 2005/2006 winter season compared rather well with the results of the semi-idealized runs. As the offshore wind events predictably fell within the synoptic weather band of 2-5



days, the quasi-steady state position of the plume could not be observed, since the response time of the plume to the wind forcing falls outside the weather band.

The change of plume depth was found to be correlated with the direction of the wind forcing. The plume noticeably thickened during periods of offshore directed winds, and thinned or remained steady during more downwelling favorable periods. This relationship is possibly due to the plume being more compressed under more downwelling conditions, which would increase the buoyancy term relative to the shear term. Also, the plume would be constrained to shallower depth, limiting the ability to entrain ambient fluid into the plume through vertical mixing processes as is observed in the idealized model results of Moffat and Lentz (2012).

This study is part of a process to give a more complete picture of what is driving the freshwater transport pathways in the NYB. It must be noted that even though the freshwater transport in a plume subjected to offshore winds is in the downstream direction, it is fundamentally different than the downwelling response; the plume is no longer constrained by the coast. This has enabled us to give a more detailed description of the Hudson River plume and the resulting freshwater transport pathways during the winter when offshore winds are the dominant wind forcing.



## **Chapter 5:**

### **Summary**

In Chapter 2 the response of the Hudson River plume to variable river, wind, and shelf forcings is described. During the 2006 LaTTE field campaign the plume is observed to detach from the coast just downstream from outflow and form a downstream recirculating region. This downstream feature was remarkably and surprisingly persistent over a 2 week period of downwelling winds. It is hypothesized that the onshore wind that preceded the formation of the feature and the subsequent relaxation enhanced the already high river discharge. This released a large amount of freshwater onto the shelf in a rather short time period. The large plume was then hit by a brief upwelling wind event that transported the plume in the offshore direction, with the HSV constraining the offshore movement. Once the wind relaxes, the plume geostrophically adjusts and forms the downstream recirculation feature. The longevity of this feature is explained using the Wedderburn number, which is the ration between the wind and buoyant forcing terms. Periods of where the wind stress term is dominant bracket the time period when the plume is observed, suggesting the wind during the time period the downstream feature was present was not strong enough to significantly alter the structure.

In Chapter 3, the effects of an offshore directed wind stress on a buoyant plume system is explored using idealized numerical model domain and forcing. Once subjected to the offshore winds, the plume is observed to be rapidly transported offshore within a few inertial periods at which point it reaches a steady state in terms of position, depth, velocity, and density. The plume now resembles an elongated eddy. The depth is parameterized using a critical Richardson number criterion. The mean plume velocity is found to be the sum of the downstream Ekman velocity and the upstream geostrophic barotropic velocity due to the sea level set down at the coast. The mean density in the

plume is estimated assuming the conservation of freshwater within the transect. This assumption of freshwater conservation is invalid for initial conditions that contain a large bulge region at the onset of the wind stress as the bolus of freshwater is transported downstream. This large input of freshwater into the transect leads the theory to overestimate the plume density. However, reasonable agreement is reached with model runs with a limited bulge region at the onset of the wind stress (wide outflow, low discharge runs). This assumption of freshwater conservation leads to problems with the estimate of the plume width; however, the low discharge, wide outflow runs have a reasonable agreement. The offshore position of the center of the plume is a balance between the offshore momentum of the outflow and the downstream momentum from the Ekman velocities. This relationship is expressed using a ratio of the plume and estuarine Froude numbers. As in Horner-Devine et al. (2006), higher Froude number outflows produce a plume that is further offshore.

Mixing in the plume is also examined at a cross-shore transect. The plume maintains a steady salinity structure in an Eulerian reference frame through a salt balance between the alongshore and cross-shore advection and the divergence of the vertical salt flux. To get a broader view of plume-wide mixing, the freshwater volume of the plume was tracked in time and salinity space. A mixing interface develops in salinity space that delineates regions where freshwater is being lost or held constant and regions in salinity space that are gaining freshwater. Using a critical Richardson number formulation, a critical mixing ratio is developed. Utilizing this mixing ratio elucidates the near, mid, and far field regions of the plume in salinity space.

In Chapter 4, numerical simulations of the New York Bight and the Hudson River plume are carried out using idealized river and offshore directed wind forcings along with a fully realistic run of the 2005/2006 winter season. For an offshore directed wind, the Hudson River plume response very generally compares to the idealized case. However, there are important differences: the plume does not reach a steady-state structure, the Hudson plume is 2 times as wide an idealized case with similar wind and river forcing, and the upstream flow in the inshore side of the plume is substantially greater for the Hudson River plume. Several simulations are run with once again a steady river and wind forcing, except the downwelling component of the wind stress differs for each run. As the downwelling component increases, the plume's offshore distance decreases. The offshore position of the plume at the outflow is dependent on the outflow Froude number and the Long Island influenced shelf flows. The upwelling current that develops along the coast of Long Island draws the plume further east and the generally westward ambient shelf current forces the far field of the plume closer to New Jersey. The transition zone between these two currents is correlated to the plume position and structure.

The differences between the idealized plume response and the response of the Hudson River plume highlight the complexities of the New York Bight region and the role of Long Island in the dispersal of freshwater. The results presented here begin to describe the structure of the freshwater transport pathways in the New York Bight in the winter described by Zhang et al. (2009) when offshore directed winds are dominant. The Hudson River plume shows a strong upstream flow on the inshore side of the plume, which is consistent with Zhang et al.'s (2009) findings of upstream freshwater transport along the New Jersey coast during the winter. Since a buoyant plume reaches a general

steady offshore position in response to offshore directed winds, it is not as efficient of a mechanism to continually transport freshwater across the shelf. However, this study has shown that the plume response to offshore winds can create significant and persistent salinity induced stratification on the inner shelf. While cross-shore winds are a ubiquitous forcing mechanism along the East Coast, this offshore wind forcing is especially important in the New York Bight where the presence of Long Island leads to the formation of plume on the order of 60km wide. As a river plume can serve as a pipeline from the terrestrial to coastal ocean regions, this response can be vitally important to the biogeochemical cycles on the shelf. Xu et al. (2011) describes the winter phytoplankton bloom off the coast of New Jersey in the winter and finds that it typically lies between the 20 and 60 m isobaths. It is within this region that the Hudson River plume, which is subject to winter offshore winds, is typically located as well. The presence of the plume, with the stratification and nutrients that comes with it, could possibly play a role in the formation of this winter bloom in the Mid-Atlantic Bight.

This dissertation provides a description and analysis of the response of a buoyant plume to offshore winds through the use of idealized and realistic modeling and the response of the Hudson River plume to the complex forcing mechanisms in the New York bight. The role of the complex geometry of the New York Bight in the response of the Hudson River plume to cross-shore winds, more specifically the role of the Hudson Shelf Valley, still needs to be more fully understood. However, the results of this dissertation greatly advance the knowledge of buoyant river plume response to wind forcing, and it lays another piece of the foundation for future work in the Mid-Atlantic Bight and on river plumes in general.

### Acknowledgement of Previous Publications

Chapter 2 has been published in the scientific journal *Ocean Dynamics*.

Jurisa, J. T. and R. J. Chant, 2012: The coupled Hudson River estuarine-plume response to variable wind and river forcings. *Ocean Dyn.*, **62**, 771-784.

Chapter 3 has been submitted for publication in the scientific journal, *Journal of Physical Oceanography*.

Jurisa, J. T. and R. J. Chant, submitted: Impact of offshore winds on a buoyant plume system. *J. Phys. Oceanogr.*



## References

- Avicola, G. and P. Huq, 2003: The characteristics of the recirculating bulge region in coastal buoyant outflows. *J. Mar. Res.*, **61**, 435-463.
- Castelao R, O. Schofield, S. Glenn, R. J. Chant, J. Kohut, 2008: Cross-shelf transport of freshwater on the New Jersey shelf. *J. Geophys. Res.*, **113**, C07017 doi:10.1029/2007JC004241
- Chapman, D. C., 1985: Numerical treatment of cross-shelf open boundaries in a barotropic coastal ocean model. *J. Phys. Oceanogr.*, **15**, 1060–1075.
- Chant, R. J., S. M. Glenn, E. Hunter, J. Kohut, R. F. Chen, R. W. Houghton, J. Bosch, and O. Schofield, 2008a: Bulge formation of a buoyant river outflow. *J. Geophys. Res.*, **113**, C01017, doi: 10.1029/2007JC004100.
- Chant, R.J., J. Wilkin, W. Zhang, B.-J. Choi, E. Hunter, R. Castelao, S. Glenn, J. Jurisa, O. Schofield, R. Houghton, J. Kohut, T.K. Fraser, and M.A. Moline, 2008b: Dispersal of the Hudson River plume in the New York Bight. *Oceanogr.*, **21**, 148-161.
- Chen, S.-N. and P. Sanford, 2009: Axial wind effects on stratification and longitudinal salt transport in an idealized, partially mixed estuary. *J. Phys. Oceanogr.*, **39**, 1905-1920.
- Choi, B. J. and J. L. Wilkin, 2007: The effect of wind on the dispersal of the Hudson River plume. *J. Phys. Oceanogr.*, **24**, 1878-1896.
- Chao, S.-Y. and W. C. Boicort, 1986: Onset of estuarine plumes. *J. Phys. Oceanogr.*, **16**, 2137-2149.
- Chao, S.-Y., 1988: Wind-driven motion of estuarine plumes. *J. Phys. Oceanogr.*, **18**, 1144-1166.
- Ekman, V. W., 1905: On the influence of the earth's rotation on ocean currents. *Ark. Mat. Aston. Fys.*, **2**, 1-53.
- Fewings, M., S. J. Lentz, and J. Fredericks, 2008: Observations of cross-shelf flow driven by cross-shelf winds on the inner continental shelf. *J. Phys. Oceanogr.*, **38**, 2358-2378.
- Flather, R. A., 1976: A tidal model of the northwest European continental shelf. *Mem. Soc. Roy. Sci. Liege*, **6**, 141–164.

- Fong, D. A., W. R. Geyer, and R.P. Signell, 1997: The wind-forced response on a buoyant coastal current: observations of the western Gulf of Maine plume. *J. Mar. Syst.*, **12**, 69-81.
- Fong, D. A. and W. R. Geyer, 2001: Response of a river plume during an upwelling favorable wind event. *J. Geophys. Res.*, **106**, 1067-1084.
- Fong, D. A. and W. R. Geyer, 2002: The alongshore transport of freshwater in a surface-trapped river plume. *J. Phys. Oceanogr.*, **32**, 957-972.
- Garvine, R. W., 1985: A simple model of estuarine subtidal fluctuations forced by local and remote wind stress. *J. Geophys. Res.*, **90**, 11945-11948.
- Garvine, R. W., 1995: A dynamical system for classifying buoyant discharges. *Cont. Shelf Res.*, **15**, 1585-1596.
- Garvine, R. W., 1999: Penetration of buoyant coastal discharge onto the continental shelf: a numerical model experiment. *J. Phys. Oceanogr.*, **29**, 1892-1909.
- Geyer, W.R., 1997: Influence of wind on dynamics and flushing of shallow estuaries. *Estuarine, Coastal and Shelf Science*, **44**, 713-722.
- Haidvogel, Dale B., H. Arango, W.P. Budgell, B.D. Cornuelle, E. Curchitser, E. DiLorenzo, K. Fennel, W.R. Geyer, A.J. Hermann, L. Lanerolle, J. Levin, J.C. McWilliams, A.J. Miller, A.M. Moore, T.M. Powell, A.F. Shchepetkin, C.R. Sherwood, R.P. Signell, J.C. Warner, J. Wilkin (2008), Ocean forecasting in the terrain-following coordinates: Formulation and skill assessment of the Regional Ocean Modeling System. *J. Computational Physics*, **227**, 3595-3624.
- Harris, C. K., B. Butman, and P. Traykovski, 2003: Winter-time circulation and sediment transport in the Hudson Shelf Valley. *Cont. Shelf Res.*, **23**, 801-820.
- Hetland, R. D., 2005: Relating river plume structure to vertical mixing. *J. Phys. Oceanogr.*, **35**, 1667-1688.
- Hetland, R. D. and D. G. MacDonald, 2008: Spreading in the near-field Merrimack River plume. *Ocean Modell.*, **21**, 12-21.
- Hickey, B., S. Geier, N. Kachel, and A. MacFadyen, 2005: A bi-directional river plume: The Columbia in summer. *Cont. Shelf Res.*, **25**, 1631-1656.
- Horner-Divine, A. R., D. A. Fong, S. G. Monosmith, and T. Maxworthy, 2006: Laboratory experiments simulating a coastal river inflow. *J. Fluid. Mech.*, **555**, 203-232.

- Horner-Devine, A. R., 2009: The bulge circulation in the Columbia River plume. *Cont. Shelf Res.*, **29**, 234-251.
- Hunter, E. J., R. J. Chant, J. L. Wilkin, and J. Kohut, 2010: High-frequency forcing and subtidal response of the Hudson River plume. *J. Geophys. Res.*, **115**, C07012, doi: 10.1029/2009JC005620.
- Huq, P., 2009: The role of Kelvin number on bulge formation from estuarine buoyant outflows. *Estuaries and Coasts*, **32**, 709-719.
- Jurisa, J. T. and R. J. Chant, 2012: The coupled Hudson River estuarine-plume response to variable wind and river forcings. *Ocean Dyn.*, **62**, 771-784.  
- Chapter 2 of this dissertation
- Jurisa, J. T. and R. J. Chant, submitted: Impact of offshore winds on a buoyant plume system. *J. Phys. Oceanogr.*  
- Chapter 3 of this dissertation
- Lentz, S.J. and K.R. Helfrich, 2002: Buoyant gravity currents along a sloping bottom in a rotating fluid. *J. Fluid Mech.*, **464**, 251-278.
- Lentz, S. J., 2004: The response of buoyant coastal plumes to upwelling favorable winds. *J. Phys. Oceanogr.*, **43**, 2458-2469.
- Lentz, S.J. and J. Largier, 2006: The influence of wind forcing on the Chesapeake Bay coastal current. *J. Phys. Oceanogr.*, **36**, 1305-1316.
- Lentz, S.J., 2008: Observations and a model of the mean circulation over the Middle Atlantic Bight continental shelf. *J. Phys. Oceanogr.*, **38**, 1203-1221.
- Lerczak, J. A., W. R. Geyer, and D. K. Ralston, 2009: The temporal response of the length of a partiall stratified estuary to changes in river flow and tidal amplitude. *J. Phys. Oceanogr.*, **38**, 915-933.
- MacCready, P., R. D. Hetland, and W. R. Geyer, 2002: Long-term isohaline salt balance in an estuary. *Cont. Shelf Res.*, **22**, 1591-1601.
- MacDonald, D. G., L. Goodman, and R. D. Hetland, 2007: Turbulent dissipation in a near-field river plume: A comparison of control volume and microstructure with a numerical model. *J. Geophys. Res.*, **112**, C07026, doi:10.1029/2006JC004075.
- Moffat, C., and S. J. Lentz, 2012: On the Response of a Buoyant Plume to Downwelling-Favorable Wind Stress. *J. Phys. Oceanogr.*, doi:10.1175/JPO-D-11-015.1, in press.

- Monismith, S., 1987: Modal response to reservoirs to wind stress. *J. Hydraulic. Eng.*, **113**, 1290-1306.
- Münchow, A. and R. J. Chant, 2000: Kinematics of inner shelf motion during the summer stratified season off New Jersey. *J. Phys. Oceanogr.*, **30**, 247-268.
- Nof, D., 1998. Eddy-wall interactions. *J. Mar. Res.*, **46**, 527-555.
- Pollard, R. T., P. B. Rhines, and R. O. R. Y. Thompson, 1973: The deepening of the wind-mixed layer. *Geophys. Fluid Dyn.*, **3**, 381-404.
- Ralston, D. K., W. R. Geyer, and J. A. Lerczak, 2008: Subtidal salinity and velocity in the Hudson River estuary: observation and modeling. *J. Phys. Oceanogr.*, **38**, 753-770.
- Rennie, S. E., J. L. Largier, and S. J. Lentz, 1999: Observations of a pulsed buoyancy current downstream of Chesapeake Bay. *J. Geophys. Res.*, **104**, 18227-18240.
- Shchepetkin, A. F., and J. C. McWilliams, 2005: The Regional Oceanic Modeling System (ROMS): A split-explicit, free-surface, topography-following coordinate oceanic model. *Ocean Modell.*, **9**, 347-404.
- Shchepetkin, A. F., and J. C. McWilliams, 2009a: Computational kernel algorithms for finescale, multi-process, long-term oceanic simulations. In: Temam, R., Tribbia, J. (Guest Eds.), Computational Methods for the Ocean and the Atmosphere, P.G. Ciarlet (Ed.), Handbook of Numerical Analysis, vol. XIV, pp. 119-182, Elsevier Science, doi: 10.1016/S1570--8659(08)01202--0.
- Shchepetkin, A. F., and J. C. McWilliams, 2009b: Correction and commentary for “Ocean forecasting in terrain-following coordinates: Formulation and skill assessment of the regional ocean modeling system” by Haidvogel et al., *J. Comp. Phys.* 227, pp. 3595-3624. *J. Comp. Phys.*, **228**, 8985-9000, DOI: 10.1016/j.jcp.2009.09.002.
- Tilburg, C. E., 2003: Across-shelf transport on a continental shelf: Do across-shelf winds matter? *J. Phys. Oceanogr.* **33**, 2675-2688.
- Valle-Levinson, A., and K. M. M. Lwiza, 1995: The effects of channels and shoals on exchange between the Chesapeake Bay and the adjacent ocean. *J. Geophys. Res.*, **100**, 18551-18563.
- Whitney, M. M. and R. W. Garvine, 2005: Wind influence on a coastal buoyant outflow. *J. Geophys. Res.*, **110**, C03014, doi:10.1029/2003JC002261.

- Xu, Y., R. J. Chant, D. Gong, R. Castelao, S. Glenn, and O. Schofield, 2011: Seasonable variability of chlorophyll a in the Mid-Atlantic Bight. *Cont. Shelf Res.*, **31**, 1640-1650.
- Yankovsky, A. E. and D. C. Chapman, 1997: A simple theory for the fate of buoyant discharges. *J. Phys. Oceanogr.*, **27**, 1386-1401.
- Yankovsky, A. E. and R. W. Garvine, 1998: Subinertial dynamics on the inner New Jersey shelf during the upwelling season. *J. Phys. Oceanogr.*, **28**, 2444-2458.
- Yankovsky, A. E., B. M. Hickey, and A. K. Münchow, 2001: Impact of variable inflow on the dynamics of a coastal buoyant plume. *J. Geophys. Res.*, **106**, 19809-19824.
- Zhang, W. G., J. L. Wilkin, and R. J. Chant, 2009: Modeling the pathways and mean dynamics of river plume dispersal in the New York Bight. *J. Phys. Oceanogr.*, **39**, 1167-1183.